INVESTIGATING NEW GUAIAZULENES AND DIKETOPYRROLOPYRROLES FOR PHOTONIC APPLICATIONS

by

EBRAHIM H. GHAZVINI ZADEH

B.S. Lebanese University, 2007
M.S. American University of Beirut, 2009
M.S. University of Florida, 2012

A dissertation submitted in partial fulfillment of the requirements
for the degree of Doctor of Philosophy
in the Department of Chemistry
in the College of Sciences
at the University of Central Florida
Orlando, Florida

Spring Term
2015

Major Professor: Kevin D. Belfield

ABSTRACT

π-Conjugated systems have been the focus of study in recent years in order to understand their charge transport and optical properties for use in organic electronic devices, fluorescence bioimaging, sensors, and 3D optical data storage (ODS), among others. As a result, several molecular building blocks have been designed, allowing new frontiers to be realized. While various successful building blocks have been fine-tuned at both the electronic and molecular structure level to provide advanced photophysical and optoelectronic characteristics, the azulene framework has been underappreciated despite its unique electronic and optical properties. Among several attributes, azulenes are vibrant blue naturally occurring hydrocarbons that exhibit large dipolar character, coupled with stimuli-responsive behavior in acidic environments. Additionally, the non-toxic nature and the accompanying eco-friendly feature of some azulenes, namely guaiazulene, may set the stage to further explore a more "green" route towards photonic and conductive materials.

The first part of this dissertation focuses on exploiting guaiazulene as a natural building block for the synthesis of chromophores with varying stimuli-responsiveness. Results described in Chapter 1 show that extending the conjugation of guaiazulene through its seven-membered ring methyl group with aromatic substituents dramatically impacts the optical properties of the guaiazulenium carbocation. Study of these π–stabilized tropilium ions enabled establishing photophysical structure-property trends

for guaiazulene-terminated π-conjugated analogs under acidic conditions, including absorption, emission, quantum yield, and optical band gap patterns. These results were exploited in the design of a photosensitive polymeric system with potential application in the field of three dimensional (3D) optical data storage (ODS).

Chapter 2 describes the use of guaiazulene reactive sites (C-3 and C-4 methyl group) to generate a series of cyclopenta[*ef*]heptalenes that exhibit strong stimuli-responsive behavior. The approach presents a versatile route that allows for various substrates to be incorporated into the resulting cyclopenta[*ef*]heptalenes, especially after optimization that led to devising a one-pot reaction toward such tricyclic systems. Examining the UV-vis absorption profiles in neutral and acidic media showed that the extension of conjugation at C(4) of the cyclopenta[*ef*]heptalene skeleton results in longer absorption maxima and smaller optical energy gaps. Additionally, it was concluded that these systems act as sensitizers of a UV-activated (< 300 nm) photoacid generator (PAG), via intermolecular photoinduced electron transfer (PeT), upon which the PAG undergoes photodecomposition resulting in the generation of acid.

In a related study, the guaiazulene methyl group at C-4 was employed to study the linear and nonlinear optical properties of 4-styrylguaiazulenes, having the same π–donor with varying π-spacer. It was realized that the conjugation length correlates with the extent of bathochromic shift of the protonated species. On the other hand, a trend of

decreasing quantum yield was established for this set of 4-styrylguaiazulenes, which can be explained by the increasingly higher degree of flexibility.

The second part of this dissertation presents a comprehensive investigation of the linear photophysical, photochemical, and nonlinear optical properties of diketopyrrolopyrrole (DPP)-based derivatives, including two-photon absorption (2PA), femtosecond transient absorption, stimulated emission spectroscopy, and superfluorescence phenomena. The synthetic feasibility, ease of modification, outstanding robustness, and attractive spectroscopic properties of DPPs have motivated their study for fluorescence microscopy applications, concluding that the prepared DPP's are potentially suitable chromophores for high resolution stimulated emission depletion (STED) microscopy.

To my loving family and sincere friends.

ACKNOWLEDGMENTS

I would like to express my deepest gratitude to my advisor, Dr. Kevin D. Belfield, for his excellent guidance: he continually and persuasively conveyed a spirit of curiosity and adventure in research and scholarship.

My thanks go to the members of the research group for their professionalism and support. I would like to thank Dr. Adam W. Woodward and Dr. Simon Tang for their excellent collaboration, advice and commitment. Additionally, I would like to acknowledge Dr. Mykhailo Bondar for his guidance in the photophysical characterization of the compounds described in Chapter 3 and for his comments and explanation. I would also like to thank Dr. Taihong Liu for his constant support and assistance over my studies at the PhD program.

TABLE OF CONTENTS

LIST OF FIGURES

LIST OF TABLES

LIST OF SCHEMES

LIST OF ACRONYMS AND ABBREVIATIONS

^{13}C	Carbon 13 isotope
^{1}H	Hydrogen 1 isotope
2PA	Two-photon absorption
abs	Absorption
°C	Degrees centigrade
cal	Calculated
$CDCl_3$	Deuterated chloroform
cm^{-1}	Wavenumber
DCM	Dichloromethane
DMSO	Dimethylsulfoxide
em	Emission
ESA	Excited state absorption
exc	Excitation
fl	Fluorescence
fs	Femtosecond
GM	Goppert Mayer (10^{-50} cm^4 s $photon^{-1}$ $molecules^{-1}$)
Hz	Hertz
J	Coupling constant
kHz	Kilohertz

M	Molar
MeOH	Methanol
MHz	Megahertz
nm	Nanometer
NMR	Nuclear magnetic resonance
ns	Nanosecond
OD	Optical density
ODS	Optical data storage
PAG	Photoacid generator
pTHF	polytetrahydrofuran
S_0	Ground state, singlet
S_1	First excited state, singlet
THF	Tetrahydrofuran
TOL	Toluene
UV	Ultraviolet

CHAPTER 1: CHROMOPHORIC MATERIALS DERIVED FROM A NATURAL AZULENE: SYNTHESES, HALOCHROMISM AND ONE-PHOTON AND TWO-PHOTON MICROLITHOGRAPHY

1.1. Abstract

The commercial success of numerous pharmaceuticals relies on key intermediates that are isolated directly from natural sources.[1] This strategy has been employed extensively by the Pharma industry, which utilizes the preexisting bioactivity of natural products to enhance or add specificity to drugs and cosmetics through chemical modification. In fact, it is estimated that 40% of all medicines are natural extracts or semi-synthetic derivatives of naturally derived intermediates.[2] Similarly, the physical, electronic, and optical properties of some natural pigments could offer access to key building blocks for developing bio-derived chromophoric materials. Additionally, the non-toxic nature and the accompanying eco-friendly feature of natural dyes could set the stage for chemists to explore a more "green" route towards photonic and conductive material.[3,4] Among natural pigments, guaiazulene is considered a lead structure as it serves as a modular building block for the design and synthesis of functional materials with optical, conductive, and electron transfer properties. Toward that goal, this chapter details the syntheses of a series of 4-styrylguaiazulenes **3a-l** that are prepared by condensation of the C-4 methyl group of naturally-occurring guaiazulene **1** with various aromatic carboxaldehydes **2**. Treating these analogues **3a-l** with strong acids protonates

the electron-rich C-3 and reveals a reversible halochromic behavior where the optical energy gap responds predictably to electron-donor strength and degree of π-conjugation. Additionally, acid-doping is accompanied by efficient fluorescence switch-on, which allowed for the design of a new 3D fluorescence readout nonerasable (permanent or write-once read-many, WORM) system, which is comprised of a switch-on fluorescent guaiazulene-containing chromophore **3e** and commercially available iodonium photo-acid generator (PAG) in thin polymethyl methacrylate (PMMA) films.

1.2. The Enigmatic Azulenes

Figure 1. Common azulenes and some of their natural resources.[5]

Centuries ago, royal blue azulenes were extracted through distillations of various essential oils (Figure 1).[6] Though originally the color of these enigmatic oils was fallaciously attributed to contamination from the copper distillation apparatuses employed, the resulting azure-blue-colored oils were volatile, while no precipitate

(copper salts) was observed when washed with ether (Figure 2). The name "azulene" was coined in 1864 for this blue oil, however, it is now used to distinguish the parent compound and, hence, the class of derivatives thereof.[6] After the isolation of an azulene derivative in 1915, there had been several attempts to elucidate its structure, namely one that suggested a tricyclic system; however, hydrogenation indicated a bicyclic skeleton where the reduced products shared similarities with some sesquiterpenes. Finally, the isomerization of different azulenes to naphthalenes at high temperatures supported a 5,7-bicyclic structure, which was asserted by synthetically preparing azulene derivatives.[6] Since then, the striking blue-green color of azulenes has aroused scientific attention, initially for their physical properties but more recently for their novel electronic structures.[7] So what makes azulenes so colorful?

Figure 2. German Chamomile essential oil is known as a natural source for guaiazulene**.**

1.3. What Makes Azulenes Colored?

There are several factors that determine the "color" of matter; namely, colors are dictated by the absorption and the scattering properties of the materials. For a set of four polyenes: 1,3,5-hexatriene (colorless), retinal (yellow), β-carotene (orange), and astaxanthin (red), it is clear that the length of conjugation is an important structural feature that determines the richness of the color of each of these polyenes (Figure 3). This can be explained from simple molecular orbital considerations where the HOMO–LUMO gap is reliant on the length of conjugation, hence, as the HOMO-LUMO gap decreases, the wavelength of the absorbed color increases (bathochromic shift).[7]

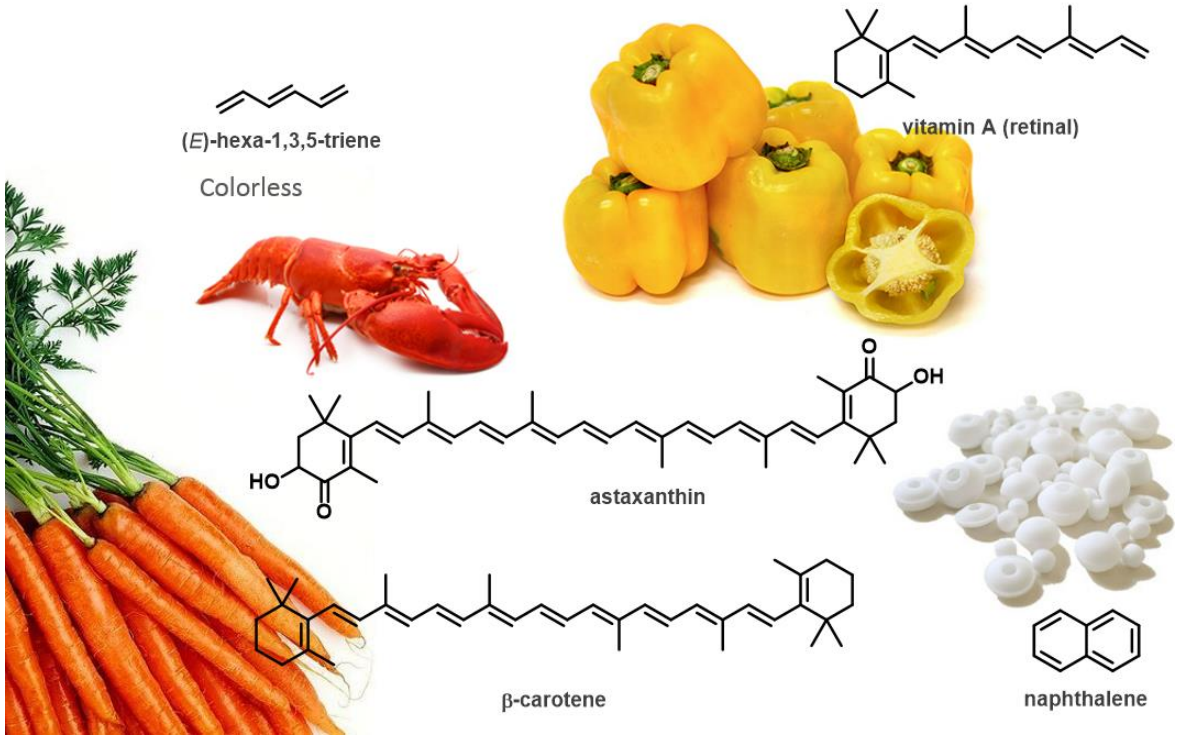

Figure 3. Richness of the color of various species as a direct result of increased conjugation of polyenes. Naphthalene, the constitutional isomer of azulene, is colorless.

The same explanation may not be extended when comparing azulene to its constitutional isomer, naphthalene. While both have the same number of conjugated π–bonds, naphthalene is colorless. The main perturbation that differentiates the two isomers lie in the non-alternate nature of azulene that inevitably accounts for its blue color. A non-alternate hydrocarbon exhibits a pattern with two adjacent unstarred carbons at the ring junction, whereas an alternant hydrocarbon has all alternating starred and unstarred carbons (Figure 4).

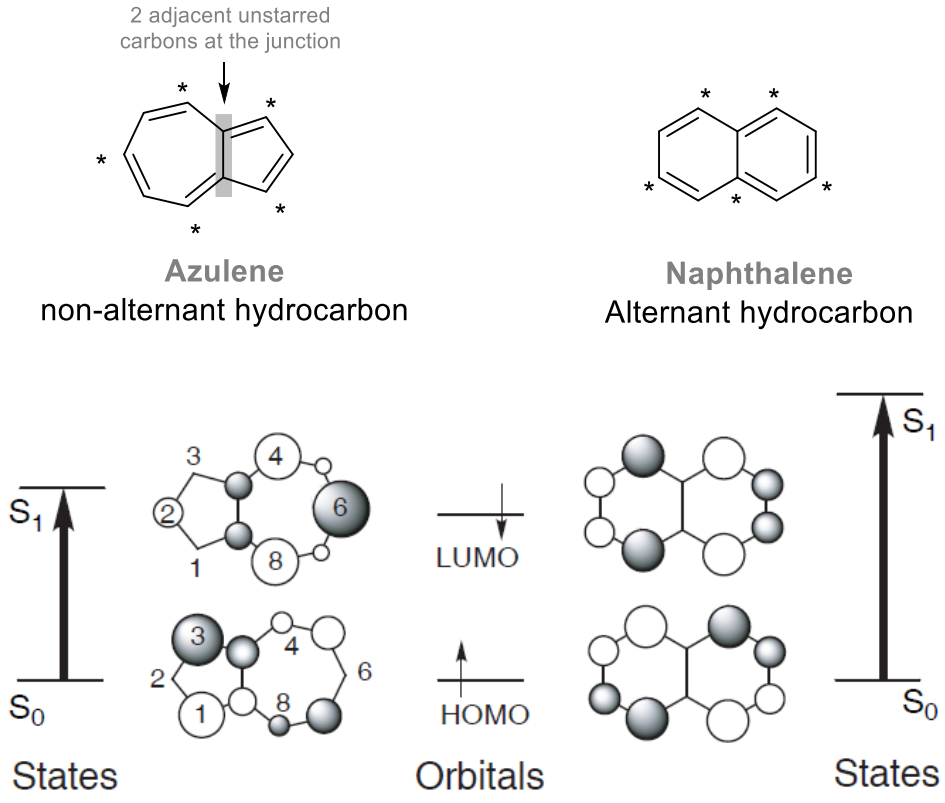

Figure 4. HOMO and LUMO of azulene and of naphthalene: the difference in relative sizes of coefficients of the atomic orbitals shows a large difference in distribution of electron density for the two molecules in their respective S_1 state.

The asymmetry in non-alternate hydrocarbons results in HOMO and LUMO orbitals occupying different areas of the molecule, resulting in a poor overlap between the two orbitals (Figure 4).[8] Thus, when considering frontier molecular orbitals (FMO) of azulene, each of the HOMO and LUMO contains one electron in the S_1 state.[7] As can be seen by the different locations of the nodal points in HOMO and LUMO, as well as the relative sizes of coefficients of the atomic orbitals, there is little overlap between these two electrons. This results in a slight repulsion between the two electrons occupying these two orbitals, and, hence, giving rise to a low transition energy to the S_1 state in the visible region (Figure 4).[7] Hence, the blue-green color of azulenes have a weak $S_0 \rightarrow S_1$ transition of the azulene at ~650 nm.[7]

On the other hand, naphthalene absorbs only in the UV region; this comes as a result of equal magnitude of the coefficients at different carbons for the HOMO and LUMO. In essence, the two electrons in these orbitals would occupy the same space, causing large electron–electron correlation energy, which raises the S_1 level of naphthalene. A similar situation exist in the case of LUMO+1 and HOMO of azulene, where the similar distribution of electron density in the two orbitals results in an increase in the energy of the S_2 state.[7] As a consequence of the higher S_2 state and the low lying S_1 state, azulene absorbs between 500 and 700 nm, resulting in an intense blue color.

The addition of an electron donating or withdrawing group at C-1 and/or C-3 leads to color change and a shift in the visible region band as depicted in Figure 5. By

considering the large electron coefficients at C-1 and C-3, it is possible to explain the effect that the nature of substituents has on the apparent color. For example, addition of two fluorine atoms at C-1 and C-3 has a destabilizing effect on HOMO and LUMO+1 while not disturbing the LUMO level (Figure 5). The corresponding higher S_0 energy level gives rise to a narrower gap and, hence, a bathochromic shift in the absorption spectrum (Figure 5).[7,8] On the contrary, the addition of electron withdrawing groups results in a more stable HOMO level, and hence a wider S_0-S_1 level (Figure 5).

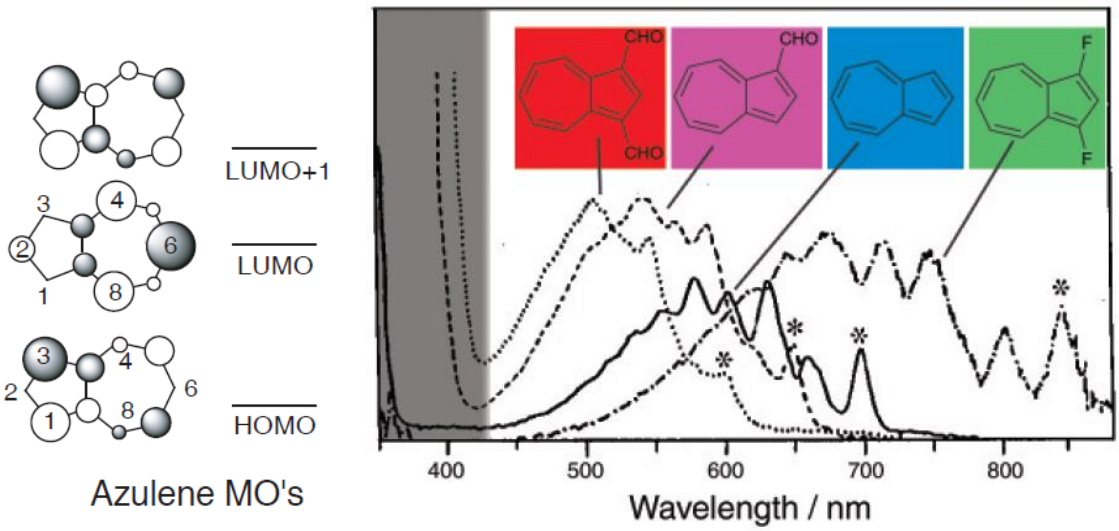

Figure 5. (Left) HOMO, LUMO and LUMO+1 of azulene.[7] (Right) Absorption profiles of 1,3-difluoroazulene (green), azulene (blue), azulene-1-carboxaldehyde (magenta), and azulene-1,3-dicarboxaldehyde (red). The S_0-S_2 transitions are shaded in grey while the transitions to the S_1 states lie between 500-800 nm.

The opposite can be observed for azulene absorption spectra when substituents occupy positions 2, 4 and/or 6. Electronically, the HOMO-LUMO energy gap becomes larger in the case of electron donating groups where the LUMO and LUMO+1 levels are raised in comparison to those of unsubstituted azulene (Figure 7). On the contrary, a red-

shift is notable for azulenes substituted at 4 or 6 position with an electron withdrawing group, characteristic of a narrower HOMO-LUMO energy gap (Figure 7). [9]

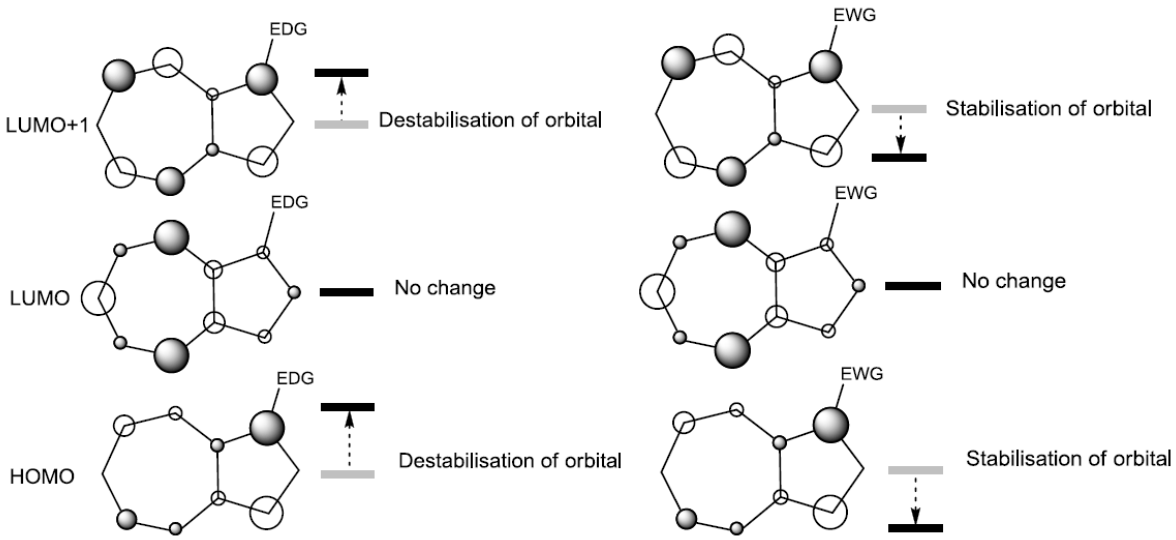

Figure 6. The effect of substituents at the C-1 on azulene FMO.[7]

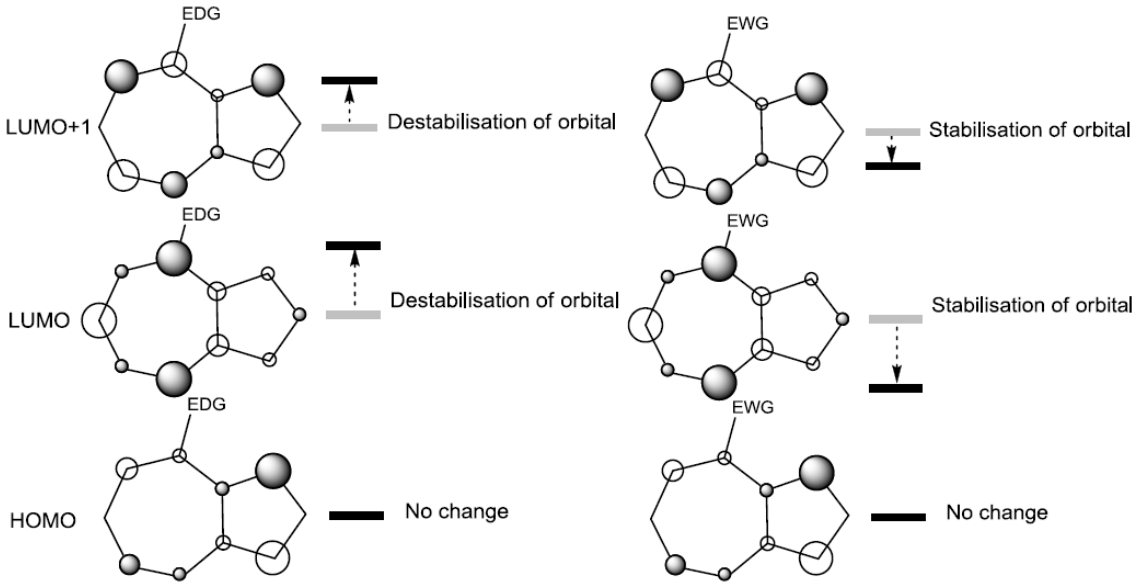

Figure 7. The effect of substituents at the C-4 on azulene FMO.[8]

1.4. Motives and Objectives

Azulenes structural and electronic features give access to various chemical modifications that enabled azulenes to be building blocks for the construction of conducting polymers,[18] as cathode modification layers in bulk-heterojunction solar cells,[19] and in electrochromic and nonlinear optical materials.[11] As a result of its high electron density at C-1/C-3, azulene can readily participate in electrophilic aromatic substitution. In fact, treatment of azulene with strong acids leads to protonation at C-1/C-3 and the formation of the resonance-stabilized 6-π-electron tropylium cation.[20] It was shown that extending the conjugation through the seven-membered ring of the parent azulene with aromatic substituents dramatically impacts the optical, electrochemical and electrochromic properties of azulenylium carbocation.[17-26]

We envisioned that using guaiazulene as a natural precursor, various stimuli-responsive chromophore can be synthesized, which would (a) help further understand the optical and electronic properties of azulenes derivatives, (b) establish photophysical structure-property trends for guaiazulene-terminated π-conjugated analogues under acidic conditions, including absorption, emission, quantum yield and optical band gap patterns, and (c) enable employing the synthesized chromophores in the design of eco-friendly photosensitive polymeric systems that can be derived from sustainable, naturally occurring sources with potential application in the field of 3D optical data storage (ODS).

1.5. Results and Discussion

1.5.1. Syntheses of 4-Styrylguaiazulenes 3a-l

4-Styrylguaiazulenes **3a-l** were prepared by condensation of the C-4 methyl group of guaiazulene and common aldehydes (Scheme 1). The reactivity of methyl group can be explained by hyperconjugation that is triggered by the electron-poor nature of the 7-membered ring.[27] While this reaction has been documented previously,[28] failure to reproduce the synthesis prompt us to investigate different reaction conditions (Table 1). The use of excess benzaldehyde **2a** (3 equiv.) in a solution of ^{t}BuOK and morpholine generates the corresponding 4-styrylguaiazulene **3a** (method *E*) in moderate yield. On the other hand, fewer side products and better yield were obtained when a solution of guaiazulene **1** in *t*-amyl alcohol was added dropwise to a hot solution of benzaldehyde **2a** (3 equiv.) and ^{t}BuOK in *t*-amyl alcohol (method *F*). It is noteworthy that in the case of low-melting aldehydes, careful addition of ^{t}BuOK to a melted guaiazulene/aldehyde mixture produces **3a** in better yields under neat conditions; however, employing these conditions requires the use of a large excess of **2** that serves to completely dissolve **1** (method *G*).

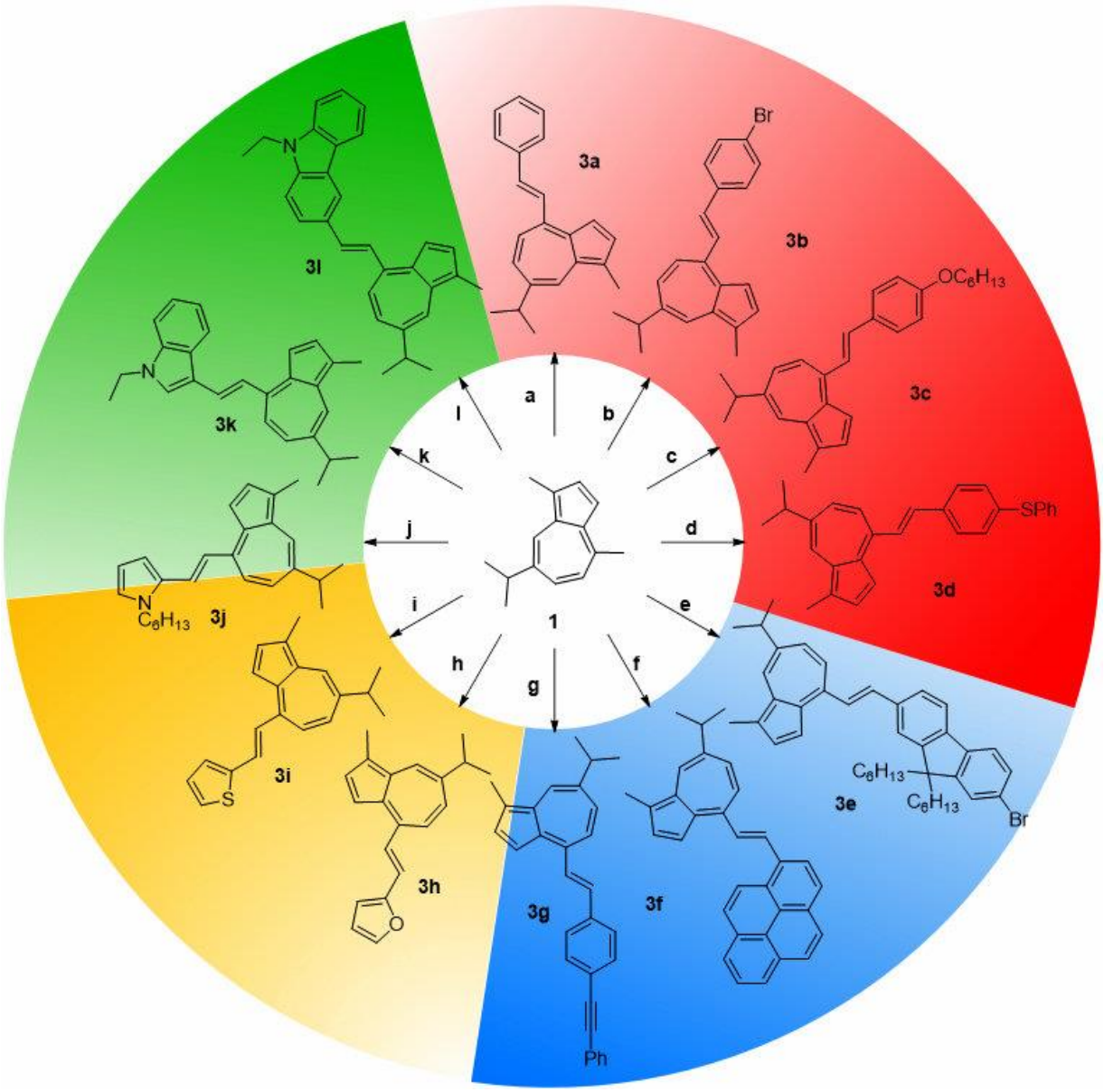

Scheme 1. Syntheses of 4-styrylguaiazulenes **3a-l**. Reagents and conditions: (a) benzaldehyde **2a**, method *F*, 54%; (b) 4-bromobenzaldehyde **2b**, method *G*, 48%; (c) 4-(hexyloxy)benzaldehyde **2c**, method *G*, 43%; (d) 4-(phenylthio)benzaldehyde **2d**, method *E*, 35%; (e) 7-bromo-9,9-dihexyl-9*H*-fluorene-2-carbaldehyde **2e**, method *F*, 34%; (f) pyrene-1-carbaldehyde **2f**, method *E*, 70%; (g) (*E*)-4-(4-bromostyryl)-7-isopropyl-1-methylazulene **3b**, $Pd(PPh_3)_2Cl_2$, CuI, K_2CO_3, THF, 32%; (h) furan-2-carbaldehyde **2g**, method *G*, 67%; (i) thiophene-2-carbaldehyde **2h**, method *G*, 66%; (j) 1-hexyl-1*H*-pyrrole-2-carbaldehyde **2i**, method *E*, 71%; (k) 1-ethyl-1*H*-indole-3-carbaldehyde **2j**, method *F*, 48%; (l) 9-ethyl-9*H*-carbazole-3-carbaldehyde **2k**, method *E*, 75%. Color represent the different series compared in this work: **3a-d**, **3e-g**, **3h-j**, and **3j-l**.

Table 1. Conditions for the formation of 3a.

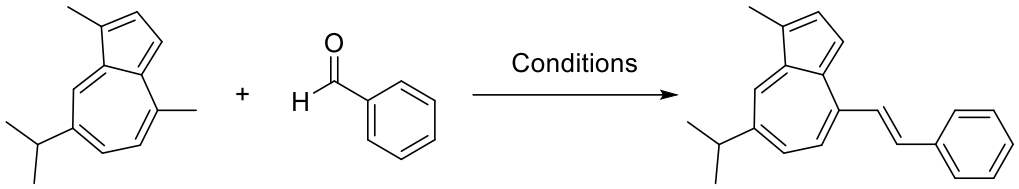

1 **2a** **3a**

Method	Equiv. of **2a**	Base (equiv.)	Solvent	Temp.	Yield (%)
A	3	K_2CO_3 (3)[c]	DMF	TBAB, 80 ˚C	0[a]
B	3	Cs_2CO_3 (3)	DMF	120 ˚C	Trace[a]
C	3	LDA	THF	0 ˚C	0[a]
D	3	^{t}BuOK (3)	THF	65 ˚C	29[b]
E	3	morpholine (1), ^{t}BuOK (3)	THF	65 ˚C	40[b]
F	3	^{t}BuOK (3)	^{t}AmOH	110 ˚C	54[b]
G	10	^{t}BuOK (3)	neat	100 ˚C	48[b]

[a] Product was not observed. [b] Isolated yields. [c] TBAB was added as transfer agent.

1.5.2. NMR Studies

NMR studies were carried out to determine the protonation site on 4-styrylguaiazulenes. In that regard, analyzing the ^{1}H NMR of **3i** and **3i**(H^+) shows that protonation takes place exclusively at C-3 as indicated by the singlet peak corresponding to C-1 Me- group and the presence of a broad peak that corresponds to the allylic protons at C-3 (Figure 8). Interestingly, all proton peaks corresponding to **3i**(H^+) are at higher

frequency than **3i**, thus indicating increased deshielding as a result of the resonance-stabilized tropylium cation.

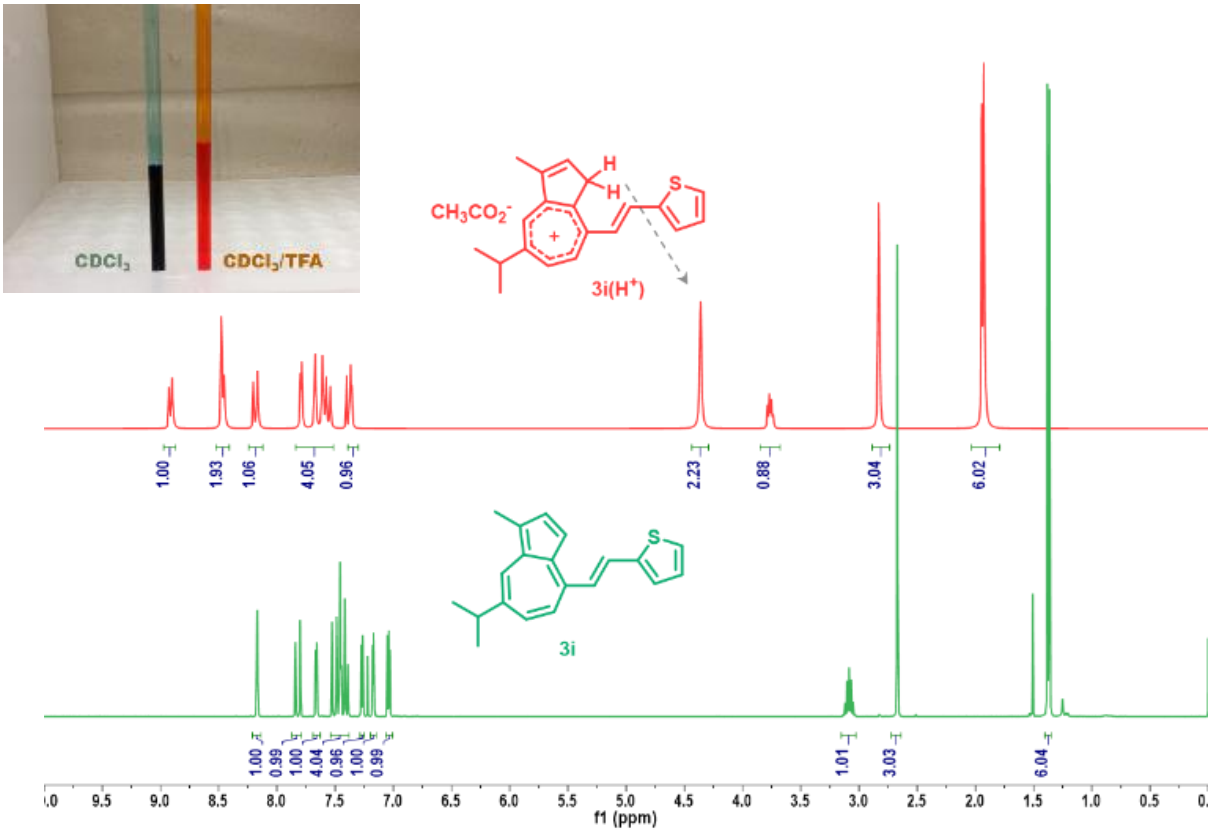

Figure 8. ^{1}H NMR spectra of **3i** in $CDCl_3$ and $CDCl_3$:TFA, inset showing the two solutions in NMR tubes in $CDCl_3$ and when treated with TFA.

1.5.3. UV-vis Absorption Study

Examination of the UV-vis spectra of **3a-l** in their neutral states (DCM) shows that all derivatives exhibit a broad profile with onsets of absorption ranging between 405 for **3a** and 472 nm for **3f** that corresponds to the S_0–S_2 transition (Table 2). In addition, all spectral profiles are distinguished by broad absorptions centered at ~ 650 nm that are correlated with the weak S_0–S_1 transition common in various azulene derivatives.

The effect of acid on the absorption of 4-styrylguaiazulenes **3a-l** was investigated employing either a solution of 10% TFA in DCM or photoexcitation of a solution of **3** and commercially available PAG, diphenyliodonium hexafluorophosphate (DPIHFP), in DCM. In all cases a bathochromic shift in the main absorption peak relative to the original π–π^* transitions reveals a dependence on the extent of conjugation of the guaiazulenium cation with the adjacent aromatic rings. For instance, guaiazulenium cations **3a-d**(H^+) (445, 450, 500, and 523 nm, respectively), the increasing absorption maxima can be correlated with an increased strength of the electron-donating group on the para position of the phenyl group, and hence a stronger donor (Figures 9-12).

Similarly, for guaiazulenium cation **3a**(H^+) baring a styryl group a sharp peak at λ_{max} = 445 nm is observed, while an increasingly dramatic impact on the absorption maxima is noted for guaiazulenium cations having *p*-(phenylethynyl)styryl **3g**(H^+) (λ_{max} = 490 nm), fluorenylvinyl **3e**(H^+) (λ_{max} = 529 nm), and pyrenylvinyl **3f**(H^+) (λ_{max} = 599 nm) moieties (Figures 13-15). Whereas a similar trend can be seen in the case of guaiazulenium cations conjugated to 5-membered ring heterocycles **3h-j**(H^+) (Figures 16-18), the absorption maxima of **3j-l**(H^+) are of comparable values (Figures 18-20). This suggests that the extent of conjugation of nitrogen-containing heterocyclic guaiazulenium cations has little impact on λ_{max}. Collectively, these observations indicate that narrowing of the optical band-gap upon treatment of **3** with strong acids can be systematically tuned by

the nature of the substituent conjugated to the seven-membered ring of guaiazulene (Table 2).

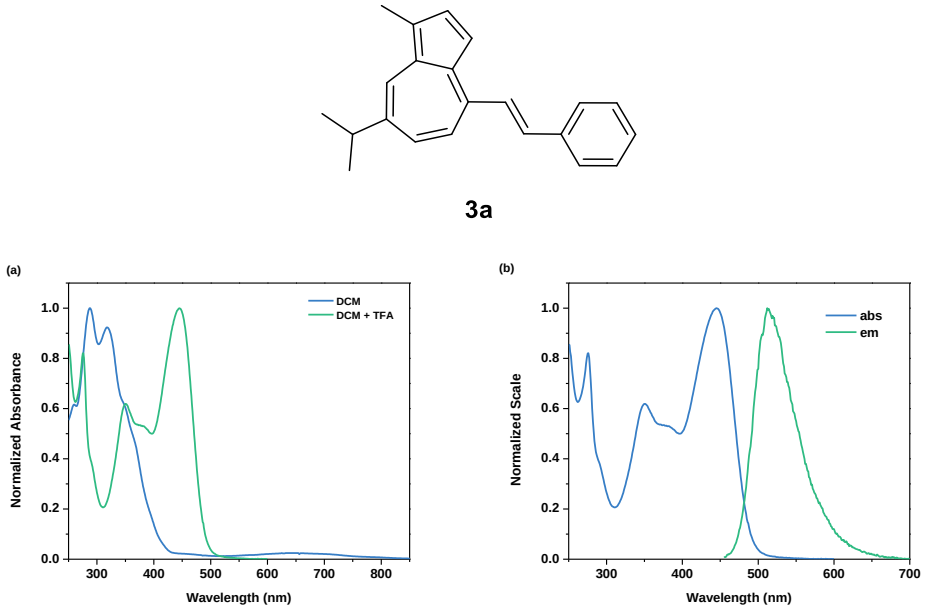

Figure 9. (a) Normalized absorbance spectra of **3a** in DCM, λ_{max} = 318 nm, and DCM:TFA (10%), λ_{max} = 445 nm. (b) Normalized abs and em spectra of **3a** in DCM:TFA (10%), λ_{ex} = 445 nm, λ_{max} = 512 nm, QY 0.03 (CV in MeOH).

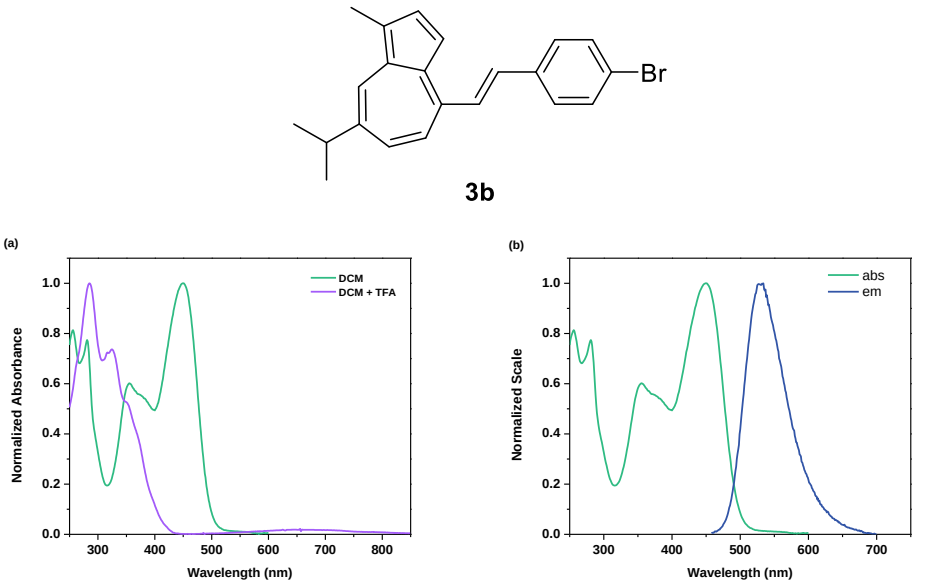

Figure 10. (a) Normalized absorbance spectra of **3b** in DCM, λ_{max} = 318 nm, and DCM:TFA (10%), λ_{max} = 450 nm. (b) Normalized abs and em spectra of **3b** in DCM:TFA (10%), λ_{ex} = 445 nm, λ_{max} = 534 nm, QY 0.05 (CV in MeOH).

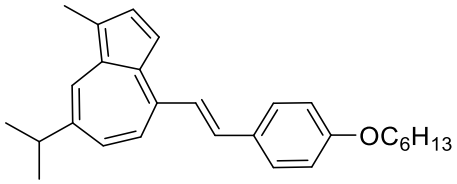

3c

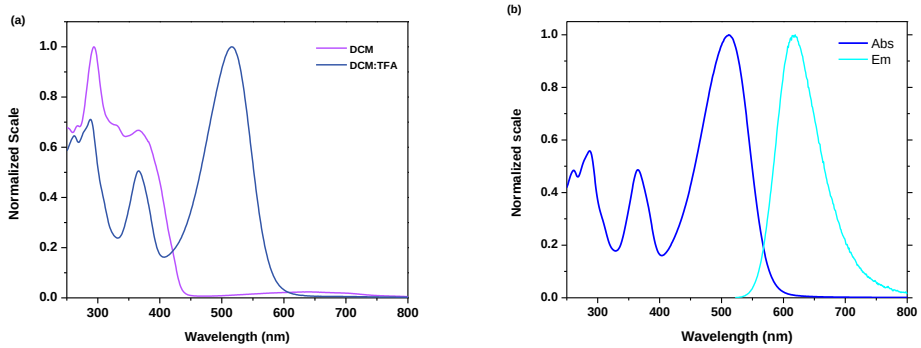

Figure 11. (a) Normalized absorbance spectra of **3c** in DCM, λ_{max} = 367 nm, and DCM:TFA (10%), λ_{max} = 516 nm. (b) Normalized abs and em spectra of **3c** in DCM:TFA (10%), λ_{ex} = 445 nm, λ_{max} = 534 nm, QY 0.12 (CV in MeOH).

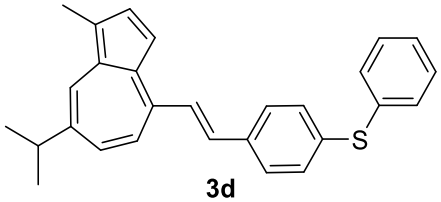

3d

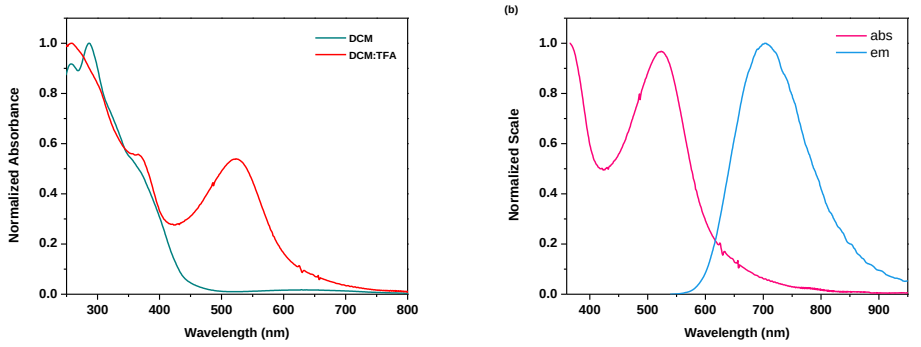

Figure 12. (a) Normalized absorbance spectra of **3d** in DCM, λ_{max} = 370 nm, and DCM:TFA (10%), λ_{max} = 523 nm. (b) Normalized abs and em spectra of **3d** in DCM:TFA (10%), λ_{ex} = 523 nm, λ_{max} = 705 nm, QY 0.11 (CV in MeOH).

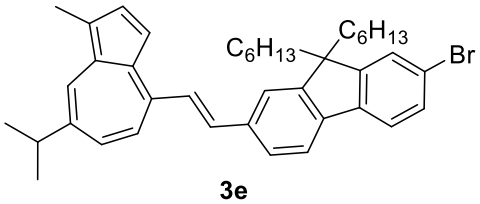

3e

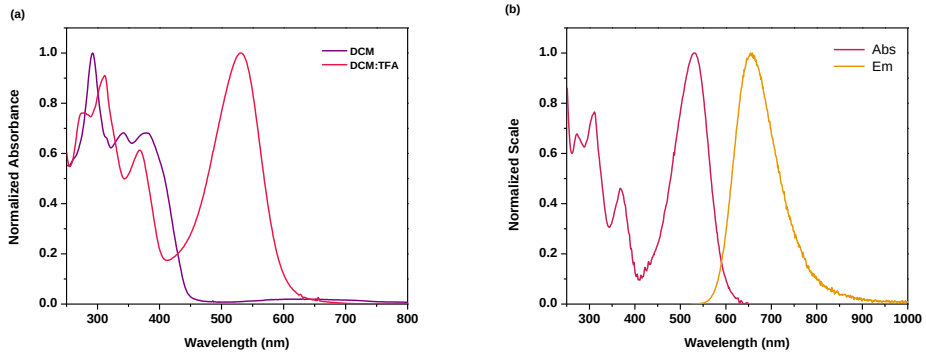

Figure 13. (a) Normalized absorbance spectra of **3e** in DCM, λ_{max} = 379 nm, and DCM:TFA (10%), λ_{max} = 530 nm. (b) Normalized abs and em spectra of **3e** in DCM:TFA (10%), λ_{ex} = 530 nm, λ_{max} = 656 nm, QY 0.70 (Rh6G in EtOH).

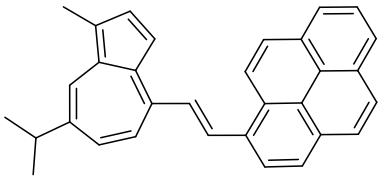

3f

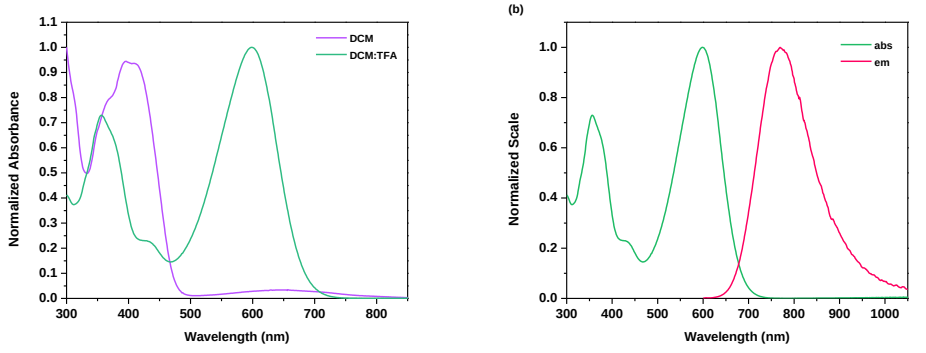

Figure 14. (a) Normalized absorbance spectra of **3f** in DCM, λ_{max} = 405 nm, and DCM:TFA (10%), λ_{max} = 599 nm. (b) Normalized abs and em spectra of **3f** in DCM:TFA (10%), λ_{ex} = 600 nm, λ_{max} = 768 nm, QY 0.05 (CV in MeOH).

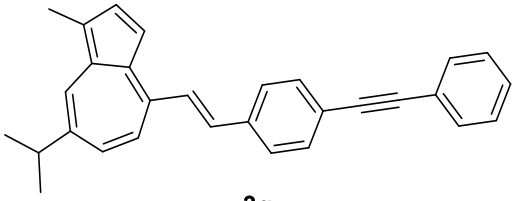

3g

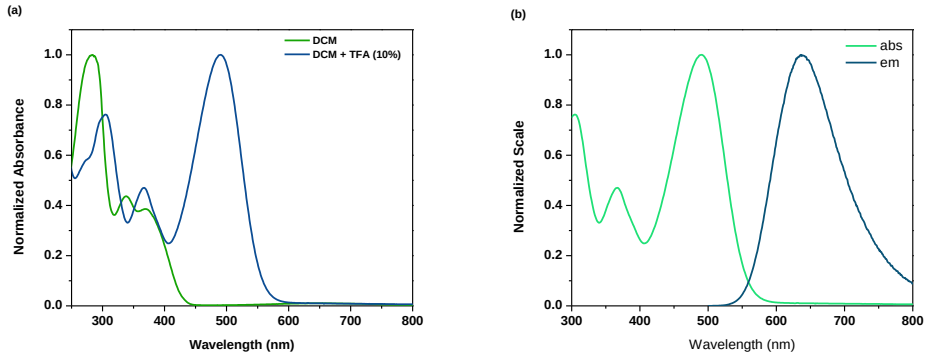

Figure 15. (a) Normalized absorbance spectra of **3g** in DCM, λ_{max} = 369 nm, and DCM:TFA (10%), λ_{max} = 490 nm. (b) Normalized abs and em spectra of **3g** in DCM:TFA (10%), λ_{ex} = 490 nm, λ_{max} = 636 nm, QY 0.55 (CV in MeOH).

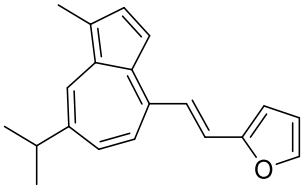

3h

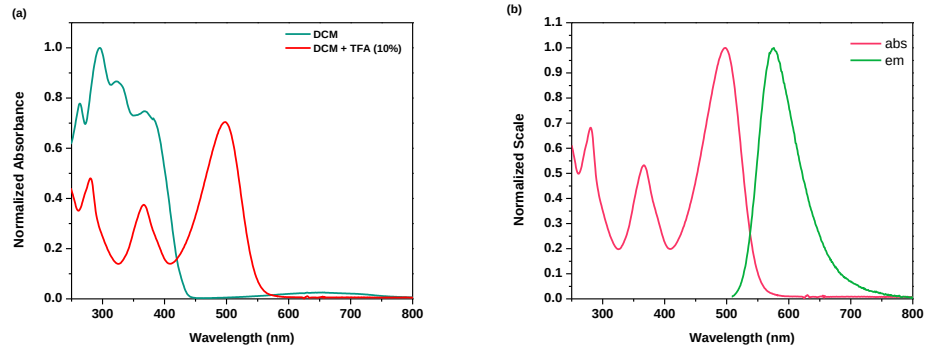

Figure 16. (a) Normalized absorbance spectra of **3h** in DCM, λ_{max} = 332 nm, and DCM:TFA (10%), λ_{max} = 498 nm. (b) Normalized abs and em spectra of **3h** in DCM:TFA (10%), λ_{ex} = 498 nm, λ_{max} = 576 nm, QY 0.19 (CV in MeOH).

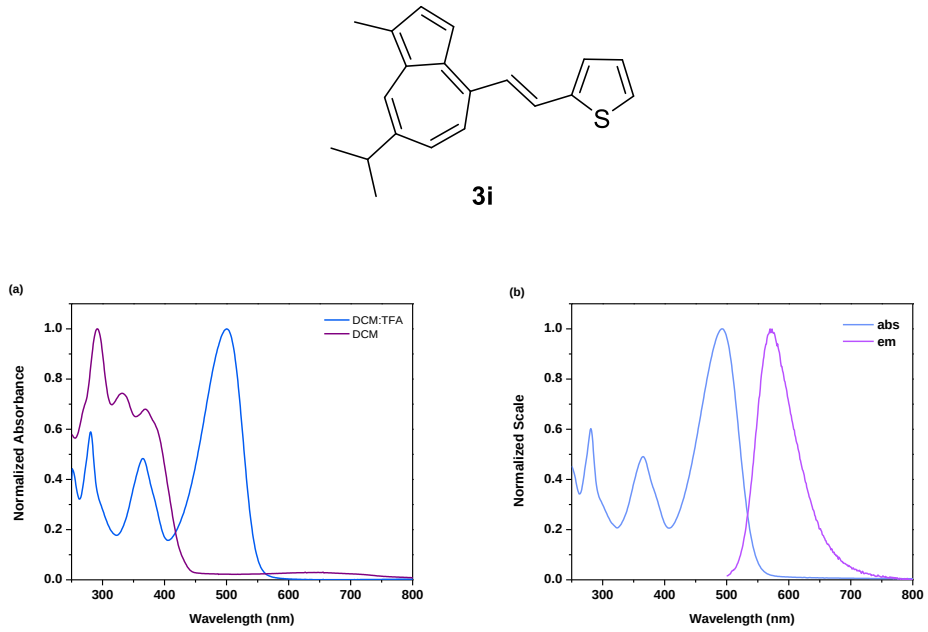

Figure 17. (a) Normalized absorbance spectra of **3i** in DCM, λ_{max} = 332 nm, and DCM:TFA (10%), λ_{max} = 493 nm. (b) Normalized abs and em spectra of **3i** in DCM:TFA (10%), λ_{ex} = 493 nm, λ_{max} = 570 nm, QY 0.02 (CV in MeOH).

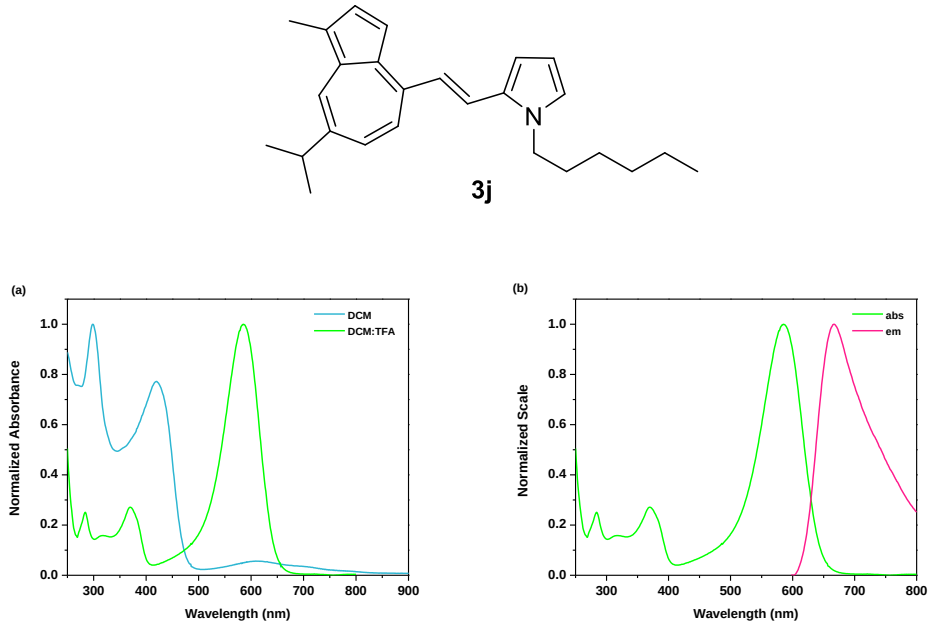

Figure 18. (a) Normalized absorbance spectra of **3j** in DCM, λ_{max} = 420 nm, and DCM:TFA (10%), λ_{max} = 587 nm. (b) Normalized abs and em spectra of **3j** in DCM:TFA (10%), λ_{ex} = 587 nm, λ_{max} = 663 nm, QY 0.01.

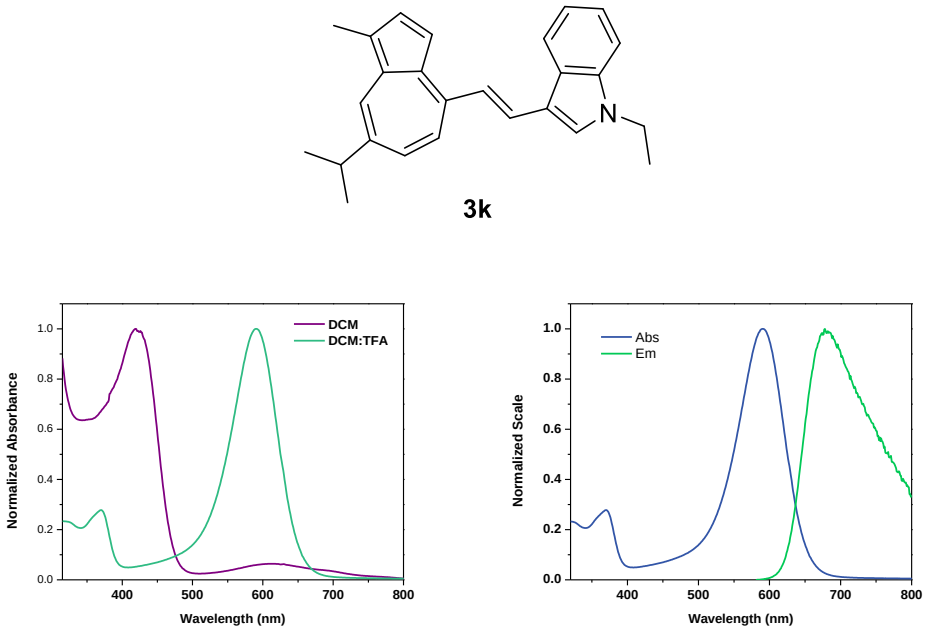

Figure 19. (a) Normalized absorbance spectra of **3k** in DCM, λ_{max} = 425 nm, and DCM:TFA (10%), λ_{max} = 590 nm. (b) Normalized abs and em spectra of **3k** in DCM:TFA (10%), λ_{ex} = 590 nm, λ_{max} = 678 nm.

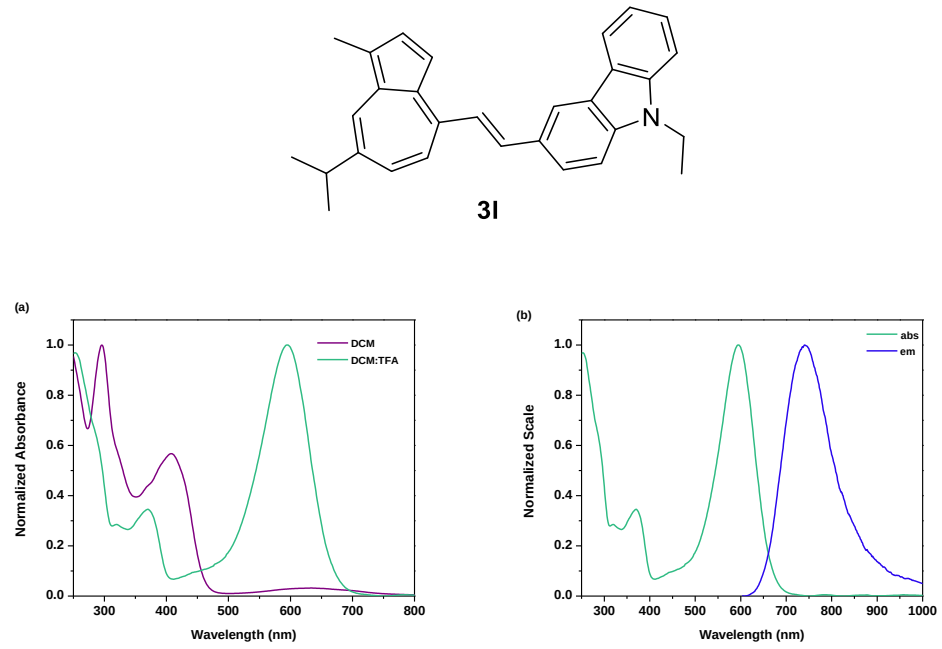

Figure 20. (a) Normalized absorbance spectra of 3l in DCM, λ_{max} = 407 nm, and DCM:TFA (10%), λ_{max} = 595 nm. (b) Normalized abs and em spectra of 3l in DCM:TFA (10%), λ_{ex} = 593 nm, λ_{max} = 744 nm.

Table 2. Linear optical properties of 3 in DCM:TFA.[a]

3	$\boldsymbol{\lambda_{max}^{abs}}$ (nm)[b]	$\boldsymbol{\lambda_{max}^{em}}$ (nm)[c]	Stokes shift (nm)	φ_F[d]	$\boldsymbol{E_g^o}$ (eV)
a	445	512	67	0.03	2.53
b	450	534	84	0.05	2.50
c	516	619	103	0.12	2.17
d	523	705	182	0.11	2.04
e	529	656	127	0.70	2.07
f	599	768	169	0.05	1.81
g	490	636	146	0.55	2.24
h	498	576	78	0.19	2.26
i	493	570	77	0.02	2.26
j	587	663	76	0.01	1.92
k	590	678	88	0.01	1.90
l	593	744	151	0.02	1.86

[a] All measurements performed at room temperature. [b] Absorption and emission maxima ±1 nm. [c] All experiments were performed using optical densities ≤ 0.1 at the excitation wavelength ($\lambda_{ex} = \lambda_{max}^{abs}$). [d] Fluorescence quantum yields are relative to the quantum yield of either DPA in cyclohexane, Rh6G in ethanol or CV in methanol.

1.5.4. Emission Properties of 4-Styrylguaiazulenes 3a-l

Similar to guaiazulene **1**, all synthesized 4-styrylguaiazulenes **3a-l** have an extremely weak S_1–S_0 emission in DCM. On the other hand, fluorescence is switched-on to varying extents upon dissolving **3a-l** in a solution of DCM:TFA (v:v, 9:1). The structureless emission spectra of **3a-l**(H^+) suggest that the long-wavelength emission may result from an internal charge transfer (ICT) state. Interestingly, emission maxima are also consistent with previous observations drawn from the absorption profiles, in that enhanced conjugation and increasing strength of electron-donor group of the aromatic

substituents result in longer S_1–S_0 emissions (Table 2). It is observed that all 4-styrylguaiazulenes have considerably large Stokes shift, however, the calculated Stokes shift for **3d**(H^+) (181 nm) is surprisingly larger than those determined of the same series (**3a-c**(H^+)). It is noteworthy that derivatives baring aromatic substituents of expanded conjugation **3e-g**(H^+) similarly show large Stokes shifts, reflecting more structural reorganization of **3d-g**(H^+) upon photoexcitation.

The fluorescence quantum yields (Φ_F) measured for **3a-d**(H^+) show a steady increase in the radiative decay upon photoexcitation with increasing donor strength (Table 2). On the other hand, guaiazulenium **3e**(H^+) and **3g**(H^+) have exceptionally high fluorescence quantum efficiencies as result of increased conjugation and rigidity. Fluorescence switching-on is also observed in the case of **3h**(H^+) with a Φ_F of 0.19, but becomes negligible for **3i**(H^+) as a direct consequence of significant spin-orbit coupling induced by the thienyl **s**ulfur.

1.5.5. Acid Titrations on 4-Styrylguaiazulenes

The study of UV-vis spectral changes as a function of TFA concentration was made using two closely related 4-styrylguaiazulenes **3b,c**. In both cases, the addition of TFA results in a gradual increase in intensities of new peaks corresponding to the protonated species along with bleaching of the π–π^* transition peaks in the UV-region (Figure 21). In addition, both 4-styrylguaiazulene analogs **3b,c** display an isosbestic point at 380 and 425 nm, respectively, as a result of two interconverting optically different species.

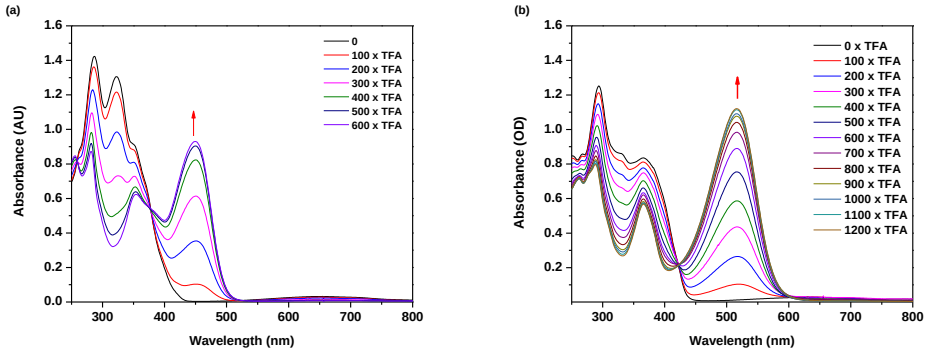

Figure 21. Absorption spectra of (a) **3b** (8.0×10^{-5} M) and (b) **3c** (8.0×10^{-5} M) upon titration with a solution of TFA and DCM.

It is notable that the equivalence of TFA necessary to induce complete acid saturation varies between the two derivatives, however, a trend related to the different electron donor strength could not be established as seen in the case of titration of **3l** (Figure 22).

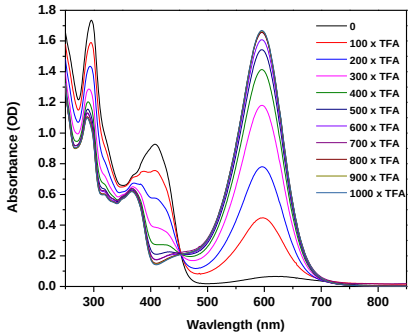

Figure 22. Absorption spectra of **3l** (8.0×10^{-5} M) upon titration with a solution of TFA and DCM.

In a similar fashion, fluorescence spectral changes as result of incremental TFA concentration were studied by employing **3e** that exhibits significant switch-on fluorescence (Figure 23). As predicted, the intensity of the emission band at 656 nm

responds proportionally to TFA titrations, where 1500 molar equivalences of TFA are deemed necessary to achieve a 6-fold increase in the emission band at 8.0×10^{-6} M of **3e**.

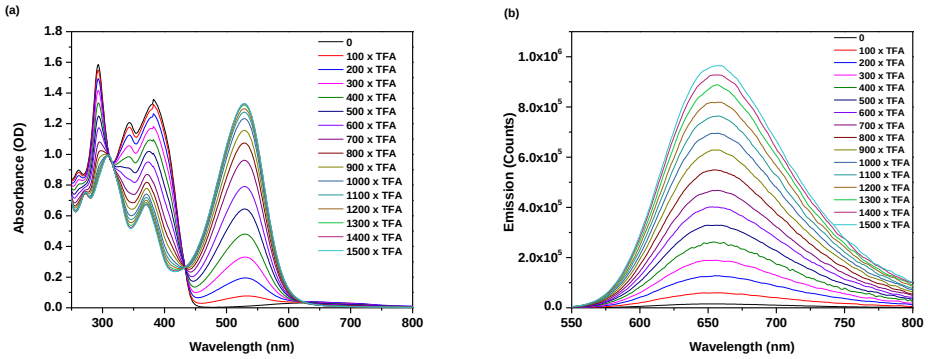

Figure 23. (a) Absorption spectra of **3e** (8.0×10^{-5} M) (b) and emission spectra of **3e** (8.0×10^{-6} M) upon titration with a solution of TFA in DCM.

1.5.6. Phototitration using Photoacid Generator

A similar halochromic behavior was observed when an equimolar solution of **3e** and a commercially available onium PAG, DPIHFP, is irradiated at 405 nm where absorption spectra were recorded at 1 minute intervals (Figure 24a). While DPIHFP is activated at wavelengths below 300 nm, photoexcitation is also achieved at 405 nm through an intermolecular photoinduced electron transfer (PeT) phenomenon, which is reported to occur from the S_2 state of guaiazulene to the excited state of various electron acceptors.[29,30] Sensitization of UV-activated DPIHFP with **3e** was evident as the band at λ_{max} = 532-537 nm, associated with **3e**(H+) UV-vis profile, gradually emerges with a concomitant decrease in intensity of 365 nm peak. In a solution of 2:1 DPIHFP/**3e** (Figure 24b), complete conversion to the protonated species **3e**(H+) was achieved in a shorter

time period, while a further increase in the concentration of DPIHFP had little effect on peak intensities and irradiation time that is necessary for complete protonation.

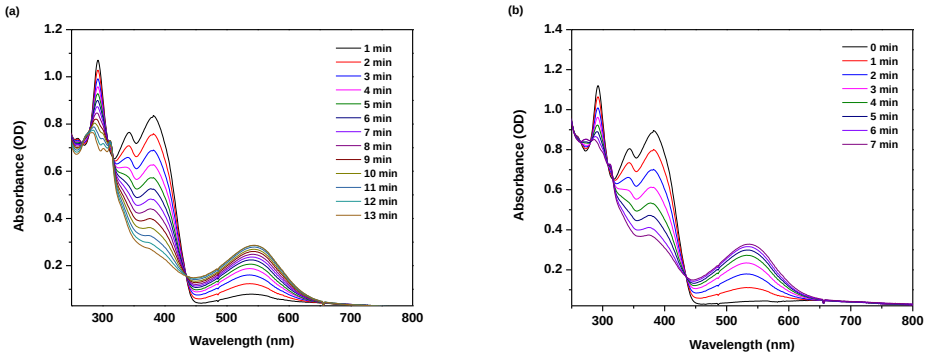

Figure 24. Absorption spectra of **3e** (8.0×10^{-5} M) in the presence of (a) 1 equiv. and (b) 2 equiv. of DPIHFP in DCM (1 min interval, average irradiance = 24.3 mW cm^{-2} at 405 nm).

1.5.7. Thin-film One-Photon and Two-Photon Microlithography

The results described previously encouraged us to design a photosensitive polymeric system with potential application in the field of 3D optical data storage. These films are prepared by spin-coating a DCM solution of **3e** as an acid-sensitive fluorescence switch-on dye/PAG sensitizer, DPIHFP as the photoacid generator, and PMMA as the matrix. The thin film samples are then irradiated using custom printed transparency masks as well as a copper TEM grid. A 405 nm-laser is briefly used to excite the film samples placed under the appropriate masks. Brightfield images are then collected after the removal of the masks by using an Olympus IX-81 microscope with a TRITC filter cube to capture the fluorescence emitted by **3e**(H+). Control images, taken for sections of the film that saw no 405 nm excitation, showed only autofluorescence or negligible signal. One the other hand, fluorescence images of one-photon irradiated masked samples were

taken under 100× magnifications showing grid sizes of approximately 100 μm from one corner of a square grid to the other (Figure 25a). Unfortunately for the mask used in Figure 25b (a compilation of four images), capture of a detailed smaller image was limited by the quality of the mask made. The excellent contrast seen from these images from such short exposure times prompted the attempt to probe the quality of 2PE lithography with these films. The corresponding samples were examined under a Leica SP5 confocal microscope with a 63× 1.20 numerical aperture water immersion objective coupled to a 2PE system with 800 nm wavelength emission. Point excitation of the film was performed by setting the microscope at the maximum optical zoom allowed and irradiating for a period of five seconds followed by moving in the Z direction to another area below the first plane and exciting for the same time interval. The image was then retaken using 1× zoom at 561 nm and collected from 570 – 650 nm and scanned using 0.15 μm steps. Collected images as a result of 2PE can be seen in Figure 26. Scanned voxels show an average size of ~5 × 6 nm in the xy-plane with an example shown in Figure 26a. Figure 26b shows a 3D rendering of a single voxel where the height along the z-direction could be measured as being approximately 16 μm. Figure 26c shows a 3D image corresponding to Figure 26a with a side view along the z-axis clearly showing the distinct region of no fluorescence that lies in between the two voxels.

We then studied the effect of radiation power and interval, in which two different irradiation powers (1.6 mW and 0.7 mW) and (5.0 s and 0.5 s) times were used to create

the voxels. Figure 27a-d depicts the sectional view of the captured images. As expected, higher power and longer exposure time lead to greater depth of the voxel along the z-axis (18-20 μm).[31] On the other hand, a low power radiation with a short exposure time result in a depth of ~9 μm. The rectangular to cuboidal shape of the voxels can be attributed to the faster scanning mode of the microscope, which translates to the voxels being created with a false point scanning method despite applying maximum optical zoom.[32] This mainly affected the y-axis of the voxel with an average length of ~5 μm to ~2 μm. The results, however, show that if a true point scan was applied, the spatial resolution could be greatly enhanced by controlling the power and speed of irradiation.

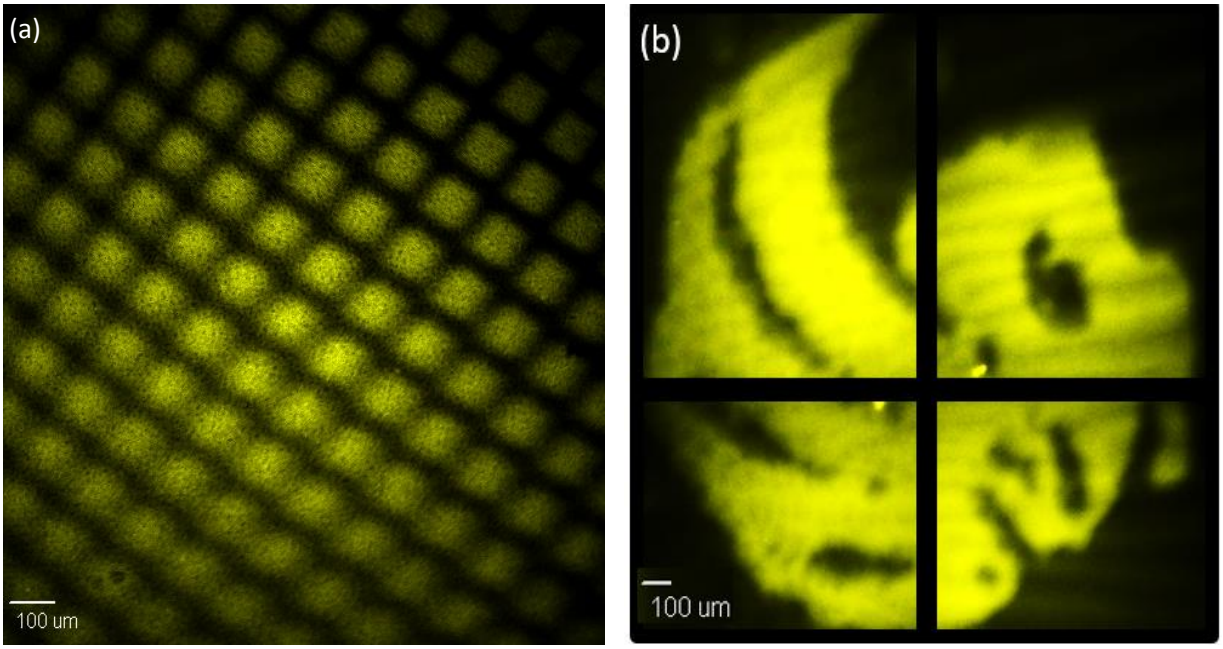

Figure 25. Thin film fluorescence image using (a) 200 mesh TEM grid mask and (b) custom transparent mask. (Images taken with a custom TRITC filter cube (Ex:525/40; DM:555; Em:624/40 – Scale bar 100 μm). Spin-coated films are prepared from a solution of **3e**, 2% (w/w); DPIHFP, 6%; PMMA, 92% in DCM (5 mL).

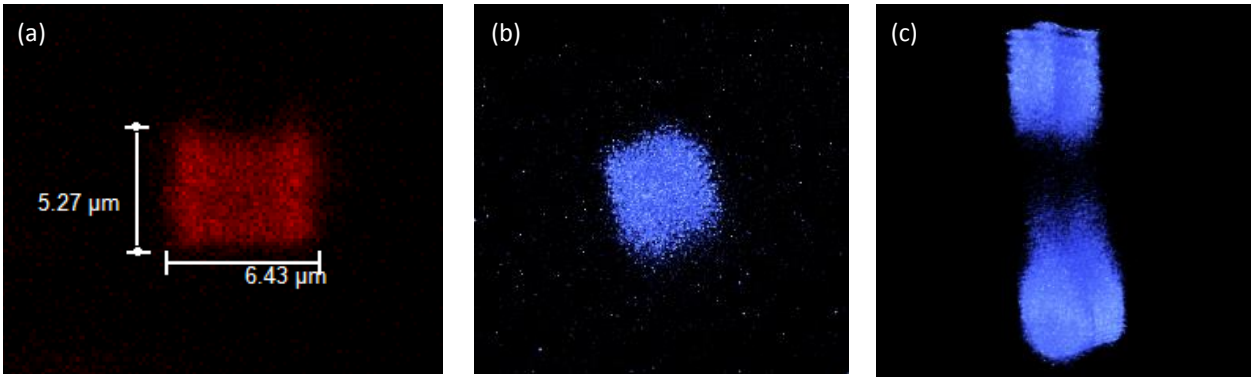

Figure 26. 2PE images of thin film samples: (a) Top down view of voxel showing average size of ~ 5 × 6 µm, (b) 3D reconstructed image of single voxel, (c) 3D reconstructed image of two voxels separated along the z-axis.

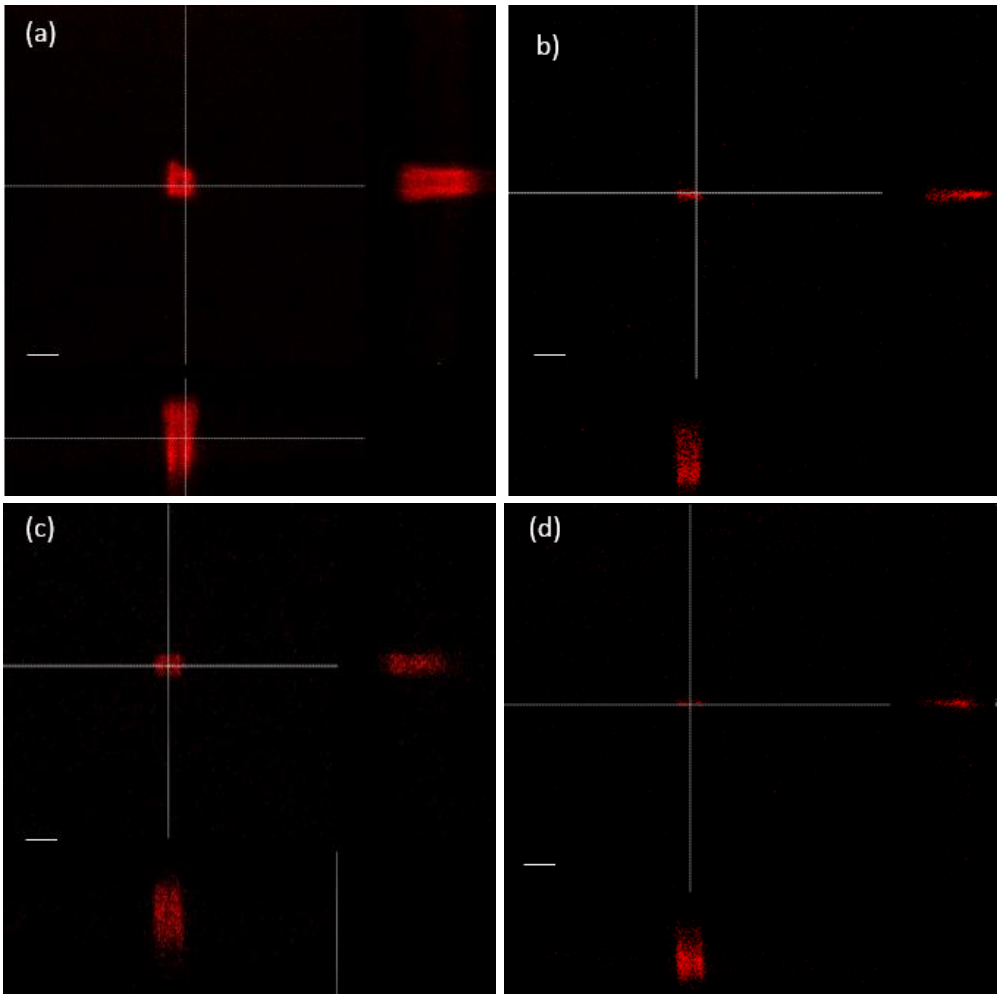

Figure 27. Sectional view of irradiation power and time experiments. Irradiation powers of 1.6 mW for (a) and (b) and 0.7 mW for (c) and (d). Irradiation times of 5.0 s for (a) and c and 0.5 s for (b) and (d). (Scale bar 5 µm).

1.6. Conclusion and Future work

In conclusion, naturally-occurring guaiazulene has been used as a building block to prepare an introductory set (**3a-l**) of 12 guaiazulene-terminated π-conjugated analogs for which photophysical structure-property trends under acidic conditions are established. Experiments indicates a linear dependence of photophysical behavior on the nature of the donor moiety, and shows how the extent of π-conjugation can result in tunable optical energy gaps for the described guaiazulenium derivatives. In addition, the fluorescence switching-on of these analogues in response to protonation via a commercial PAG was considered for the design of photosensitive polymeric system with potential application in the field of 3D optical data storage. The corresponding images clearly demonstrate the ability for **3** to be applied in the use of 2PE fluorescence lithography with its high fluorescence signal after very short irradiation times. Efforts to further explore the use of guaiazulene as an eco-friendly, non-toxic starting material for deriving chromophores for bio-imaging applications are on-going in our research group.

1.7. Experimental Section

1.7.1. General Information

Reagents and solvents were purchased from commercial sources and used without further purification unless otherwise specified. THF was degassed in 4 L drum and passed through two sequential purification columns (activated alumina) under a positive nitrogen atmosphere. Thin layer chromatography (TLC) was performed on SiO_2-60 F254

aluminum plates with visualization by UV light or TFA staining. Flash column chromatography was performed using CombiFlash Rf 200. Melting points (mp.) were determined on a Fisher Scientific melting point apparatus. 400(100) MHz $^{1}H(^{13}C)$ NMR spectra were recorded on Bruker AvanceIII 400 spectrometer. 500(125) MHz $^{1}H(^{13}C)$ NMR were recorded on Varian VNMRS 500 spectrometer. Chemical shifts (δ) are given in parts per million (ppm) relative to TMS and referenced to residual protonated solvent ($CDCl_3$: δH 7.26 ppm, δC 77.23 ppm; DMSO-d_6: δH 2.50 ppm, δC 39.50 ppm). Abbreviations used are s (singlet), d (doublet), t (triplet), q (quartet), quin (quintet), hp (heptet), b (broad), and m (multiplet). ESI-TOF-MS spectra were recorded on Agilent 6210 TOF spectrometer, respectively. Linear photophysical parameters were determined at room temperature in spectroscopic grade DCM. The steady-state one-photon absorption spectra were obtained with UV-Vis spectrophotometer Agilent 8453, using regular quartz cells with 1 cm path length and molecular concentrations as reported. The steady-state fluorescence was measured with FLS980 spectrofluorimeter (Edinburg Instruments Ltd.), using spectrofluorimetric quartz cells with 1 cm path length and low concentrated solutions (C $\approx 8 \times 10^{-6}$ M). Fluorescence quantum yields (Φ_F) were determined by standard method relative to DPA in cyclohexane, Rh6G in ethanol or CV in methanol.

1.7.2. One and two-photon microscopy of film samples

Film samples were initially irradiated with a 405 nm laser through a custom mask printed on a clear transparency or a 200 mesh copper TEM grid. Brightfield one-photon

images were then taken using an Olympus IX-81 microscope equipped with a Hamamatsu EM-CCD C9100 digital camera using a TRITC filter cube (Ex:525/40; DM:555; Em:624/40) and a 10x (Olympus UplanFLN 10x, N.A.=0.30) objective. One and two-photon microscopy images were all recorded with a Leica TCS SP5 II laser-scanning confocal microscope system with a 63× objective (HCX Pl APO CS 63.0 × 1.20 WATER UV) coupled to a tunable Coherent Chameleon Vision S (80 MHz, mode-locked, 75 fs pulse width, tuned to 900 nm) laser. Irradiation times of up to ten seconds were used for the excitation of dye film samples followed by confocal one-photon images taken by exciting the film sample at 561 nm and collecting between 570-620 nm. Captured images were then 3D rendered by using Olympus Slidebook V5.0. Laser power was measured from the output of the beam from the objective.

1.7.3. Syntheses of 4-tyrylguaiazulenes 3a-l.

Method *E*: A solution of guaiazulene 1 (1.0 mmol) in anhyd. THF (5 mL) was added dropwise to a hot solution of **2** (3.0 mmol), morpholine (1.0 mmol), and ^{t}BuOK (3.0 mmol) in anhyd. THF (5 mL). The mixture was heated until most of the starting material was consumed (0.2 – 1.0 h). The mixture was cooled to room temperature and poured in dilute HCl (1 N), then extracted with EtOAc (2 × 25 mL). The fractions were dried over Na_2SO_4 and evaporated under reduced pressure. Flash column chromatography using hexanes and EtOAc (0 → 5%) afforded the desired product as green solid. For Method *F*, a hot solution of ^{t}BuOK (3.0 mmol) in *t*-amyl alchol (10 mL) was heated at 105 °C for 30

min. To this solution was added **2** (3.0 mmol) followed by the dropwise addition of a solution of guaiazulene 1 (1.0 mmol) in *t*-amyl alchol (5 mL). The solution was heated for 3 h at 105 °C, then cooled to room temperature and poured in dilute HCl (1 N). The mixture was extracted with DCM (2 × 25 mL) and worked up as above. As for method *G*, 10.0 mmol of aldehydes **2a-c**, **2g** or **2h** and guaiazulene **1** (1.0 mmol) were heated to 80 C in a sand bath followed by the addition of ^{t}BuOK (3.0 mmol) in small portions. The slurry was heated for 10 min and the cooled to room temperature. The greenish solid was dissolved with hexanes (30 mL) and filtered through a short silica pad. The solvent was condensed and the resulting crude mixture was purified using Flash column chromatography using hexanes and EtOAc (0 → 3%).

(*E*)-7-Isopropyl-1-methyl-4-styrylazulene (3a). Green oil (54%). ^{1}H NMR (NMR ($CDCl_3$, 400 MHz) δ 8.25 (dd, J = 1.7, 0.8 Hz, 1H), 8.06 (d, J = 16.1 Hz, 1H), 7.77 – 7.70 (m, 1H), 7.68 (ddt, J = 7.7, 1.3, 0.6 Hz, 2H), 7.60 – 7.35 (m, 7H), 3.15 (p, J = 6.9 Hz, 1H), 2.74 (s, 3H), 1.44 (d, J = 7.0 Hz, 4H). ^{13}C NMR ($CDCl_3$, 100 MHz) δ 142.2, 140.5, 137.2, 135.3, 134.3, 133.5, 130.0, 129.2, 128.7, 127.4, 126.3, 120.7, 112.3, 38.7, 25.1, 13.4. HRMS (ESI) (*m*/*z*): $[M + H]^+$ calcd for $C_{22}H_{23}$ 287.1794; found, 287.1790.

(*E*)-4-(4-Bromostyryl)-7-isopropyl-1-methylazulene (3b). Green needles (mp. 100.0 – 102.0 °C, 46%). ^{1}H NMR (NMR ($CDCl_3$, 400 MHz) δ 8.18 (s, 1H), 7.97 (d, J = 16.1 Hz, 1H), 7.67 (d, J = 3.9 Hz, 1H), 7.59 – 7.36 (m, 7H), 7.28 (d, J = 16.2 Hz, 1H), 3.09 (sept, J = 6.9 Hz, 1H), 2.67 (s, 3H), 1.37 (d, J = 6.9 Hz, 6H). ^{13}C NMR ($CDCl_3$, 100 MHz) δ 141.5, 140.5, 137.1,

136.9, 136.7, 136.4, 135.0, 133.4, 132.7, 132.1, 130.5, 128.6, 126.1, 122.3, 120.3, 112.0, 100.1, 38.5, 29.9, 24.9, 13.2. HRMS (ESI) (*m*/*z*): $[M + H]^+$ calcd for $C_{22}H_{22}Br$ 365.0899; found, 365.0895.

(*E*)-4-(4-(Hexyloxy)styryl)-7-isopropyl-1-methylazulene (3c). Green needles (mp. 55.0 – 58.0 °C, 43%). ^1H NMR ($CDCl_3$, 400 MHz) δ 8.21 (s, 1H), 7.92 (d, J = 16.1 Hz, 1H), 7.69 (d, J = 3.9 Hz, 1H), 7.60 (d, J = 8.6 Hz, 2H), 7.57 – 7.49 (m, 3H), 7.38 (d, J = 16.1 Hz, 1H), 6.97 (d, J = 8.6 Hz, 2H), 4.04 (t, J = 6.6 Hz, 2H), 3.14 (sept, J = 6.9 Hz, 1H), 2.72 (s, 3H), 1.84 (dd, J = 8.5, 6.4 Hz, 2H), 1.56 – 1.33 (m, 13H), 1.00 – 0.93 (m, 2H). ^{13}C NMR ($CDCl_3$, 100 MHz) δ 159.7, 142.4, 139.9, 136.8, 136.6, 136.3, 135.0, 133.7, 133.1, 130.0, 128.5, 127.3, 125.9, 120.3, 115.0, 112.0, 68.3, 38.4, 31.7, 29.9, 29.4, 25.9, 24.9, 22.8, 14.2, 13.2. HRMS (ESI) (*m*/*z*): $[M + H]^+$ calcd for $C_{28}H_{35}O$ 387.2682; found, 387.2688.

(*E*)-(4-(2-(7-Isopropyl-1-methylazulen-4-yl)vinyl)phenyl)(phenyl)sulfane (3d). Green powder (mp. 120.0 – 122.0 °C, 35%) ^1H NMR ($CDCl_3$, 500 MHz) δ 8.21 (d, J = 1.8 Hz, 1H), 8.00 (d, J = 16.2 Hz, 1H), 7.72 – 7.66 (m, 1H), 7.60 – 7.55 (m, 2H), 7.51 (d, J = 1.9 Hz, 1H), 7.46 (dd, J = 7.5, 3.6 Hz, 2H), 7.44 – 7.41 (m, 2H), 7.38 – 7.33 (m, 5H), 7.32 – 7.28 (m, 1H), 3.12 (sept, J = 6.9 Hz, 1H), 2.70 (s, 3H), 1.40 (d, J = 6.9 Hz, 6H). ^{13}C NMR ($CDCl_3$, 125 MHz) δ 141.6, 136.8, 136.7, 136.5, 136.4, 136.0, 134.9, 133.2, 133.0, 131.5, 130.8, 129.8, 129.3, 127.7, 127.4, 125.9, 120.2, 111.9, 110.0, 38.3, 24.7, 13.0. HRMS (ESI) (*m*/*z*): $[M + H]^+$ calcd for $C_{28}H_{27}S$ 395.1828; found, 395.1817.

(*E*)-2-Bromo-9,9-dihexyl-7-(2-(7-isopropyl-1-methylazulen-4-yl)vinyl)-9*H*-fluorene (3e). Green powder (mp. 88.0 – 90.0 ˚C, 34%) ^{1}H NMR ($CDCl_3$, 400 MHz) δ 8.20 (s, 1H), 8.06 (d, J = 16.1 Hz, 1H), 7.72 – 7.66 (m, 2H), 7.62 (dd, J = 7.9, 1.5 Hz, 1H), 7.59 – 7.44 (m, 8H), 3.11 (sept, J = 6.9 Hz, 1H), 2.69 (s, 3H), 1.99 (ddd, J = 11.5, 9.8, 6.3 Hz, 4H), 1.40 (d, J = 6.9 Hz, 6H), 1.18 – 1.00 (m, 12H), 0.77 (t, J = 7.0 Hz, 6H), 0.71 – 0.58 (m, 4H). ^{13}C NMR ($CDCl_3$, 100 MHz) δ 153.7, 151.4, 142.3, 140.9, 140.5, 140.1, 137.1, 137.0, 136.8, 135.3, 134.8, 133.5, 130.4, 129.4, 126.7, 126.6, 126.3, 121.8, 121.6, 121.5, 120.6, 120.5, 112.2, 55.8, 40.7, 38.7, 31.9, 30.0, 25.1, 24.1, 23.0, 14.4, 13.4. HRMS (ESI) (m/z): $[M + H]^+$ calcd for $C_{41}H_{50}Br$ 621.3091; found, 621.3096.

(*E*)-1-(2-(7-Isopropyl-1-methylazulen-4-yl)vinyl)pyrene (3f). Green foamy solid (mp. 108.0 – 110.0 ˚C, 70%). ^{1}H NMR ($CDCl_3$, 400 MHz) δ 8.51 – 8.40 (m, 3H), 8.26 – 8.15 (m, 5H), 8.11 (d, J = 9.2 Hz, 1H), 8.05 (s, 2H), 7.99 (d, J = 7.6 Hz, 1H), 7.74 – 7.54 (m, 4H), 3.12 (sept, J = 6.9 Hz, 1H), 2.72 (s, 3H), 1.43 (d, J = 7.1 Hz, 6H). ^{13}C NMR ($CDCl_3$, 100 MHz) δ 142.3, 140.5, 137.2, 137.1, 136.8, 135.2, 133.4, 132.0, 132.0, 131.7, 131.6, 131.2, 131.1, 129.0, 128.1, 127.8, 127.7, 126.3, 126.2, 125.7, 125.4, 125.4, 125.3, 125.1, 124.3, 123.2, 120.8, 112.3, 38.6, 25.0, 13.3. HRMS (ESI) (m/z): $[M + H]^+$ calcd for $C_{32}H_{27}$ 411.2107; found, 411.2110.

(*E*)-7-Isopropyl-1-methyl-4-(4-(phnylethynyl)styryl)azulene (3g). Green needles (mp. 100.0 – 102.0 ˚C, 32%). ^{1}H NMR ($CDCl_3$, 400 MHz) δ 8.26 (d, J = 1.9 Hz, 1H), 8.09 (d, J = 16.1 Hz, 1H), 7.75 (d, J = 3.8 Hz, 1H), 7.68 – 7.48 (m, 9H), 7.41 (ddd, J = 9.1, 4.9, 1.7 Hz, 4H), 3.16 (sept, J = 6.9 Hz, 1H), 2.75 (s, 3H), 1.45 (d, J = 6.9 Hz, 6H). ^{13}C NMR ($CDCl_3$, 100 MHz)

δ 141.7, 140.5, 137.4, 137.1, 137.0, 136.7, 135.1, 133.3, 133.3, 132.2, 131.8, 130.6, 128.6, 127.2, 126.2, 123.4, 123.2, 120.4, 112.2, 90.9, 89.7, 38.5, 24.9, 13.3. HRMS (ESI) (*m*/*z*): $[M + H]^+$ calcd for $C_{30}H_{27}$ 387.2107; found, 387.2112.

(*E*)-2-(2-(7-Isopropyl-1-methylazulen-4-yl)vinyl)furan (3h). Green oil (mp. 80.0 – 82.0 °C, 67%). ^{1}H NMR ($CDCl_3$, 400 MHz) δ 8.20 (d, *J* = 1.9 Hz, 1H), 7.97 (d, *J* = 16.1 Hz, 1H), 7.70 (dd, *J* = 3.9, 0.8 Hz, 1H), 7.56 – 7.48 (m, 3H), 7.43 (d, *J* = 11.1 Hz, 1H), 7.21 (d, *J* = 16.0 Hz, 1H), 3.08 (sept, *J* = 6.9 Hz, 1H), 2.71 (s, 3H), 1.41 (d, *J* = 6.9 Hz, 6H). ^{13}C NMR ($CDCl_3$, 100 MHz) δ 153.6, 143.3, 141.7, 140.3, 137.1, 136.6, 135.1, 133.3, 128.1, 126.3, 121.5, 112.0, 112.4, 112.3, 110.7, 38.97, 25.1, 13.4. HRMS (ESI) (*m*/*z*): $[M + H]^+$ calcd for $C_{20}H_{21}O$ 277.1587; found, 277.1587.

(*E*)-2-(2-(7-Isopropyl-1-methylazulen-4-yl)vinyl)thiophene (3i). Green powder (mp. 68.0 – 70.0 °C, 66%). ^{1}H NMR ($CDCl_3$, 400 MHz) δ 8.17 (s, 1H), 7.82 (d, *J* = 15.9 Hz, 1H), 7.69 – 7.64 (m, 1H), 7.55 – 7.38 (m, 4H), 7.27 (dd, *J* = 5.2, 0.9 Hz, 1H), 7.17 (dd, *J* = 3.4, 0.8 Hz, 1H), 7.09 – 7.01 (m, 1H), 3.08 (sept, *J* = 6.9 Hz, 1H), 2.67 (s, 3H), 1.37 (d, *J* = 6.9 Hz, 6H). ^{13}C NMR ($CDCl_3$, 100 MHz) δ 153.4, 143.1, 141.4, 140.1, 136.9, 136.3, 134.9, 133.1, 127.8, 126.1, 121.3, 119.7, 112.2, 112.1, 110.5, 38.4, 24.9, 13.2. HRMS (ESI) (*m*/*z*): $[M + H]^+$ calcd for $C_{30}H_{27}$ 293.1358; found, 293.1358.

(*E*)-1-Hexyl-2-(2-(7-isopropyl-1-methylazulen-4-yl)vinyl)-1*H*-pyrrole (3j). Green oil (71%). ^{1}H NMR ($CDCl_3$, 400 MHz) δ 8.14 (d, *J* = 2.0 Hz, 1H), 7.75 (d, *J* = 15.8 Hz, 1H), 7.62 (d, *J* = 3.9 Hz, 1H), 7.50 – 7.36 (m, 3H), 7.27 (s, 1H), 6.82 – 6.64 (m, 2H), 6.32 – 6.12 (m, 1H),

4.00 (t, *J* = 7.3 Hz, 2H), 3.08 (s, 1H), 2.66 (s, 3H), 1.77 (t, *J* = 7.1 Hz, 2H), 1.40 – 1.24 (m, 12H), 0.94 – 0.77 (m, 3H). ^{13}C NMR ($CDCl_3$, 100 MHz) δ 143.0, 139.9, 136.8, 136.4, 135.2, 133.4, 131.8, 126.6, 126.3, 124.2, 122.7, 120.2, 112.4, 109.2, 108.7, 47.7, 38.7, 32.1, 31.9, 27.0, 25.2, 23.0, 14.5, 13.6. HRMS (ESI) (*m*/*z*): $[M + H]^+$ calcd for $C_{26}H_{34}N$ 360.2686; found, 360.2697.

(*E*)-1-Ethyl-3-(2-(7-isopropyl-1-methylazulen-4-yl)vinyl)-1*H*-indole (3k). Green powder (mp. 74.0 – 77.0 ˚C,48%). ^{1}H NMR ($CDCl_3$, 400 MHz) δ 8.16 (s, 1H), 8.13 – 8.08 (m, 1H), 8.01 (d, *J* = 16.2 Hz, 1H), 7.68 – 7.59 (m, 2H), 7.58 – 7.46 (m, 3H), 7.42 (s, 1H), 7.37 (d, *J* = 1.4 Hz, 0H), 7.32 – 7.26 (m, 1H), 4.30 – 4.11 (m, 2H), 3.16 – 3.04 (sept, J = 7.0 1H), 2.67 (s, 3H), 1.56 – 1.49 (m, 3H), 1.38 (d, *J* = 7.0 Hz, 6H). ^{13}C NMR ($CDCl_3$, 100 MHz) δ 143.7, 139.6, 137.3, 136.6, 136.3, 135.2, 133.2, 128.5, 127.5, 126.0, 125.5, 122.8, 120.9, 120.9, 120.0, 115.0, 112.1, 110.2, 41.6, 38.6, 25.1, 15.7, 13.5. HRMS (ESI) (*m*/*z*): $[M + H]^+$ calcd for $C_{26}H_{28}N$ 354.2216; found, 354.2176.

(*E*)-9-Ethyl-3-(2-(7-isopropyl-1-methylazulen-4-yl)vinyl)-9*H*-carbazole (3l). Green foamy solid (mp. 88.0 – 90.0 ˚C, 75%). ^{1}H NMR ($CDCl_3$, 400 MHz) δ 8.36 (dd, *J* = 1.7, 0.6 Hz, 1H), 8.22 – 8.20 (m, 1H), 8.19 (ddd, *J* = 7.8, 1.2, 0.7 Hz, 1H), 8.08 (d, *J* = 16.1 Hz, 1H), 7.85 – 7.81 (m, 1H), 7.71 – 7.67 (m, 1H), 7.64 (d, *J* = 16.0 Hz, 1H), 7.61 – 7.49 (m, 4H), 7.48 – 7.43 (m, 2H), 7.32 – 7.28 (m, 1H), 4.42 (q, *J* = 7.2 Hz, 2H), 3.18 – 3.09 (m, 1H), 2.74 – 2.64 (m, 3H), 1.48 (t, *J* = 7.2 Hz, 3H), 1.42 (d, *J* = 6.9 Hz, 6H). ^{13}C NMR ($CDCl_3$, 100 MHz) δ 142.6, 140.5, 139.8, 136.8, 136.4, 136.2, 135.2, 135.0, 133.0, 128.6, 126.7, 126.1, 125.8, 125.1, 123.1,

120.7, 120.3, 119.7, 119.3, 112.0, 108.9, 108.8, 38.4, 37.7, 24.9, 13.9, 13.2. HRMS (ESI) (*m*/*z*): $[M + H]^+$ calcd for $C_{30}H_{30}N$ 404.2373; found, 404.2320

CHAPTER 2: EXTENDING Π-CONJUGATION OF GUAIAZULENE VIA RING ANNULATION OR PALLADIUM CATALYZED CROSS-COUPLING REACTIONS

Parts of this chapter appear in E. H. Ghazvini Zadeh, *et al. Eur. J. Org. Chem.* **2015**, 2271–2276.

2.1. Abstract

Guaiazulene reactive sites at C-3 and C-4 were exploited to generate a series of cyclopenta[*ef*]heptalenes **6a-c** that exhibit strong stimuli-responsive behavior. Though the synthesis of cyclopenta[*ef*]heptalenes has been reported in the literature, this described approach is versatile in that it allows for various substrates to be incorporated into the resulting cyclopenta[*ef*]heptalenes. The synthesis was optimized to a one-pot step that furnished a set of cyclopenta[*ef*]heptalenes **6a-c**, which was characterized via 1D and 2D NMR. In addition, UV-vis absorption profiles were obtained in neutral and acidic media, showing that the extension of conjugation at C(4) of the cyclopenta[*ef*]heptalene skeleton from X = H, **6a**, to X = CN, and 2-thiophenyl, **6b** and **6c**, respectively, resulting in longer absorption maxima and smaller optical energy gaps of the cyclopenta[*ef*]heptalenium cations **6a-c**$^{+}$. Additionally, in the presence of a UV-activated (< 300 nm) photoacid generator (PAG), protonation of **6c** can be indirectly achieved via intermolecular photoinduced electron transfer (PeT) from the excited state of **6c** to the PAG, upon which the latter undergoes photodecomposition resulting in the generation of acid. In a related study, guaiazulene methyl group at C-4 was employed to study the linear and non-linear

optical properties of 4-styrylguaiazulenes **3c**, **3m**, and **3o**, which have 4-hexylphenylether moiety as the π–donor with varying π-spacer. As predicted, increasing the conjugation results in a bathochromic shift for the protonated species. On the other hand, a trend of decreasing quantum yield was established for this set of 4-styrylguaiazulenes, which can be explained by the increasingly higher degree of flexibility.

2.2. Azulenes – Modular Building Blocks

There is an extensive growth in the research and development of organic materials whose optical, electronic, and conductive properties can be modulated upon application of external stimuli. The design of such chromophores has been based on various π-conjugated building blocks that are functionalized with electron donor or acceptor moieties, leading to extended push-pull chromophores.[33] Expanded π-conjugated organic materials are often known for poor physical and chemical stability, limiting their scope of application.[33,34] To address these drawbacks, significant efforts have been made to exploit the azulene framework as a modular building block for the synthesis of chromophores having stimuli-responsive behavior.[35] Similar to the various azure-blue derivatives of the bicyclic sesquiterpene – azulene, guaiazulene exhibits unique electronic and optical properties that allow for its use in charge-transport,[13,14] nonlinear optics,[15,16] and sensor applications.[17] Unlike other small aromatic hydrocarbons, guaiazulene exhibits a relatively large permanent dipole moment, owing to its fused electron–rich cyclopentadiene and electron–poor heptatriene skeleton (Figure 28).[18,19,21] Electronic

properties of the azulene core result in the domination of fluorescence from the S_2 excited state to the S_0 state, in violation of Kasha's rule,[35] and very low emission intensity from the S_1 to S_0 state. Treatment of guaiazulene with strong acids leads to the protonation of the cyclopentadiene ring at the unsubstituted 3-position and yields the tropylium cation, which is accompanied by a change in the radiative decay pathway from the $S_2 \rightarrow S_0$ to the $S_1 \rightarrow S_0$ transition in the protonated species.[22]

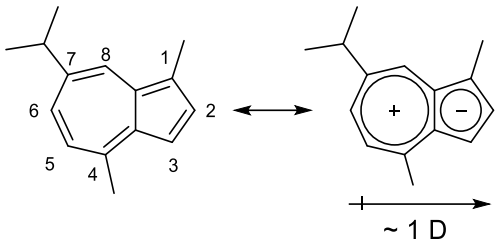

Figure 28. Resonance structures of guaiazulene with the numbering scheme and permanent dipole moment.

Various substitution patterns on the azulene core have been tailored in order to alter the azulene structure and understand the effect of acid doping on the optical and electronic properties of azulene-containing systems.[23-26] The selective synthesis of azulene derivatives having a single isomeric arrangement of functional groups at the 4- and 7-positions of the seven-membered ring was reported.[23] Such a connectivity pattern allowed for the incorporation of two thiophenyl groups at these positions *via* Stille coupling. The corresponding azulenium cation showed a significantly smaller energy gap with a concomitant red shift of the absorption maximum and a relatively strong $S_1 \rightarrow S_0$ fluorescence (Figure 29).[13-15]

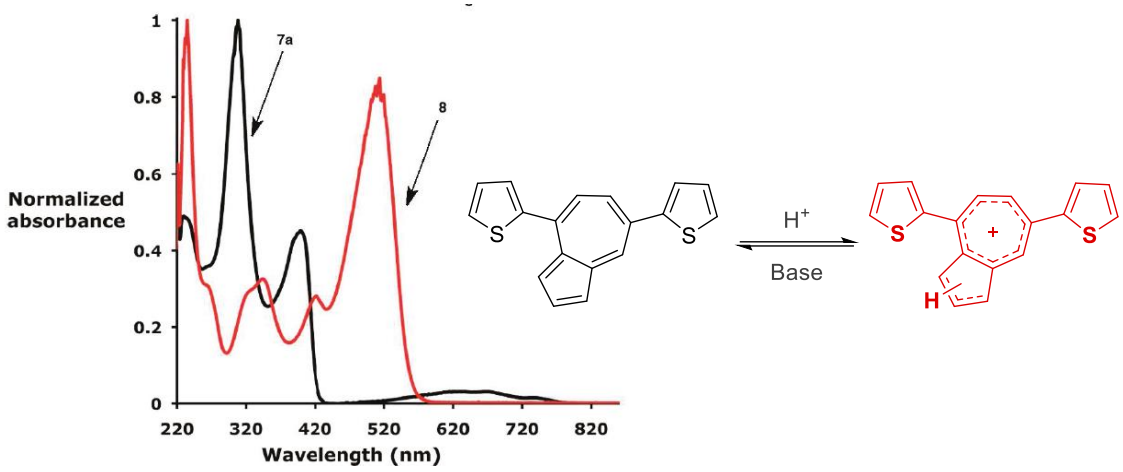

Figure 29. Formation of azulenium cations (red) from thiophene azulene oligomer (black). UV-vis absorption in DCM and DCM:TFA for neutral oligomer and protonated oligomer, respectively.

2.3. Annulation of Guaiazulene to Cyclopenta[*ef*]heptalenes

The extension of the azulene framework by annulation to form a stimuli-responsive π–conjugated polycyclic hydrocarbon has been modestly reported. Hafner used the immonium salts of 4,6,8-trimethylazulene-1-formaldehyde and 4,6,8-trimethylazulene-1-propenal to form via intramolecular cyclization the corresponding cyclopenta[*cd*]azulene and cyclopenta[*ef*]heptalene, respectively (Figure 30).[36] Recently, Wu and coworkers demonstrated a relatively lengthy method for the synthesis of two functionalized cyclopenta[*ef*]heptalenes,[37] and none of the prepared derivatives were fully conjugated throughout the skeleton (Figure 30). In addition, the doping of these tricyclic systems with acids has not yet been reported. We envisioned that a stimuli-responsive cyclopenta[*ef*]heptalene framework can be achieved by adopting a similar synthetic approach to the one reported by Wu.[37] As depicted in Figure 30, the

intermediate aldehyde is attacked by the enolate, leading to 7,8-dihydrocyclopenta[*ef*]heptalene. In this work, we employed the acidic protons of the Me group at C(4) of prepared guaiazulene-based acrylonitriles for the annulation of the fused 7-membered ring. This concomitantly introduces a basic amine on C(5) that is thought to be feasibly protonated by acids to generate a halochromic system.

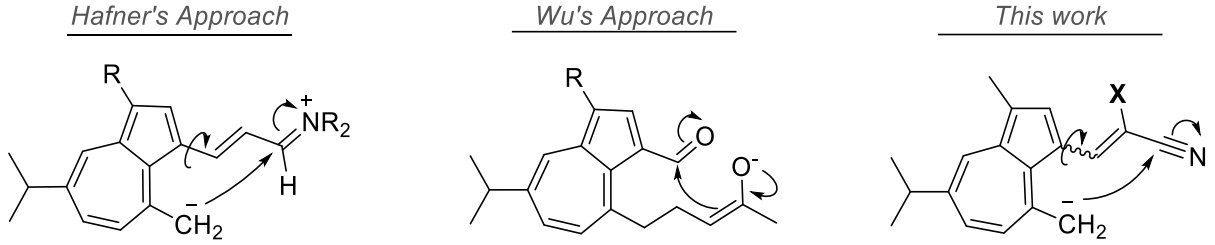

Figure 30. Ring formation via intramolecular cyclization.

When compared to previous literature procedures, the approach employed in this work is rather versatile in that it allows for various alkyl or (hetero)aryl groups to be installed on the C-4 position of cyclopenta[*ef*]heptalene skeleton, hence yielding an array of cyclopenta[*ef*]heptalenes that could enable study of photophysical structure-property trends.

2.4. Syntheses and NMR Characterization of Cyclopenta[*ef*]heptalenes 6a-c

The syntheses of cyclopenta[*ef*]heptalenes **6a-c** are shown in Scheme 2. Initially, 3-guaiazulenecarboxylaldehyde **1a** was condensed with acetonitriles **4a-c** in the presence of morpholine as a base to afford the corresponding guaiazulene-based acrylonitrile **5a-c**. Treatment of **5a-c** with two equivalents of ^{t}BuOK led to formation of the fused 7-

membered ring **6a-c**. The two-step synthetic route was reexamined in order to afford **6a-c** in a one-pot synthesis. Accordingly, condensation and ring formation were achieved when excess acetonitrile **4a-c** and ^{t}BuOK were used, leading to yields higher than those obtained via the step-wise approach.

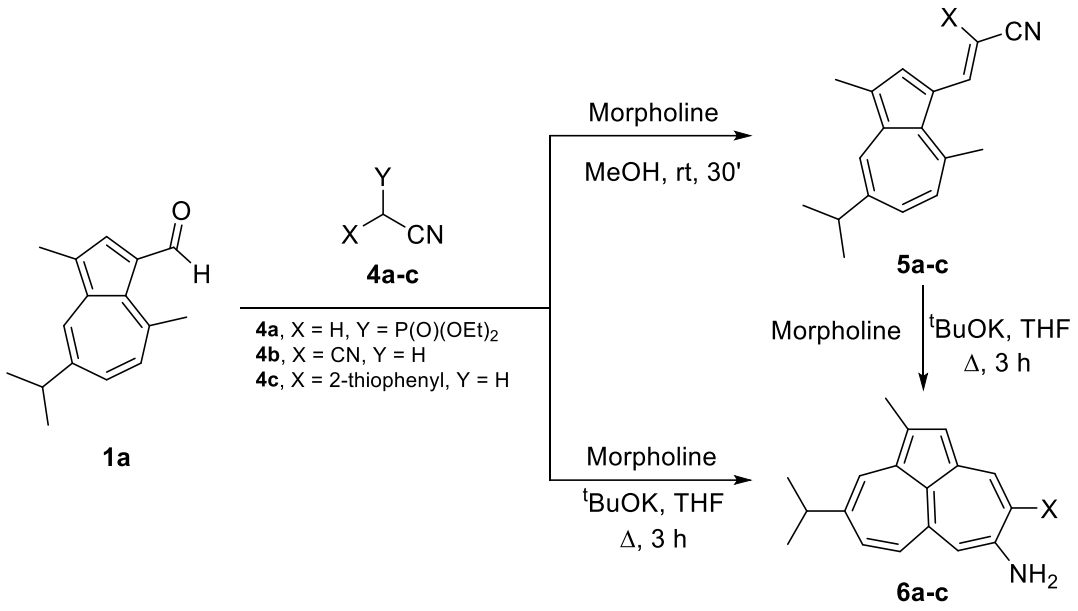

Scheme 2. Syntheses of **6a-c**.

We predicted that protonation with TFA would occur on the amine, as observed with various other aromatic compounds having exocyclic amines. However, a thorough NMR study, including COSY, ^{1}H-^{13}C HSQC, ^{1}H-^{15}N HSQC, HMBC, and INADEQUATE experiments, shows that protonation occurs at C(6), as evidenced by the presence of a CH_2 in the HSQC spectra of the protonated forms (Figure 31, inset). Further analysis of spectra corresponding to the neutral and protonated forms of **6** shows that all aromatic ^{1}H resonances appear at lower frequency than expected for aromatic systems, but shift

significantly to higher frequency when protonated (Figure 31). This suggests that the –NH_2 group does not behave as an aromatic amine, but rather as an enamine. This phenomenon can be interpreted by comparing the relative hardness of cyclopenta[*ef*]heptalene (0.285), azulene (0.439), and benzene (1.000). Coined by Parr and Zhou, relative hardness is an index used to identify aromatic, nonaromatic, and antiaromatic character of cyclic conjugated molecules, and incorporates high stability, low reactivity, and sustained induced ring current as defining measures of aromaticity.[38] Accordingly, the values of relative hardness suggest that **6** exhibits low aromatic character, which is consistent with the unusual low frequencies of aromatic ^{1}H resonances. Additionally, the higher frequencies of **6a-c**$^+$ ^{1}H resonances are comparable to those seen in azulene derivatives, suggesting that a larger sustained induced ring current exists, and hence a larger aromatic character for the protonated species.

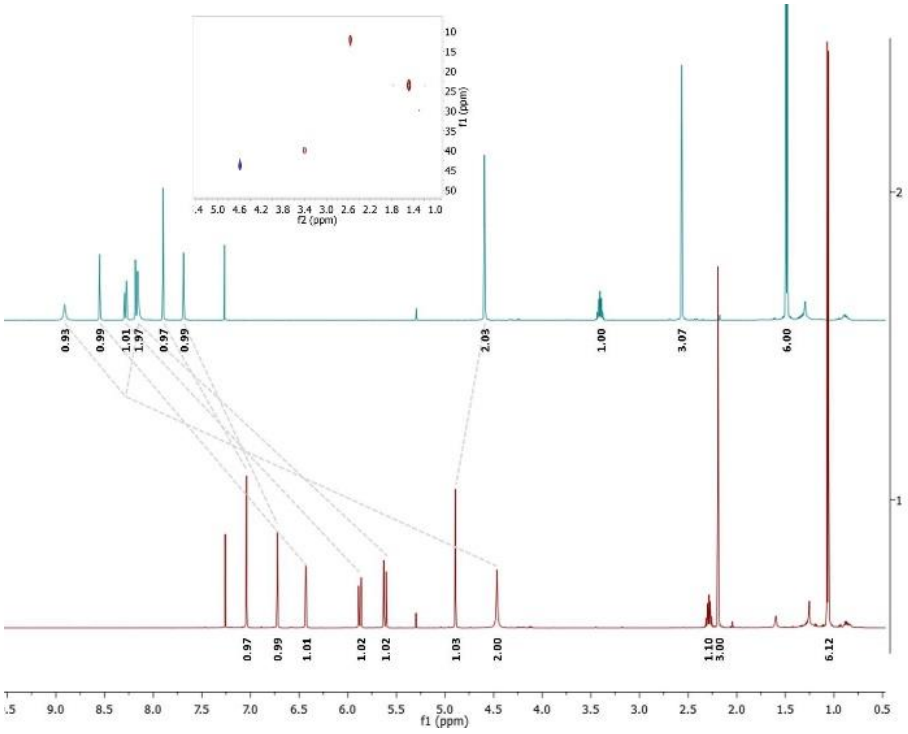

Figure 31. ^{1}H NMR spectra for 6b (red, $CDCl_3$) and **6b**$^{+}$ (blue, $CDCl_3$ + 1% TFA) with aliphatic ^{1}H-^{13}C HSQC spectrum for **6b**$^{+}$ (inset).

The resonances of cyclopenta[*ef*]heptalenes are assigned by analyzing the 1D and 2D NMR spectra, which became important to resolve any ambiguities, especially at C(2a), C(2a'), and C(10') in the cyclopenta[*ef*]heptalene skeleton (see Scheme 2 for numbering). The assignment was validated by directly observing the ^{13}C-^{13}C connectivity with an INADEQUATE experiment on **6b** (Figure 32). In the case of **4a**, protonation could potentially occur at either C(4) or C(6), which are at the β-position of the amine group. However, HMBC correlation between the ^{13}C resonance of C(7) and the CH_2 ^{1}H resonance indicated that protonation with TFA occurs at C(6).

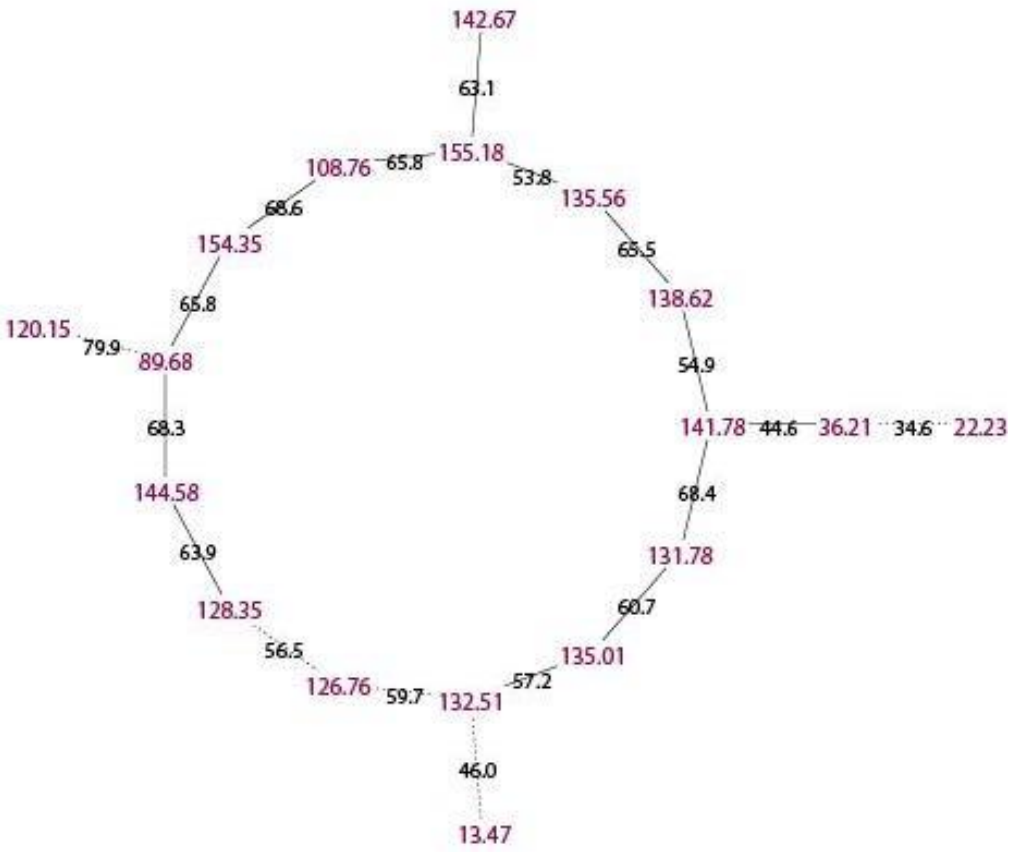

Figure 32. ^{13}C-^{13}C coupling network for 4b as determined by NMRanalyst.

2.5. UV-vis Absorption Study of Cyclopenta[*ef*]heptalenes

Examination of the UV-vis spectra of **6a-c** (Figure 33) in their neutral states (DCM) shows that all derivatives exhibit an absorption maximum at ~400 nm that corresponds to the S_0–S_2 transition, consistent with other reported azulenes (Figure 3a, Table 2).[18] It is notable, however, that there is little to no indication of the long wavelength absorption that corresponds to the $S_0 \rightarrow S_1$ transition seen in azulene derivatives.[23-26] Upon protonation of **6a-c**, there is a distinct bathochromic shift relative to the original π–π*

transitions (Figure 3b). The absorption maxima of the new broad peaks (574, 587, 609) are correlated with the extent of conjugation of the protonated heptalenes **6a-c+**, respectively.

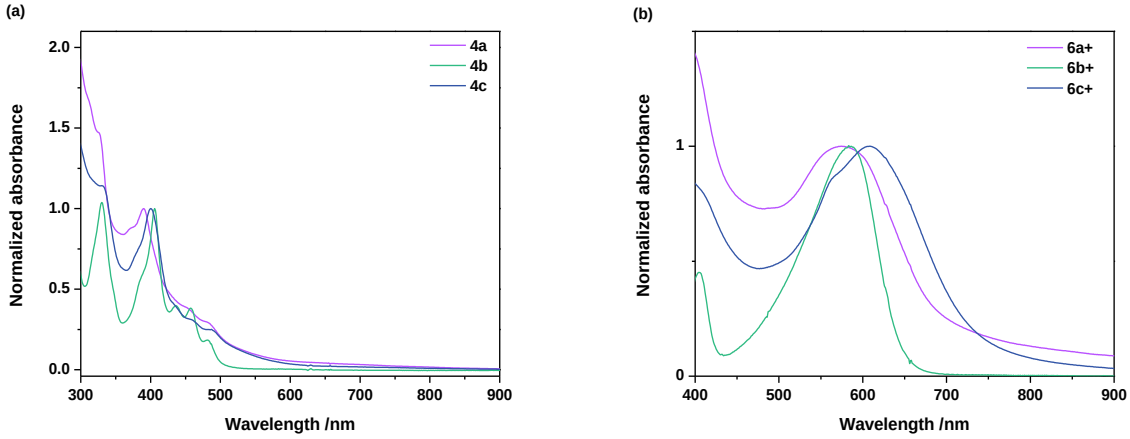

Figure 33. (a) Absorption spectra of **6a-c** in DCM, and (b) **6a-c**$^{+}$ in DCM:TFA (v:v, 9:1).

Extrapolating the onset wavelength of the absorption spectra of cyclopenta[*ef*]heptalenes in their neutral **6a-c** and protonated forms **6a-c+**, it is possible to estimate their corresponding optical energy gap, *E*g (Table 3).[29] It can be seen that the energy gap decreases through the series of derivatives, which is consistent with other azulene derivatives previously reported.[23]

Table 3. Spectral data for compounds 4a-c in DCM and DCM:TFA (v,v; 9,1)

4	Neutral			Protonated		
	λ_{max}^{abs} (nm)	λ_{onset}^{abs} (nm)	*E*g (eV)	λ_{max}^{abs} (nm)	λ_{onset}^{abs} (nm)	*E*g (eV)
a	390	498	2.49	574	647	1.92
b	406	510	2.43	586	692	1.79
c	400	521	2.38	609	752	1.65

2.6. Sensitization of Commercial PAG with Cyclopenta[*ef*]heptalenes

Inspired by reports that discuss the intramolecular photoinduced electron transfer (PeT) from the S_2 state of azulene to the excited state of various electron acceptors,[29] the possible intermolecular PeT of **6** to the excited state of a commercial PAG, diphenyliodonium hexafluorophosphate (DPIHFP), was investigated. Such a PAG is photoactivated at wavelengths ranging from the VUV to UV.[40] This presents a serious drawback, especially in certain applications as it limits their use to a spectral region that may overlap with functional groups that undergo, e.g., free radical photoinitiated polymerization.[41] As a proof of concept, sensitization of DPIHFP with **6** was investigated when **6c** was initially excited in the range of the S_0-S_2 transition (365 – 410 nm). Photoexcitation of **6c**/DPIHFP was recorded at 10 s intervals (Figure 34a). Acid generation was evident as the band at 580 nm, commonly observed in the UV-vis profile of **6c**$^+$, gradually emerges with a concomitant decrease in intensity at 400 nm. An isosbestic point observed at 465 nm is indicative of the presence of two inter-converting optically different phases in the solution.

Interestingly, excitation of a **6c**/DPIHEP solution at 532 nm is similar in manner to that observed in Figure 4a, yet provides better controlled sensitization of DPIHFP as result of lower absorptivity at longer wavelength (Figure 34b). In contrast, the use of a 254 nm excitation source allows for a direct excitation of DPIHFP. This was observed when **6c+** was obtained via phototitration of an equimolar ratio of **6c** and DPIHFP in

DCM using a 254 nm hand-held UV-lamp (Figure 34c) at 20 s intervals. Complete protonation was achieved in 80 s using direct excitation at 254 nm, while requiring ~ 3 min when excited at 405 nm, and ~ 8 min for 532 nm excitation. This suggests that **6a-c** can be used as sensitizers for commercial UV-activated PAGs.

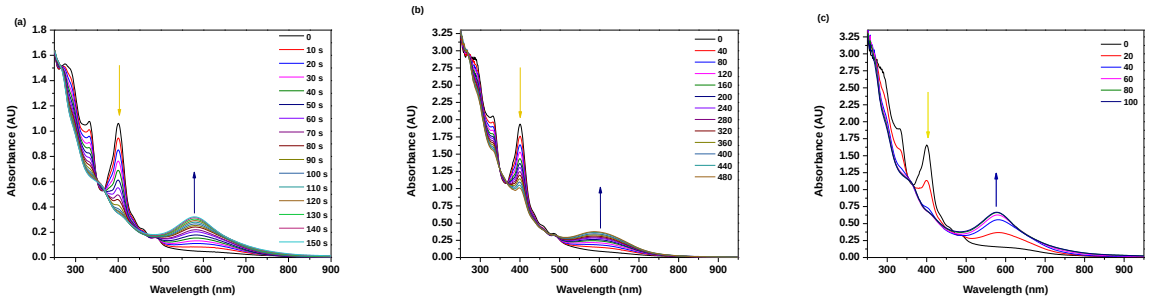

Figure 34. Absorption spectra recorded at (a) 10 s intervals of 4c/DPIHFP (3.7×10^{-4} M, 12.5 mW cm^{-2}, 405 nm), (b) at 40 s intervals of 4c/DPIHFP (1.25×10^{-3} M, 12.5 mW cm^{-2}, 532 nm) and (c) at 20 s intervals of **6c**/DPIHFP (1.1×10^{-3} M, 12.5 mW cm^{-2}, 254 nm).

2.7. Concluding Remarks and Future Work

In summary, we report a new approach towards the efficient synthesis of stimuli-responsive cyclopenta[*ef*]heptalenes **6** from naturally-occurring guaiazulene. Upon protonation with TFA, perturbation of the electronic states resulted in a switch from the dominant $S_0 \rightarrow S_2$ transition in the neutral state to the $S_0 \rightarrow S_1$ transition as seen in other reported azulene derivatives, where E_g of **6a-c**$^+$ is finely tunable by substituents at C(4). In addition UV-vis spectrometry demonstrated that **6** can act as a sensitizer of DPIHFP. This suggests that such cyclopenta[*ef*]heptalenes may be employed as visible sensitizers in a variety of applications of PAGs.

2.8. Effect of π–Spacer on the Linear and Non-Linear Photophysical Properties of Guaiazulene-terminated Chromophores

In the second part of this study, we aimed at preparing a set of guaiazulene-terminated chromophores having 4-hexylphenylether as the donor part of the molecule for investigating the effect conjugation length and the nature of π–spacer on the linear and non-linear properties of guaiazulenes **3c**, **3m**, and **3o** (Figure 35). We envisioned that using these results, an *in silico* study can be conducted, leading to the possibility of designing guaiazulene-terminated compounds with desirable properties, hence significantly limiting chemical wastes that result from the synthesis of target molecules with less appreciable properties.

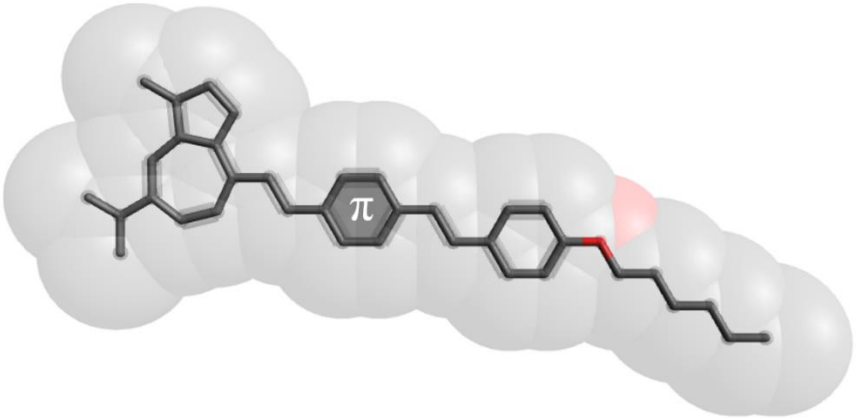

Figure 35. Structure of guaiazulene-terminated compounds with various π–spacers.

2.8.1. Synthesis of Guaiazulene-terminated Analogs 3c, 3m and 3o

The synthesis of **3c** is depicted in Scheme 3. Initially, 4-hydroxybenzaldehyde **A** was alkylated with 1-hexylbromide to afford **2c** in 90% yield. Purification of this intermediate was facilitated when a marginal excess of **A** was used; the reaction mixture

was then filtered and extracted with a saturated Na_2CO_3 solution, which eliminated the unreacted 4-hydroxybenzaldehyde **A**. **2c** was then used to prepare **3c** as described in Chapter 1.

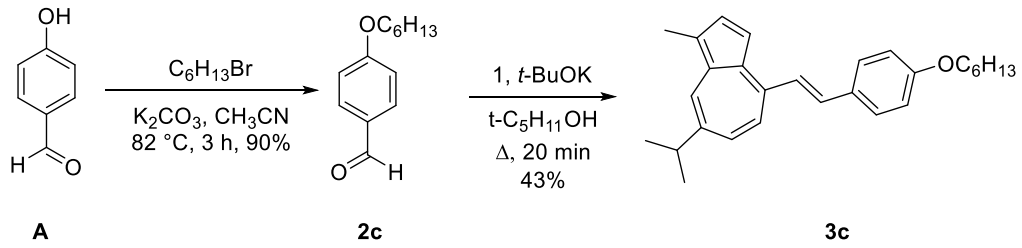

Scheme 3. Synthesis of **3c**.

The synthesis of guaiazulene-terminated chromophore **3m** is shown in Scheme 4. In this synthetic route, a Wittig reaction was employed to convert **2c** in **B** by condensing the former with methyltriphenylphosphonium bromide under basic condition. The vinyl group allowed **B** to be coupled to **2e**, which is prepared by lithium-halogen exchange reaction employing intermediate **C** in the presence of n-BuLi. The Heck coupling of **B** with **2e** yielded aldehyde **3l**, which was condensed with guaiazulene **1** as elaborated previously, affording guaiazulene-terminated analog **3m**.

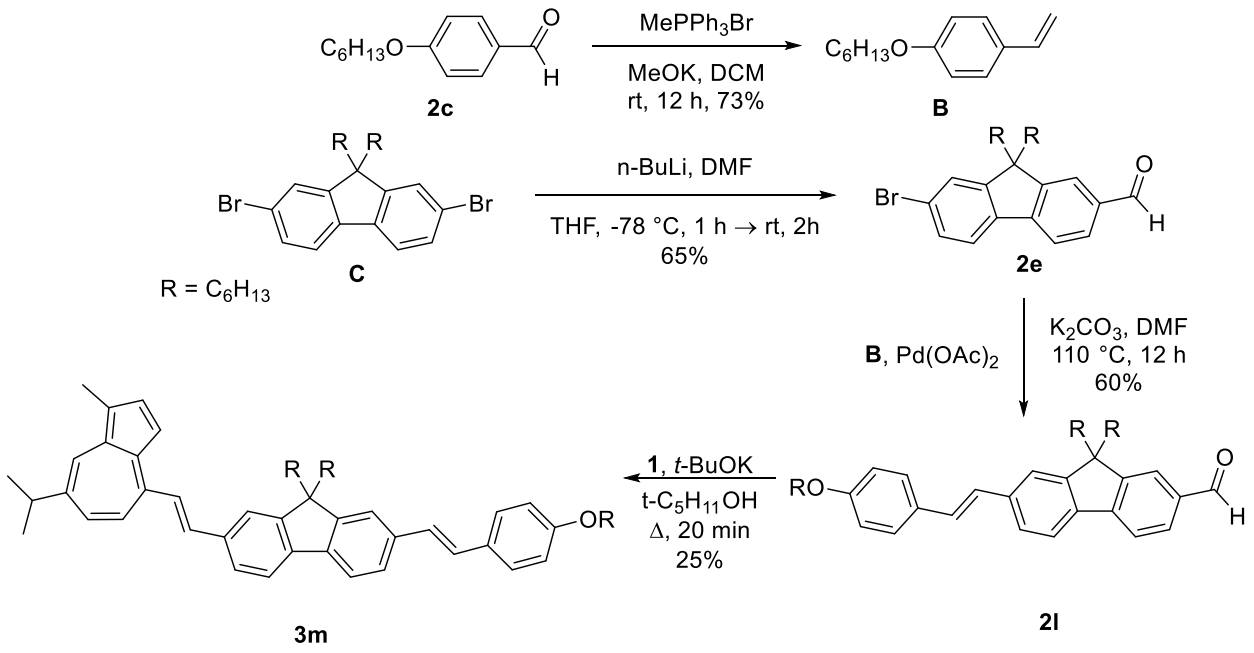

Scheme 4. Synthetic route towards **3m**.

Finally, **3o** was prepared starting with commercially available 5-bromothiophene-2-carbaldehyde **2m** and involved a convergent synthetic approach. Aldehyde **2m** was condensed with guaiazulene **1** under basic conditions to afford **3n**. This constituted the first segment that was later connect to vinyl-terminal intermediate **D** via a Heck cross-coupling reaction. In order to prepare the latter, aldehyde **3m** was condensed with methyltriphenylphosphonium bromide in a Wittig reaction as described above. Thus, a Heck coupling between **D** and **3n** afforded the target compound **3o**, which was isolated as green needles (Scheme 5). The intermediates and the target compounds were characterized by NMR spectroscopy (^{1}H and ^{13}C) and high resolution mass spectrometry.

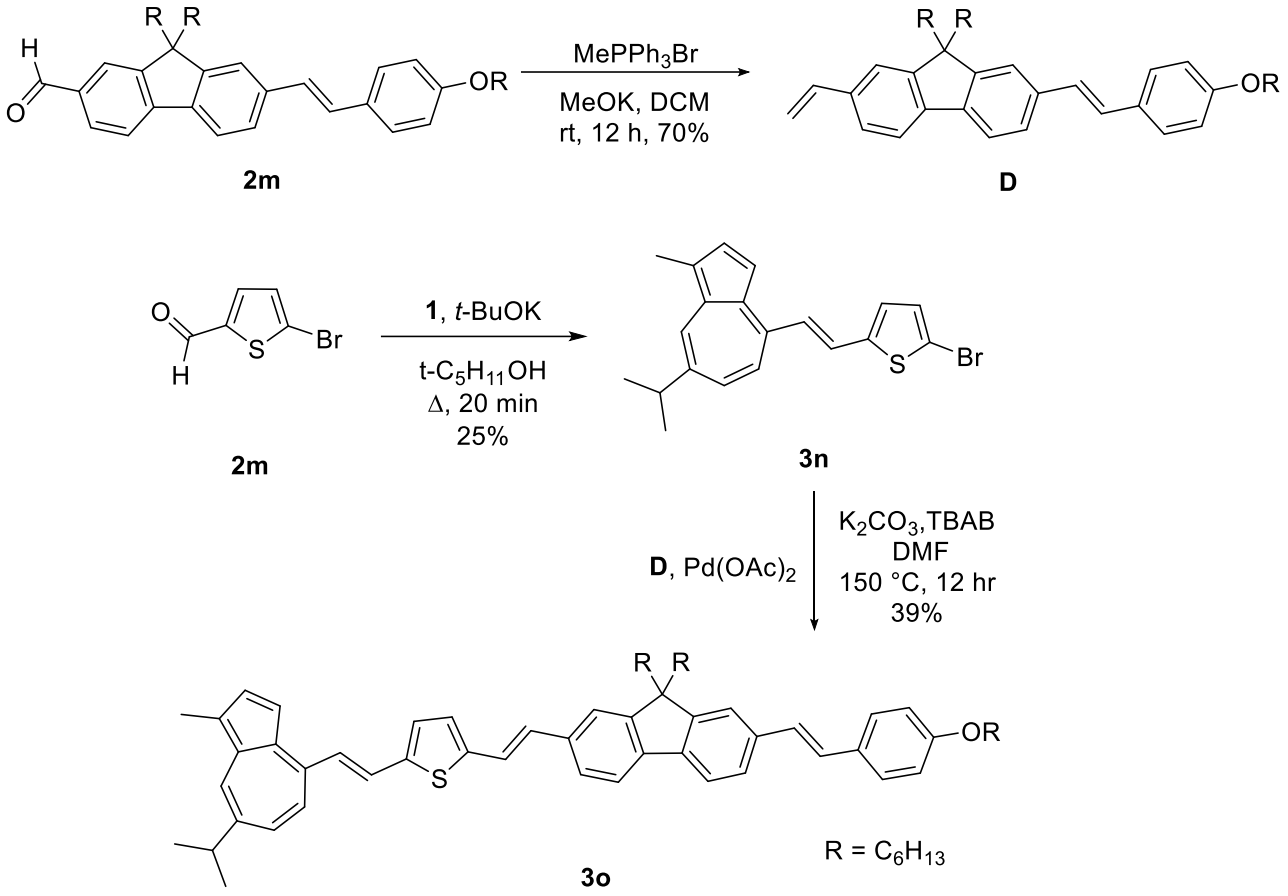

Scheme 5. Synthetic route towards **3o**.

2.8.2. Photophysical Characterization of 3c.

The absorption and emission profiles of (*E*)-4-(4-(hexyloxy)styryl)-7-isopropyl-1-methylazulene **3c** were described in Chapter 1. In methylene chloride, the various excitation wavelengths (365 nm and 650 nm) used to study the emission properties of 3c showed that this derivative is non-fluorescent. Conversely, the addition of TFA to the DCM solution of **3c** results in a dramatic changes, both in the absorption and emission

properties. The change in color from blue to reddish orange is reflected in the emergence of absorption band at 512 nm. The shift to an acidic medium results in switching the fluorescence on in the case of **3c**, with a λ_{max} = 619 nm. Using this band, excitation anisotropy was measured for the protonated species. The plateau of this trace through the main absorption band indicates that this is a single electronic transition. A summary of the photophysical properties measured for **3c** are listed as in Table 4.

Table 4. Photophysical parameters measured for **3c**, **3m**, and **3o** in DCM and 10% TFA/DCM, respectively.

	λ_{max}^{abs} [a] /nm	λ_{max}^{em} [a] /nm	$\Delta\lambda$ [b] /nm	ε [c] /10^3 M^{-1} cm^{-1}	Φ_f [d]	τ [e] /ns	Φ_{Ph} /10^{-6}
3a	294	- [f]	- [f]	29.3	- [f]	- [f]	1000
3a(H^+)	512	619	93	25.1	0.12	0.87	1.5
3m	410	500	90		0.01	1.76	
3m(H^+)	585	700	115		0.03	2.06	
3o	448	- [f]	- [f]	16.1	- [f]	- [f]	- [f]
3o(H^+)	385, 664	764	100	18.2, 16.9	0.01	1.52	13

[a] Absorption and emission maxima ±1 nm; [b] Stokes shift ±2 nm; [c] extinction coefficients ±5%; [d] fluorescence quantum yields ± 1%; [e] fluorescence lifetimes ±10%; [f] not determined.

The two-photon absorption spectrum recorded for **3c** shows a peak of ~170 GM at 1020 nm (Figure 36). This overlay with the linear absorption spectrum is not unexpected given the unsymmetrical design of the molecule. The quantum yields of photodecomposition measured for **3c** and **3c**(H^+) show significant disparity, separated by three orders of magnitude. Though a value is not explicitly stated, the photostability of guaiazulene has been investigated before; the sample showed greater photostability than

3c at an equivalent or greater irradiance but no quantitative value was reported. However, the use of DCM in the case of 3c in comparison with methanol for guaiazulene may cause such discrepancy, as the C–Cl bond in DCM is homolytically cleaved under UV light, resulting in active radical that can react with the guaiazulene moiety, which is reported to have anti-oxidant and anti-radical properties. On the other hand, longer wavelength excitation was used in the case of **3c**(H^+), hence minimizing radical formation resulting from solvent degradation.

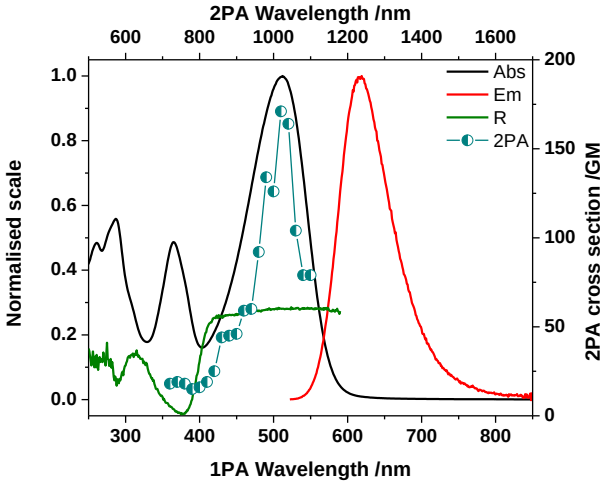

Figure 36. Absorption (black), emission (red), and 2PA spectra (turquoise points) for **3c** in 10% TFA/DCM, and excitation anisotropy (dark green) in acidified silicone oil.

2.8.3. TD-DFT Calculations toward the Design of Guaiazulene-terminated Chromophores with Predictable Photophysical Properties

The results obtained from studying the linear and non-linear properties of **3c** allowed for the design of various analogues with longer π-conjugation, and predicting their spectral properties through TD-DFT methods. Examination of the absorption

spectra generated through TD-DFT calculations shows that the weak intensity band characteristic of **3c** $S_0 \rightarrow S_1$ transition is manifested, though the bands at shorter wavelength appear to more resolved than observed in the experimental spectrum (Figure 37a). In the case of **3c**(H^+) (Figure 37b), the band centered at ~600 nm is anticipated by the calculation, however the short wavelength bands are less well aligned.

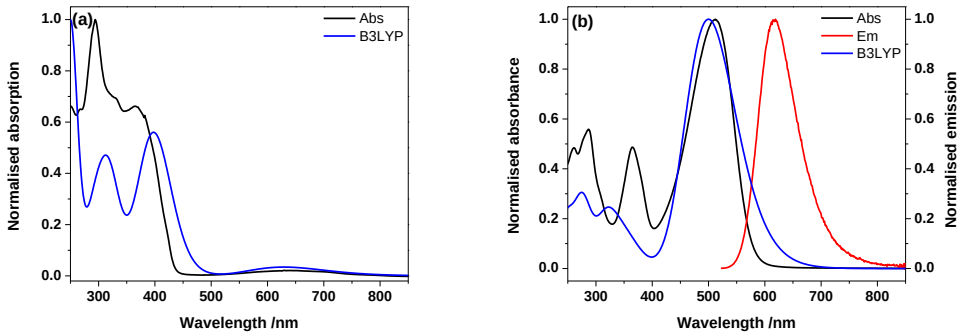

Figure 37. Calculated absorption spectra (blue) overlaid with experimental absorption (black) and emission (red) spectra for (a) **3c** and (b) **3c**(H^+).

The computed photophysical properties allowed us to design guaiazulene-terminated analogues **3m** and **3o**. The computed absorption and emission spectra for the corresponding guaiazulene-terminated analogues **3m** and **3o** showed potentially interesting properties. However, experimental results indicated that these computed spectra had some obvious discrepancies. For example, the emission λ_{max} calculated **3m**(H^+) differed by an additional 300 nm (~ 1000 nm), as compared to 700 nm for experimental spectrum (Figure 38 and 39).

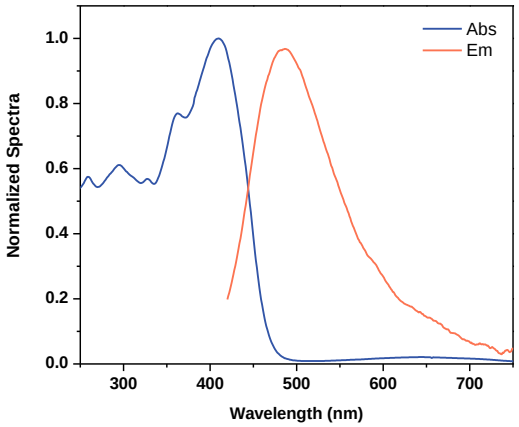

Figure 38. Absorption and emission spectra for **3m** in DCM.

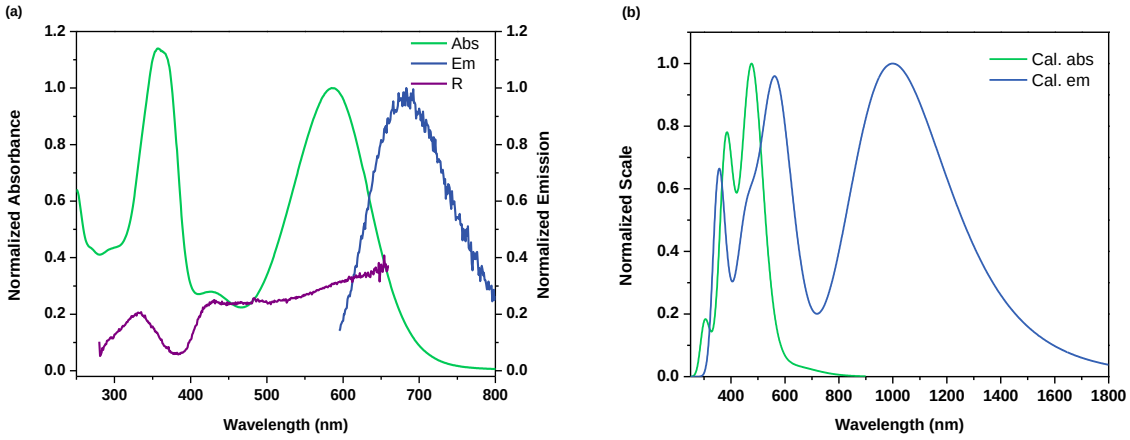

Figure 39. (a) Absorption (green) and emission (blue) for **3m** in 10% TFA/DCM, and excitation anisotropy (purple) for **3m** in acidified silicone oil. (b) Calculated absorption (green) and emission spectra of **3m**(H^+).

The one-photon absorption spectrum of **3o** (Figure 40a) shows a 100 nm hypsochromic shift compared to the calculated spectrum, and as such does not conceal the $S_0 \rightarrow S_1$ transition at ~ 650 nm. In the case of **3o**(H^+), a reasonable agreement is seen between the long wavelength band of the experiment data and the short band of the

calculated spectrum (Figure 40b). However, further probing into the band centered at ~1250 nm revealed no evidence of absorption at this wavelength. In addition, excitation of **3o**(H^+) at 664 nm results in a fluorescence band centered at 764 nm (Figure 40b), though the quantum yield of this emission is low (Table 4).

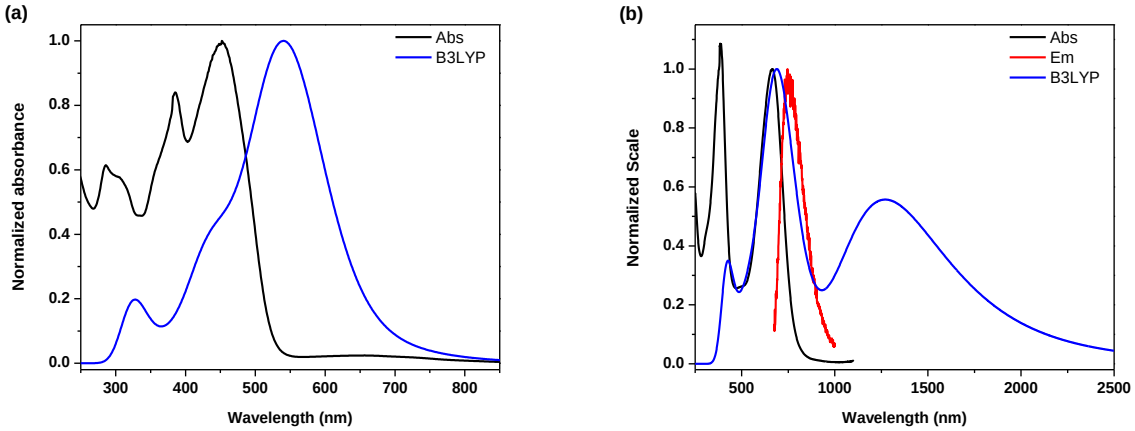

Figure 40. (a) Absorption (black) and emission (red) spectra recorded for 6 in DCM (a) and 6H in 10% TFA/DCM overlaid with their respective calculated absorption spectra (blue).

The increase in the photodecomposition quantum yield of **3o**(H^+) is nominal, though the compound was noted to have poor stability in solution over time, attributed to the combination of the thiophene and the acidic solution. In addition, the excitation anisotropy of **3o**(H^+) plateaus within the long wavelength absorption band, in accordance with a sole transition. This plateau also suggests that the absorption and emission are collinear (parallel transition dipoles), given its value of 0.4 (the theoretical maximum). The two-photon absorption spectrum of **3o**(H^+) recorded in 10% TFA/DCM initially

shows a reasonable agreement with the linear absorption spectrum, though appears erratic beyond 1300 nm (Figure 41).

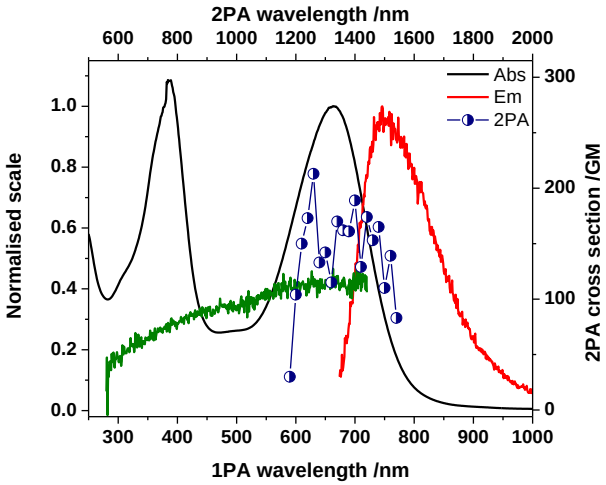

Figure 41. Absorption (black), emission (red), and 2PA spectra (dark blue points) for **3o**(H^+) in 10% TFA/DCM, and excitation anisotropy trace (dark green) in acidified silicone oil.

In an effort to resolve the difference observed between the experimental results and those of the B3LYP TD-DFT calculation, a series of additional methods were implemented. These methods include differing proportions of Hartree-Fock calculations. Such *ab intio* methods yield results that are less erratic than the semiempirical methods, though at the cost of time. Hybrid functions, including B3LYP (20% Hartree-Fock), have been developed to bridge this gap, where the ratios can be adjusted. With respect to spectroscopic data, increasing the *ab intio* portion blue shifts, or decreases, the wavelength reported for the first (longest wavelength) transition. The one-photon absorption calculated through the M06-HF (100% Hartree-Fock) method shows acceptable

correlation to the experimental, and the 2PA is to the same order of magnitude, with the same disparity as the one-photon absorption (Figure 42).

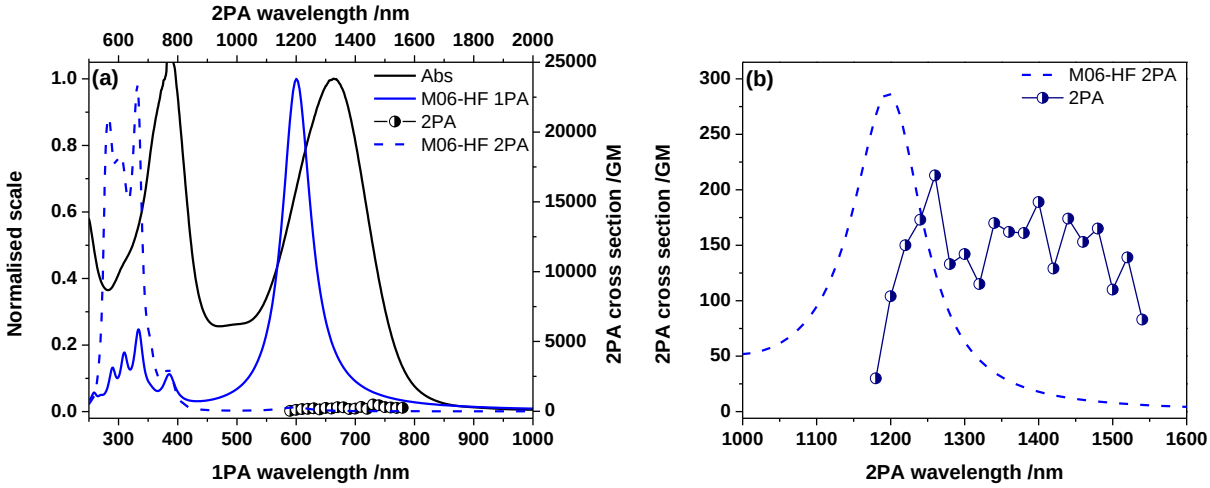

Figure 42. (a) Experimental (black) and M06-HF calculated one-photon absorption (solid blue), and experimental (dark blue points) and M06-HF calculated two-photon absorption (dashed blue); (b) an enlargement of 1000-1600 nm region of the 2PA spectrum.

2.9. Concluding Remarks and Future Work

The extension of π-conjugation of guaiazulene-terminated analogues shows a red-shifted absorption bands that rely on the length of conjugation. Unfortunately, the extended guaiazulenes showed weak fluorescence properties along with small 2PA cross-section. The low quantum yield recorded may be a consequence of increased vibrations that result from the extended geometry of the derivatives studied that allows for feasible rotation about single bonds. Our future work involves reducing rotation by constructing extended guaiazulene-terminated analogues where the vinyl spacer is substituted with

acetylenes. Alternatively, the aromatic rings can be joined via Pd-catalyzed cross coupling involving no spacers. Various structures can be synthesized to help tune the theoretical calculations in order to design chromophores with more accurately predicted properties.

2.10. Experimental Section

2.10.1. Photophysical Characterization

Linear photophysical properties were measured using prepared solutions (~ 10^{-6} M) in 10 mm quartz cuvettes using spectroscopic grade solvent. An Agilent 8453 was used to collect absorption spectra, while an Edinburgh Instruments FLS 980 for steady-state luminescence emission, excitation anisotropy, and fluorescence lifetimes. These measurements utilized a red-sensitive PMT, and a liquid-nitrogen-cooled Hamamatsu R5509-72; all measurements were corrected for detector response.

Fluorescence quantum yields were calculated using a relative method, with DPA (Φ_f = 0.95) as a reference.[9] Anisotropy measurements were performed in a viscous solvent, namely silicone oil, to hamper the rotational relaxation of the molecules. Photodecomposition quantum yields, Φ_{Ph}, were measured by irradiating into the main absorption band of solutions with LOCTITE 97034 UV-lamp (λ_{ex} = 366 nm, $I_0(\lambda) \approx$ 13 mW cm^{-2}), a green diode laser (λ_{ex} = 532 nm, $I_0(\lambda) \approx$ 98 mW cm^{-2}), or a red diode laser (λ_{ex} = 650 nm, $I_0(\lambda) \approx$ 62 mW cm^{-2}). Two-photon absorption spectra were collected through an open aperture z-scan setup using solutions (10^{-2} M) in 1 mm cuvette moved through the focal

point of the output beam of a OPA pumped by a 1 kHz, ~100 fs Coherent Inc. Legend Elite, in turn seeded by a Coherent Inc. Mira Ti-sapphire laser. Phototitrations of **6c** were performed in the presence of DPIHFP, and excited using a LOCTITE 97034 UV-lamp, a 532 nm diode laser, and a 254 nm hand-held UV-lamp

2.10.2. Synthesis

3-Formylguaiazulene (1a). Phosphorus oxychloride (5.00 mL, 53.0 mmol) was added to a solution of guaiazulene **1** (5.00 g, 25.0 mmol) in DMF at 0 °C under an inert atmosphere. After stirring in the ice bath for 1.5 h, the solution was carefully neutralized with conc. aqueous KOH solution. The purple solution was extracted with CH_2Cl_2 (3 × 50 mL), and the organic fractions were dried over Na_2SO_4 and evaporated under reduced pressure. The resulting crude oil was purified using column chromatography (hexanes: EtOAc, 3:1) to afford the title product **2** as purple solid (4.55 g, 20.1 mmol, 79%). ^{1}H NMR ($CDCl_3$, 400 MHz): δ 10.64 (s, 1H), 8.29 (d, J = 2.1 Hz, 1H), 8.23 (s, 1H), 7.59 (dd, J = 10.8; 2.1 Hz, 1H), 7.43 (d, J = 10.8 Hz, 1H), 3.16 (p, J = 7.0 Hz, 1), 3.15 (s, 1H), 2.59 (s, 1H), 1.39 (d, J = 7.0 Hz, 6H). ^{13}C NMR ($CDCl_3$, 100 MHz): δ 186.9, 147.5, 147.1, 144.1, 140.0, 139.7, 136.6, 136.0, 133.0, 128.0, 127.7, 38.7, 30.7, 25.1, 13.6.

2-((5-Isopropyl-3,8-dimethylazulen-1-yl)methylene)malononitrile (5a). *t*-BuOK (0.56 g, 5.0 mmol, 1.25 equiv) was added in small portions to a solution of 3-formylguaiazulene **1a** (0.90 g, 4.0 mmol) and diethyl (cyanomethyl)phosphonate **4a** (0.80 mL, 5.0 mmol) in anhyd. THF at 0 °C. The reaction mixture was allowed to warm to rt and then heated at

50 °C for 1h. The resulting green solution was dried under reduced pressure, and subsequently purified using column chromatography (hexanes: EtOAc, 4:1) to afford the title product **3a** as a green blue solid (1.00 g, 3.6 mmol, 92%). ^{1}H NMR ($CDCl_3$, 400 MHz, trans/cis: 2:1): δ 8.46 (s, 0.34H), 8.22 (d, J = 16.0 Hz, 0.63H), 8.12 (dd, J = 14.4, 1H), 7.94 (d, J = 11.6 Hz, 0.38 H), 7.72 (s, 0.62H), 7.39 (dd, J = 10.8; 2.0 Hz, 1H), 7.07 (d, J = 10.8 Hz, 1H), 5.53 (d, J = 15.6 Hz, 0.62H), 5.12 (d, J = 11.6 Hz, 0.36H), 3.09-3.02 (m, 1H), 2.93 (s, 3H), 2.59 (s, 1H), 2.56 (s, 2H), 1.34 (d, J = 6.8 Hz, 6H). ^{13}C NMR ($CDCl_3$, 100 MHz): δ 151, 146.7, 146.6, 146.4, 145.0, 145.0, 144.6, 143.1, 141.5, 137.8, 137.0, 136.5, 136.4, 135.9, 135.3 135.0, 131.3, 131.9, 128.1, 127.4, 122.6, 122.3, 121.3, 120.5, 89.9, 88.4, 38.4, 29.2, 25.0, 24.9, 13.5, 13.5. Calcd. for $C_{18}H_{19}N$ $[M + H]^+$ = 250.1591, exp. $[M + H]^+$ = 250.1564.

2-((5-Isopropyl-3,8-dimethylazulen-1-yl)methylene)malononitrile (5b). **1a** (0.90 g, 4.0 mmol) was added to a solution of malononitrile **4b** (0.33 g, 5.0 mmol, 1.2 equiv) and *N*-methylmorpholine (1 mL, 2.5 equiv) in methanol. After heating the resulting solution at 50 °C for 1h, the volatile material were evaporated under reduced pressure. The crude solid was purified using column chromatography (hexanes: EtOAc, 4:1) to afford the title product **3b** as dark yellow solid (1.00 g, 3.6 mmol, 90%). ^{1}H NMR ($CDCl_3$, 400 MHz): δ 8.63 (s, 1H), 8.46 (s, 1H), 8.28 (d, J = 2.2 Hz, 1H), 7.66 (dd, J = 10.8; 2.2 Hz, 1H), 7.48 (d, J = 10.8 Hz, 1H), 3.18 (sept, J = 6.9 Hz, 1H), 3.10 (s, 3H), 2.59 (s, 3H), 1.41 (d, J = 6.9 Hz, 6H). ^{13}C NMR ($CDCl_3$, 100 MHz): δ 151.2, 150.4, 147.9, 145.7, 141.7, 138.0, 137.6, 136.0, 135.8, 130.8, 121.3, 117.8, 116.8, 38.5, 29.6, 24.7.

3-(5-Isopropyl-3,8-dimethylazulen-1-yl)-2-(thiophen-2-yl)acrylonitrile (5c). The synthetic procedure for **5c** is similar to that described for **5a**. Purification of the crude reaction mixture using column chromatography (Hexanes: EtOAc, 5:1) afforded the title product as dark yellow solid (1.12 g, 3.4 mmol, 85%). ^{1}H NMR ($CDCl_3$, 400 MHz): δ 10.42 (s, 1H), 8.22 (s, 1H), 8.13 (s, 1H), 7.75 (dd, *J* = 16.0; 2.0 Hz, 1H), 7.61-7.60 (m, 1H), 7.21 (dd, *J* = 16.0; 2.0 Hz, 1H), 6.98-6.96 (m, 1H), 6.90 (dd, *J* = 4.4; 1.2 Hz, 1H), 3.14 (sept, *J* = 7.2 Hz, 1H), 2.56 (s, 3H), 1.38 (d, *J* = 7.2 Hz, 6H). ^{13}C NMR ($CDCl_3$, 100 MHz): δ 185.5, 147.4, 144.1, 144.0, 143.5, 140.3, 137.6, 136.0, 135.3, 132.6, 130.8, 128.0, 127.9, 127.2, 126.7, 126.5, 113.5, 38.3, 24.4, 12.9. Calcd. for $C_{22}H_{21}NS$ $[M + H]^+$ = 332.1468; found $[M + H]^+$ = 332.1440.

One pot synthesis of 9-isopropyl-1-methylcyclopenta[*ef*]heptalen-5-amine (6a). *t*-BuOK (2.24 g, 20.0 mmol) was added to a hot solution of **1a** (1.00 g, 4.4 mmol), **4a** (1.5 mL, 8.9 mmol) and morpholine (0.78 mL, 8.9 mmol) in dry THF (25 mL) was heated to reflux for 3 h. The formation of **6a** was monitored by TLC; interestingly, exposing the developed TLC to TFA vapor results in a rapid change in the color of the spot corresponding to 4a-c from pale yellow to purple-blue. The solution was cooled to rt and then diluted with DCM (50 mL) and washed with dilute HCl (2 N, 3 × 50 mL). The organic layer was dried over Na2SO4 and then evaporated under reduced pressure. The crude product was purified with silica column chromatography using hexanes: EtOAc (v:v, 5:1) to afford the title product as a dark yellow oil (15% for step-wise; 59% for one-pot). ^{1}H NMR ($CDCl_3$, 400 MHz): δ 6.74 (d, J = 10.8 Hz, 1H), 6.64 (s, 1H), 6.39 (d, *J* = 2.0 Hz, 1H), 5.70 (dd, *J* = 12.4;

2.0 Hz, 1H), 5.43 (d, *J* = 12.4 Hz, 1H), 4.94 (dd, *J* = 10.8; 2.4 Hz, 1H), 4.84 (d, *J* = 2.4 Hz, 1H), 3.72 (br s, 2H), 2.24-2.17 (m, 4H), 1.04 (d, *J* = 6.8 Hz, 6H). ^{13}C NMR ($CDCl_3$, 100 MHz): δ 155.8, 144.2, 141.3, 138.7, 133.7, 133.1, 129.9, 129.3, 129.2, 123.8, 111.4, 109.9, 36.5, 22.8, 13.8. Calcd. for $C_{18}H_{19}N$ $[M + H]^+$ = 250.1591, found $[M + H]^+$ = 250.1579.

Synthesis of 8-amino-4-isopropyl-2-methylcyclopenta[*ef*]heptalene-9-carbonitrile (6b) from (6b). *t*-BuOK (0.22 g, 2.0 mmol) was added to a solution of **6b** (0.55 g, 2.0 mmol) in anhyd. THF (10 mL). The solution was heated with reflux for 12 h, and then cooled to rt. The solvent was evaporated and the resulting crude was dissolved with DCM (20 mL) and was washed with dilute HCl (2 N, 3 × 50 mL). The organic layer was dried over Na_2SO_4, and was evaporated to dryness. Column chromatography (Hexanes: DCM; 3:1) was used to isolate the title product as a dark yellow solid (23% for stepwise vs 71% for one-pot). ^{1}H NMR ($CDCl_3$, 400 MHz): δ 6.74 (s, 1H), 6.44 (d, *J* = 2.0 Hz, 1H), 5.88 (dd, *J* = 12.4; 2.0 Hz, 1H), 5.62 (d, *J* = 12.4 Hz, 1H), 4.90 (s, 1H), 4.45 (br s, 2H), 2.29 (p, *J* = 6.8 Hz, 1H), 2.20 (s, 3H), 1.07 (d, *J* = 6.8 Hz, 6H). ^{13}C NMR ($CDCl_3$, 100 MHz): δ 154.7, 154.4, 144.2, 142.6, 142.5, 138.2, 137.8, 134.2, 132.3, 130.1, 129.9, 128.2, 127.2, 127.7, 125.1, 124.3, 114.0, 109.5, 36.2, 22.5, 13.5. Calcd. for $C_{19}H_{18}N_2$ $[M + H]^+$ 275.1543; found $[M + H]^+$ = 275.1503.

Isopropyl-2-methyl-9-(thiophen-2-yl)cyclopenta[*ef*]heptalen-8-amine (6c). Golden yellow solid (21% for stepwise vs 92% for one-pot). ^{1}H NMR ($CDCl_3$, 400 MHz): δ 7.25 (dd, *J* = 5.2; 1.2 Hz, 1H), 7.00 (dd, *J* = 5.2; 3.6 Hz, 1H), 6.95 (s, 1H), 6.93 (dd, *J* = 3.6; 1.2 Hz,

1H), 6.62 (s, 1H), 6.36 (d, *J* = 2.0 Hz, 1H), 5.71 (dd, *J* = 12.4 Hz, 1H), 5.46 (d, *J* = 12.4 Hz, 1H), 4.92 (s, 1H), 4.14 (br s, 2H), 2.26-2.17 (m, 4H), 1.05 (d, *J* = 6.8 Hz, 6H). ^{13}C NMR ($CDCl_3$, 100 MHz): δ 154.8, 154.2, 144.3, 142.8, 142.6, 138.4, 137.9, 133.9, 132.5, 130.1, 130.1, 128.3, 127.1, 126.7, 125.1, 124.3, 114.0, 109.3, 36.2, 22.4, 13.5. Calcd. for $C_{22}H_{21}NS$ $[M + H]^+$ = 332.1468; found $[M + H]^+$ = 332.1440.

9,9-Dihexyl-2-((*E*)-4-(hexyloxy)styryl)-7-((*E*)-2-(7-isopropyl-1-methylazulen-4-yl)vinyl)-9*H*-fluorene (3m). Green solid (25%, 72.0 – 75.0 °C). ^{1}H NMR ($CDCl_3$, 400 MHz): δ 8.20 (d, *J* = 1.4 Hz, 1H), 8.06 (d, *J* = 16.1 Hz, 1H), 7.73 – 7.61 (m, 4H), 7.59 – 7.44 (m, 9H), 7.19 – 7.04 (m, 2H), 6.95 – 6.87 (m, 2H), 3.99 (t, *J* = 6.6 Hz, 2H), 3.12 (p, *J* = 6.9 Hz, 1H), 2.70 (s, 3H), 2.04 (dd, *J* = 11.3, 5.7 Hz, 4H), 1.87 – 1.73 (m, 2H), 1.48 (dd, *J* = 10.5, 4.8 Hz, 2H), 1.40 (d, *J* = 6.9 Hz, 6H), 1.38 – 1.31 (m, 4H), 1.16 – 1.03 (m, 11H), 0.95 – 0.90 (m, 4H), 0.81 – 0.65 (m, 10H). ^{13}C NMR ($CDCl_3$, 100 MHz): δ 159.2, 152.1, 152.0, 140.3, 137.0, 136.4, 135.2, 135.0, 130.5, 128.9, 128.1, 128.0, 127.4, 126.2, 125.8, 121.7, 120.9, 120.6, 120.4, 120.3, 115.1, 77.6, 68.5, 55.4, 40.9, 38.7, 32.0, 31.9, 30.1, 29.6, 26.1, 25.1, 24.2, 23.0, 14.4, 14.4, 13.4. Calcd. for $C_{55}H_{68}O$ $[M + H]^+$ = 745.5343; found $[M + H]^+$ = 745.5189.

2-((*E*)-2-(9,9-Dihexyl-7-((*E*)-4-(hexyloxy)styryl)-9*H*-fluoren-2-yl)vinyl)-5-((*E*)-2-(7-isopropyl-1-methylazulen-4-yl)vinyl)thiophene (3o). Green solid (39%, 154.0 – 156.0 °C). ^{1}H NMR ($CDCl_3$, 400 MHz): δ.18 (d, *J* = 1.8 Hz, 1H), 7.82 (d, *J* = 15.8 Hz, 1H), 7.73 – 7.60 (m, 3H), 7.53 – 7.41 (m, 10H), 7.27 (dd, *J* = 16.0, 0.7 Hz, 1H), 7.19 – 7.00 (m, 5H), 6.90 (d, *J*

= 8.7 Hz, 2H), 3.98 (t, *J* = 6.6 Hz, 2H), 3.10 (p, *J* = 6.9 Hz, 1H), 2.72 – 2.64 (s, 3H), 2.07 – 1.93 (m, 4H), 1.85 – 1.75 (m, 2H), 1.52 – 1.43 (m, 2H), 1.37 (m, 10H), 1.19 – 0.99 (m, 11H), 0.95 – 0.88 (m, 4H), 0.80 – 0.73 (t, *J* = 8.0 Hz, 6H), 0.73 – 0.63 (m, 4H). Calcd. for $C_{55}H_{68}O$ $[M + H]^+$ = 852.5304; found $[M + H]^+$ = 852.5373.

CHAPTER 3: PHOTOPHYSICS AND BIOCONJUGATION OF FLUORESCENT WATER-SOLUBLE TWO-PHOTON ABSORBING DIKETOPYRROLOPYRROLE DYES

Parts of this chapter appear in E. H. Ghazvini Zadeh, *et al. J. Phys. Chem. C.* **2015**, *119*, in press.

3.1. Abstract

A myriad of applications have been demonstrated as a result of the synthetic feasibility, ease of modification, outstanding robustness, and attractive spectroscopic properties of diketopyrrolopyrrole (DPP) based chromophores. Toward a comprehensive linear photophysical and nonlinear optical characterization of diketopyrrolopyrroles, two derivatives, 2-(2-ethylhexyl)-3,6-di(pyridin-2-yl)-2,5-dihydropyrrolo[3,4-*c*]pyrrole-1,4-dione **9** and 2-(10-azidodecyl)-3,6-di(thiophen-2-yl)-2,5-dihydropyrrolo[3,4-*c*]pyrrole-1,4-dione **13**, were prepared. In addition to the various optical experiments performed to characterize these two derivatives, which include experimental excitation anisotropy spectra, 3D fluorescence maps, emission lifetimes, and photochemical decomposition quantum yields in a number of organic solvents, quantum chemical calculations were used to determine the nature of the main linear absorption bands of **9** and **13**. Further characterization included determining the two-photon absorption (2PA) spectra of **9** and **13** in a broad spectral range using 1 kHz femtosecond open aperture Z-scan technique, which show a maximum cross section of ~ 100 GM was shown. In addition, it was notable that transient absorption and stimulated emission pump-probe

measurements with femtosecond time resolution revealed two different types of fast relaxations in the excited states of **9** and **13**. This allowed for the determination of the one-photon stimulated emission depletion (STED) spectra. In that regard, efficient superfluorescence emission of **9** was observed under femtosecond transverse pumping conditions. In order to culminate on these results, we attempted the preparation of water-soluble DPP chromophores with extended conjugation that can be employed in bioimaging applications.

3.2. Fluorescent Molecules: Glowing Nanolamps for Sharper Bioimaging

Fluorescent chromophores have enabled scientists to monitor the interplay between biomolecules inside cells and observe disease-related proteins aggregate as well as track cell division at the nanolevel. However, bioimaging at such a level was not possible with simple optical microscopy techniques. Prior to the advent of methods in fluorescence microscopy,[44-51] optical microscopes prevented biologists to distinguish details of important cellular proteins and study relevant cellular processes. This limitation was described by the microscopist Ernst Abbe,[52] who published an equation demonstrating that the microscope resolution is limited by, among other factors, the wavelength of the light, and hence objects smaller than 0.2 μm could not be observed under a microscope (Figure 43).

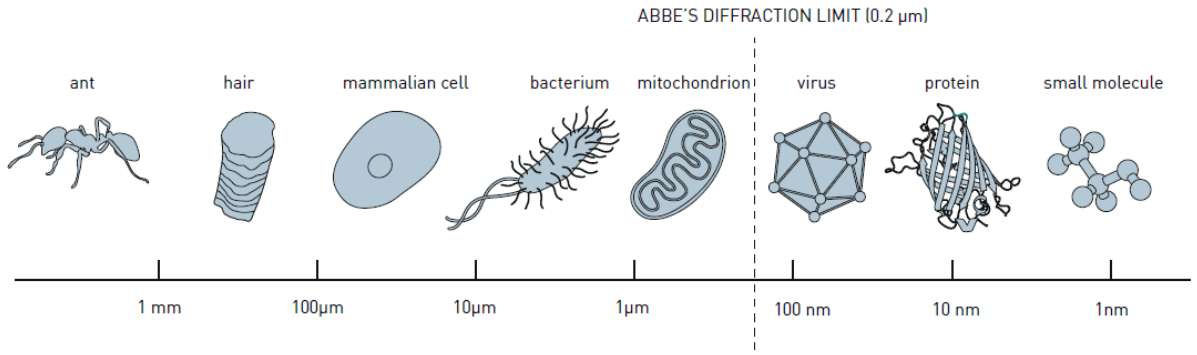

Figure 43. Abbe's diffraction limit inhibited the ability to discern nanomaterials such as viruses or single proteins**.**

In recent years, several scientists have proposed methods to overcome Abbe's diffraction barrier of light using far-field optics.[44-51] Among whom was Stephan Hell, whose proposed method, the so-called *stimulated emission depletion (STED)*, involves two overlapping synchronized laser beams, excitation and depletion.[44-47] The two pulses reach the sample position successively where the excitation laser excites and the second (STED laser) depletes the excitation within the sample. Stimulated emission arises in the region where both laser beams overlap, while fluorescence is observed only in the focal region where only the first excitation beam exists (Figure 44).

The choice of fluorophore susceptible to stimulated emission depends on certain physical properties such as photostability and suitable combinations of pulsed laser lines for both excitation and depletion. Toward that goal, a comprehensive investigation of the linear photophysical, photochemical and nonlinear optical properties of two diketopyrrolopyrrole dyes, including two-photon absorption (2PA), femtosecond

transient absorption and stimulated emission spectroscopy, and superfluorescence phenomena are presented in the second part of this work. The studied dyes show great potential for fluorescence microscopy applications, including high resolution STED microscopy.

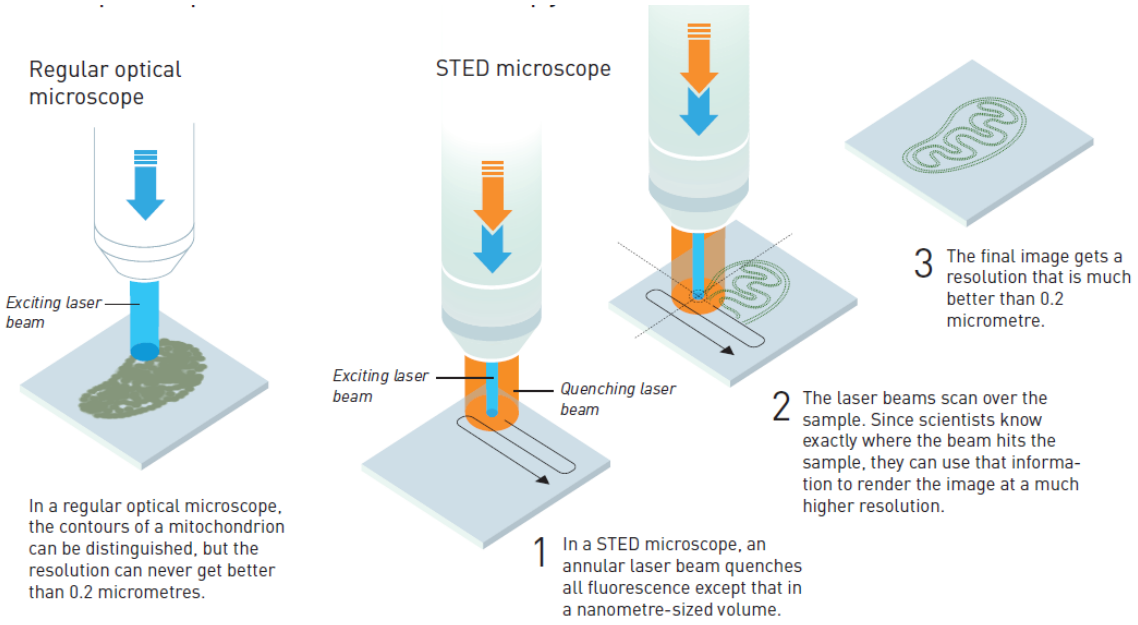

Figure 44. The principle of STED microscopy.[47]

3.3. Diketopyrrolopyrrole (DPP)-based Chromophores for Practical Applications

Diketopyrrolopyrrole (DPP) derivatives are well-known molecular structures with great potential for practical application in various pigments-employed industries,[53,54] organic electronics,[55-57] metal ion sensing,[58] laser active media,[59,60] and one- and two-photon fluorescence microscopy techniques.[61-63] The nature of these DPP derivatives has incited great interest in synthesis, study of linear spectroscopic, photochemical and non-linear optical properties, as well as fundamental investigation of

electronic structures for greater understanding and further novel application. A number of interesting properties were revealed for DPP-based media, including aggregation enhanced fluorescence emission,[64] adjustable thin-film crystallinity for use in organic photovoltaics,[57] efficient photoinitiating abilities for cationic polymerization of epoxides and free radical polymerization of acrylates,[65] and excellent self-assembling resulting in well-organized domain structures,[66] The effects of different donor/acceptor substituents on the optical properties of DPP derivatives were investigated[67-71] and the role of intramolecular hydrogen bonds in DPP structures was demonstrated.[72]

The wide array of applications discussed previously stem from the remarkable spectroscopic properties of the DPP bis(lactam) backbone. While some of these properties have not been systematically described in the literature, other characteristics may require a more elaborate and accurate study. For instance, the nature of the excited state absorption (ESA) of DPP derivatives, along with their fast relaxation processes in the ground and excited state,[73] are scarcely addressed in the scientific literature and require further investigation. In addition, the photochemical stability of DPP-based structures was studied by means of relative comparison with standard molecules[64] and/or by the measurements of temporal changes in the fluorescence or lasing intensities during irradiation.[63,74] In these cases, the majority of the presented data on photochemical stability are strictly dependent on the employed experimental conditions and cannot be considered as molecular parameters. Hence, we believe that the values of the

photodecomposition quantum yields should be determined for a more accurate characterization of the photochemical stability.[75]

In its first part, the following chapter details a comprehensive investigation of the linear photophysical, photochemical and nonlinear optical properties of DPP-based derivatives 2-(2-ethylhexyl)-3,6-di(pyridin-2-yl)-2,5-dihydropyrrolo[3,4-*c*]pyrrole-1,4-dione **9** and 2-(10-azidodecyl)-3,6-di(thiophen-2-yl)-2,5-dihydropyrrolo[3,4-*c*]pyrrole-1,4-dione **13**, including two-photon absorption (2PA), femtosecond transient absorption and stimulated emission spectroscopy, and superfluorescence phenomena. Compounds **9** and **13** exhibited great potential for fluorescence microscopy applications, including high resolution stimulated emission depletion (STED) microscopy. However, since water-solubility is a prerequisite for their use in relevant bioimaging applications, efforts toward preparing water-soluble and fluorescent red-emitting DPP-based chromophores are discussed in the latter part of this chapter.

3.4. Investigating the Linear Photophysical, Photochemical and Nonlinear Optical Properties of 9 and 13

3.4.1. Synthesis of 9 and 13.

Although the synthesis of DPP intermediates **8** and **11** is reported previously,[76-78] there is no report of use of 18-crown-6 ether as means to enhance both yields and purity of the resulting DPP (Scheme 6). This simple modification yields **8** and **11** in 81% and 74%, respectively, as compared to 30% and 21% when no ether is added. Monoalkylation

of **8** and **11** with lipophilic solubilizing groups, 2-ethylhexylbromide and 1,10-dibromodecane, was not efficient using K_2CO_3, as the bisalkylated products predominate. Therefore, ^{t}BuOK was added instead to generate the conjugated anion. This results in various red impurities that can be eliminated by tedious column chromatography. In order to avoid such undesired products, alkyl bromide was introduced to the reaction mixture prior to the addition of t-BuOK. Consequently, better alkylation yields and cleaner reaction mixture. In the case of thiophene-substituted DPP **11**, the isolation of pure monoalkylated product **12** proved cumbersome. Therefore, substitution of the Br-group of **12** with N_3 both aid in isolating a pure product and to function as a handle for further functionalization of **13**.

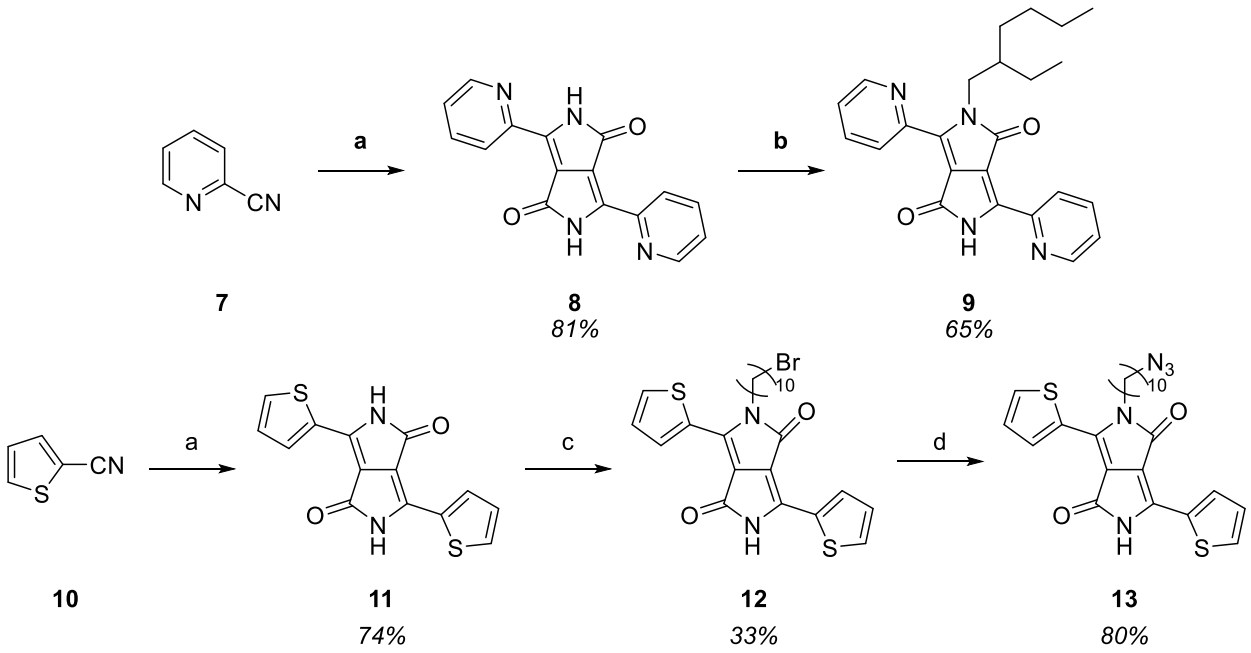

Scheme 6. (a) Diethyl succinate, ^{t}BuOK, 18-crown-6 ether, *t*-$C_5H_{11}OH$, 110 °C, 2 h; (b) 2-ethylhexyl bromide, ^{t}BuOK, 18-crown-6 ether, DMF, 100 °C, 12 h; (c) 1,10-dibromodecane, ^{t}BuOK, 18-crown-6 ether, DMF, 100 °C, 12h; (d) NaN_3, DMF, 80 °C, 3 h.

3.4.2. Linear Photophysical Measurements and Characterization

Linear photophysical parameters and photochemical stability of **9** and **13** were determined at room temperature in spectroscopic grade toluene (TOL), tetrahydrofuran (THF), and dichloromethane (DCM). The steady-state one-photon absorption (1PA) spectra were obtained with UV-Vis spectrophotometer Agilent 8453, using regular quartz cells with 1 cm path length and molecular concentrations, $C \approx (4\text{-}8)\cdot10^{-4}$ M. No aggregation effects were observed up to $C \approx 2\cdot10^{-2}$ M. The steady-state fluorescence, excitation, and excitation anisotropy spectra, along with the fluorescence lifetimes, τ_{fl}, were measured with FLS980 spectrofluorimeter (Edinburg Instruments Ltd.), using spectrofluorimetric quartz cells with 1 cm path length and low concentration solutions ($C \approx 2\cdot10^{-6}$ M). The excitation anisotropy spectra were obtained in viscous room temperature poly THF (pTHF) in order to avoid rotational depolarization effects.[79] Fluorescence quantum yields , Φ_{fl}, of **9** and **13** were determined by standard method[80] relative to Rhodamine 6G in ethanol ($\Phi_{fl} \approx 0.95$).[81] Photostability of these compounds was investigated under CW laser irradiation with excitation wavelength, $\lambda_{ex} \approx 532$ nm, and average irradiance 90 mW/cm^2. The values of photochemical decomposition quantum yields, Φ_{ph}, were determined in air saturated solutions using absorption methodology described in details previously.[79]

3.4.3. 2PA, Superfluorescence, Transient Absorption and STED Measurements

All nonlinear optical measurements were performed with femtosecond laser system described previously.[82,83] Femtosecond pulse train from Ti:Sapphire laser was regeneratively amplified by Legend Elite and pumped two optical parametric amplifiers, providing pulse duration, τ_P ≈ 100 fs (FWHM), 1 kHz repetition rate, pulse energy $E_P \leq$ 300 μJ, and tuning range 0.24 - 20 μ. The first OPA exit was used for direct measurements of the degenerate 2PA cross section values by open aperture Z-scan technique[84] using 1 mm path length quartz cells with molecular concentrations C ~ 10^{-2} M. Laser exit of the second OPA was used as a pump source for investigation of the superfluorescence properties of **9** and **13**. This laser beam was vertically polarized and focused by cylindrical lens into 4 mm × 10 mm × 35 mm fluorometric quartz cell to the waist of 0.15 mm × 4 mm, and transversely pumped liquid dye solutions (~10^{-2} - 10^{-3} M). Superfluorescence emission was observed perpendicular to the pumping beam and detected with fiber optic spectrometer. Femtosecond transient absorption measurements were performed with two laser beams from separate OPAs and optical delay line with retroreflector, using well developed pump-probe methodology.[82,85,86] Similar configuration of the experimental setup was used for STED cross sections measurements using fluorescence quenching method described previously in details.[83,87]

3.4.4. Linear Photophysical Properties and Photochemical Stability of 9 and 13

The steady-state one-photon absorption (1PA) spectra of DPPs (Figure 43a, b, curves 1-3) were nearly independent of solvent properties and exhibited well-defined vibrational structure with characteristic modes ≈ 1300 cm^{-1} (for **9**) and ≈ 1400 cm^{-1} (for **13**), evidence of noticeable vibronic interaction. The main photophysical parameters of **9** and **13** are presented in Table 5. As illustrated by these data, the values of maximum extinction coefficients were relatively small ~ (1-2)·10^4 $M^{-1}cm^{-1}$ and revealed extremely weak dependence on solvent polarity, $\Delta f = (\varepsilon - 1)/(2\varepsilon + 1) - (n^2 - 1)/(2n^2 + 1)$,[79] (where ε and n are the dielectric constant and refraction index of the medium, respectively). The excitation anisotropy spectra, $r(\lambda)$, of **9** and **13** (Figure 45c, d, curves 3) revealed the nature of the main long wavelength absorption contours. Constant values of $r(\lambda)$ in the spectral range 420 nm - 570 nm indicate on a dominant role of only one electronic transition $S_0 \rightarrow S_1$ in the main long wavelength absorption bands (S_0 and S_1 are the ground and first excited electronic states, respectively). In this case the values of transition dipoles, μ_{01}, for $S_0 \rightarrow S_1$ electronic transition can be calculated based on the experimental main 1PA bands as:[88]

$$\mu_{01} \approx 0.096 \cdot \sqrt{\int \varepsilon(\nu) \cdot d\nu / \nu^{max}} \qquad (1)$$

where μ_{01} is in D (see Table 5), extinction coefficient $\varepsilon(\nu)$ is in $M^{-1}cm^{-1}$, and ν is in cm^{-1} ($\nu^{max} = 1/\lambda_{ab}^{max}$). Small Stokes shifts and extremely weak solvatochromic behavior of **9** and

13 allow for the assumption of relatively small changes in the permanent dipole moments, $\Delta\mu_{01} = |\boldsymbol{\mu}_{00} - \boldsymbol{\mu}_{11}|$, under electronic excitation $S_0 \rightarrow S_1$ ($\boldsymbol{\mu}_{00}$ and $\boldsymbol{\mu}_{11}$ are the permanent dipole moments of S_0 and S_1 electronic states, correspondingly).

The steady-state fluorescence spectra of **9** and **13** (Figure 45a, b, curves 1'-3'), along with their excitation spectra (Figure 45c, d, curves 2) were independent of the excitation, λ_{ex}, and observed, λ_{obs}, wavelengths, respectively. These results were confirmed by 3D fluorescence maps shown in Figure 46a, b. It is also worth noting that excitation spectra of **9** and **13** overlapped well with corresponding absorption ones (Figure 45c, d, curves 1), which is indicative of reasonable agreement with Kasha's rule,[80] and negligible spectral dependence of the fluorescence quantum yields Φ_{fl}. Obtained values of Φ_{fl} were relatively high (0.7 - 0.8) and exhibited weak dependence on solvent polarity Δf. All spontaneous fluorescence emission processes in **9** and **13** exhibited mono-exponential decay profiles (Figure 46c, d, curves 1-3), and corresponding lifetimes, τ_{fl}, were in the range ~ 5 - 7 ns. The values of τ_{fl} were also estimated numerically from the equation $\tau_{fl}^{cal} = \tau_N \cdot \Phi_{fl}$ [79] and presented in Table 5 (natural lifetime, τ_N, was obtained from the Strickler and Berg approach[89] using experimental steady-state absorption and fluorescence spectra). As illustrated by these data, experimentally observed values of τ_{fl} noticeably deviate from the calculated ones, τ_{fl}^{cal}, and this deviation decreases with the increase in absorption efficiency in the main 1PA band. These results confirm the

limitations of the Strickler-Berg theory, which can be effectively employed for strongly allowed one-photon electronic transitions only.[89]

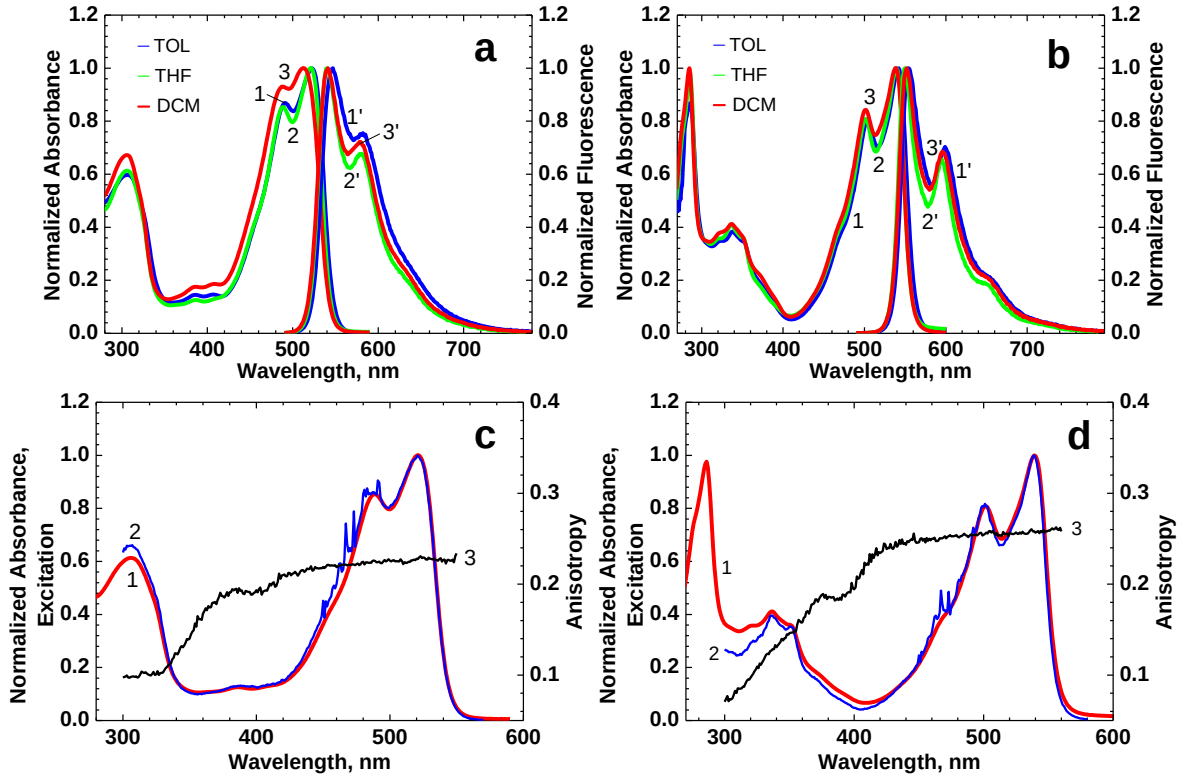

Figure 45. Normalized 1PA (1-3) and fluorescence (1′-3′) spectra of **9** (a) and **13** (b) in TOL (1, 1′), THF (2, 2′), and DCM (3, 3′). 1PA (1), excitation (2), and excitation anisotropy (3) spectra of 1 (c) and 2 (d) in THF (1, 2) and pTHF (3).

Photodecomposition quantum yields of **9** and **13**, Φ_{ph}, were determined in solvents of different polarity by absorption method[76] using CW laser excitation into the main 1PA band (λ_{ex} = 532 nm), and presented in Table 5. Observed changes in the optical density at λ_{ab}^{max} corresponded to the first order photoreaction under the employed irradiation conditions and all detectable photoproducts appeared in the short wavelength

range, at < λ_{ab}^{max}. Obtained values of $\Phi_{ph} \approx (2\text{-}5)\cdot10^{-4}$ were comparable with corresponding parameters of known fluorescent labels[82] and acceptable for practical applications in laser bioimaging.

Table 5. Linear photophysical and photochemical parameters of **9** and **13**.

DPP	**9**			**13**		
Solvent	TOL	THF	DCM	TOL	THF	DCM
Δf	0.0135	0.209	0.217	0.0135	0.209	0.217
λ_{ab}^{max}, nm	522 ± 1	521 ± 1	513 ± 1	541 ± 1	539 ± 1	538 ± 1
λ_{fl}^{max}, nm	546 ± 1	541 ± 1	541 ± 1	555 ± 1	550 ± 1	552 ± 1
Stokes shift, nm (cm^{-1})	24 ± 2 (≈ 840)	20 ± 2 (≈ 710)	28 ± 2 (≈ 1010)	14 ± 2 (≈ 470)	11 ± 2 (≈ 370)	14 ± 2 (≈ 470)
$\varepsilon^{max}\cdot10^{-3}$, $M^{-1}\cdot cm^{-1}$	9.6 ± 0.5	10.0 ± 0.5	8.8 ± 0.5	19.6 ± 1	20.2 ± 1	19.3 ± 1
μ_{01}*, D	3.8	3.9	3.8	5.2	5.3	5.3
Φ_{fl}, %	73 ± 5	77 ± 5	78 ± 5	67 ± 5	70 ± 5	73 ± 5
τ_{fl},** ns	7.0 ± 0.1	7.2 ± 0.1	7.7 ± 0.1	5.4 ± 0.1	5.9 ± 0.1	6.0 ± 0.1
τ_{fl}^{cal}, ns	20.4 ± 0.1	22.0 ± 0.1	22.2 ± 0.1	11.9 ± 0.1	12.6 ± 0.1	12.7 ± 0.1
$\Phi_{ph}\cdot10^{4}$	2.7 ± 0.5	4.6 ± 1	2.2 ± 0.5	2.8 ± 0.5	5.1 ± 1	3.5 ± 1

*See text for details. **Excitation wavelength, $\lambda_{ex} = \lambda_{ab}^{max}$. absorption λ_{ab}^{max} and fluorescence λ_{fl}^{max} maxima, Stokes shifts, maximum extinction coefficients ε^{max}, calculated transition dipole moments for $S_0 \rightarrow S_1$ excitation μ_{01}, fluorescence quantum yields Φ_{fl}, experimental τ_{fl}, and calculated τ_{fl}^{cal}, fluorescence lifetimes, and photodecomposition quantum yields Φ_{ph}.

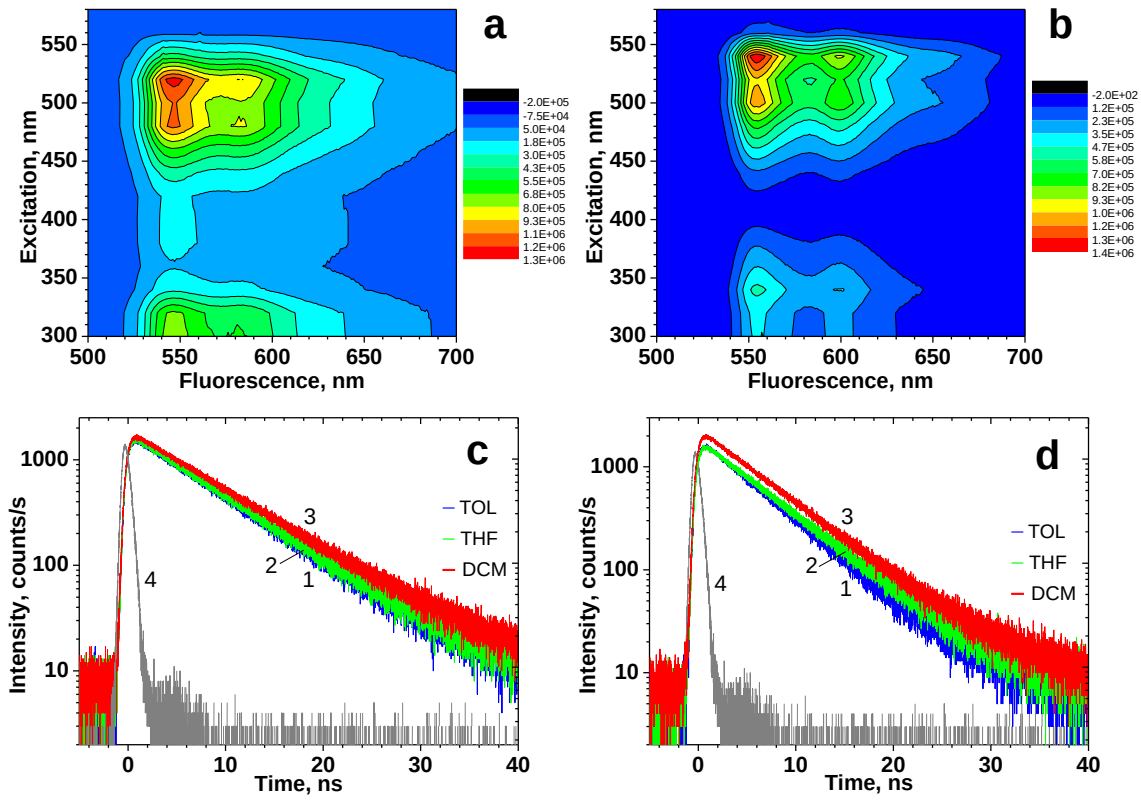

Figure 46. 3D fluorescence maps of **9** (a) and **13** (b) in TOL. Fluorescence decays of 1 (c) and 2 (d) in TOL (1), THF (2), DCM (3), and instrument response function (4).

3.4.5. 2PA Spectral Properties of 9 and 13

The investigation of two-photon absorption efficiency of **9** and **13** were performed in a broad spectral range by the well-developed open-aperture Z-scan method[75] and corresponding degenerate 2PA spectra are presented in Figure 47. Molecular structures of **9** and **13** are close to centrosymmetric compounds and, therefore, 2PA efficiency is relatively low in the main 1PA bands, with gradual increase in the two-photon allowed short wavelength region up to ~ 70-140 GM. 2PA cross sections, δ_{2PA}, in the one-photon allowed long wavelength absorption band are mainly determined by the product ~

$|\Delta\boldsymbol{\mu}_{01}|^2|\boldsymbol{\mu}_{01}|^2$, and obtained values of δ_{2PA} were consistent with the observed weak solvatochromic behavior of the steady-state fluorescence spectra of **9** and **13,** indicating on a small changes in the permanent dipole moment under electronic excitation $S_0 \rightarrow S_1$. Transition dipoles μ_{01} of **9** and **13** estimated from equation (1) (see Table 5) also confirm a good agreement with the obtained values of δ_{2PA}. The larger values of μ_{01} for **13** resulted in the corresponding increase in 2PA efficiency. It is worth noting that the maxima of two-photon action cross sections (i.e. the product of $\Phi_{fl} \cdot \delta_{2PA}$)[90] were in the range of ~ 50-100 GM, which is comparable with known two-photon fluorescence labels,[90-92] and can be practically employed.

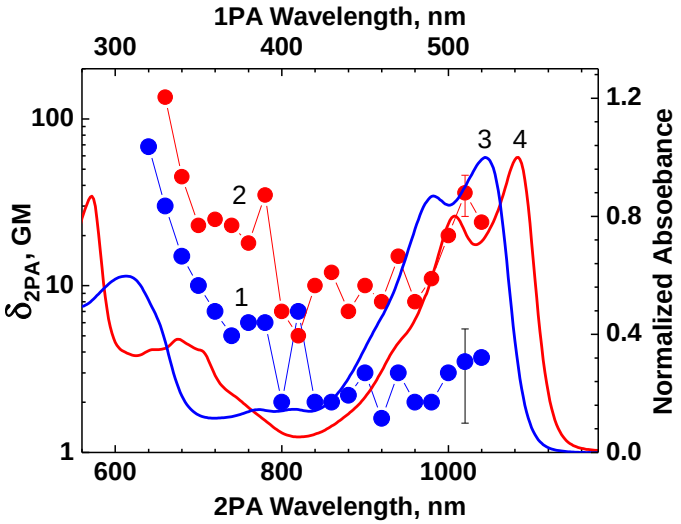

Figure 47. Degenerate 2PA (1, 2) and normalized 1PA (3, 4) spectra of **9** (1, 3) and **13** (2, 4) in TOL.

*3.4.6. Transient Absorption Spectroscopy and Superfluorescence Properties of **9** and **13***

The nature of fast relaxation processes in the excited state of **9** and **13** was investigated in low viscosity TOL solution using transient absorption pump-probe technique[82,86] with time resolution ≈ 300 fs. The kinetic dependences, $\Delta D = f(\tau_D)$, of the induced optical density, ΔD, on the time delay between pump and probe pulses, τ_D, were measured under excitation into the main long wavelength absorption band (pump wavelength, λ_{pm} = 500 nm), and probe wavelength, λ_{pr}, was tuned in a broad spectral range, 530-720 nm. The most representative dependences $\Delta D = f(\tau_D)$ for **9** and **13** are shown in Figures 48 and 49, respectively. In general, the values of induced optical density, ΔD, are determined by the depopulation of the ground state (saturable absorption (SA)), excited state absorption (ESA), and light amplification (gain) processes that usually occur in organic molecules under excitation.[93-95] As follows from these data, negative values of ΔD were detected in the main 1PA band (λ_{pr} = 530 nm), and corresponding maxima signals are related to the depopulation of the ground state S_0 accomplished in the first 300 - 400 fs (Figures 48a, 49a). The decrease in the absolute value of ΔD observed in the next 10-15 ps can be associated with the dynamic ESA and gain processes in the first excited electronic state S_1 due to Frank-Condon and solvent relaxation phenomena.[96-99] An efficient gain was observed for probe pulses in the fluorescence spectral range of **9** and **13** (Figures 48b-d, 49b-d), where no ground state absorption occurred, and negative values of ΔD can be attributed to the light

amplification with corresponding effects of solvent relaxation dynamics for particular λ_{pr}. Positive signals in the transient absorption kinetics were observed for $\lambda_{pr} \geq 660$ nm and 680 nm for **9** and **13**, respectively, and revealed a dominant role of the ESA processes in that spectral range (Figures 48e,f, 49e,f). Interestingly, some differences in the observed characteristic solvent relaxation times for different λ_{pr} can be explained by the specific spectral position of the particular λ_{pr} relative to the corresponding instantaneous ESA and/or stimulated emission contours.

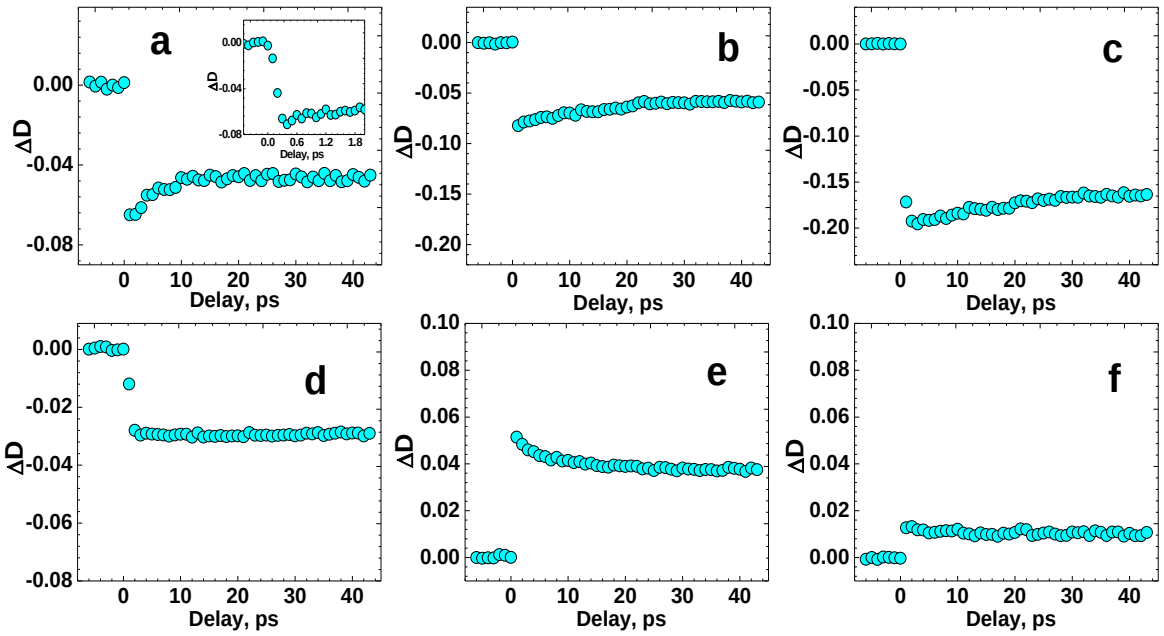

Figure 48. Kinetic dependences, $\Delta D = f(\tau_D)$, for **9** in TOL under pumping at λ_{pm} = 500 nm: λ_{pr} = 530 nm (a), 580 (b), 600 nm (c), 640 nm (d), 660 nm (e), and 700 nm (f).

Efficient light amplification of the weak probe pulses with λ_{pr} in the fluorescence spectral region (Figures 48b-d, 49b-d) was indicative of potential superfluorescence and lasing abilities of **9** and **13** in TOL, which was investigated at 10^{-2}-10^{-3} M under 1 kHz fs

transverse pumping into the main 1PA band. Highly reabsorbed and spectrally broad spontaneous fluorescence spectrum of **9** (Figure 50a, curve 1) was transformed into a narrow emission line (curves 2, 3) under the increase in pumping energy. The main parameters of the observed emission lines, such as linear polarization (in accordance with the polarization of the pump beam), relatively narrow spectral width (FWHM ~ 8-10 nm), high directionality (divergence ≤ 3 -5 mrad), along with the high intensity (more than ~ 3 orders of magnitude higher than spontaneous fluorescence emission), and obvious threshold character (Figure 50b) were attributed to the superfluorescence radiation.[78,82]

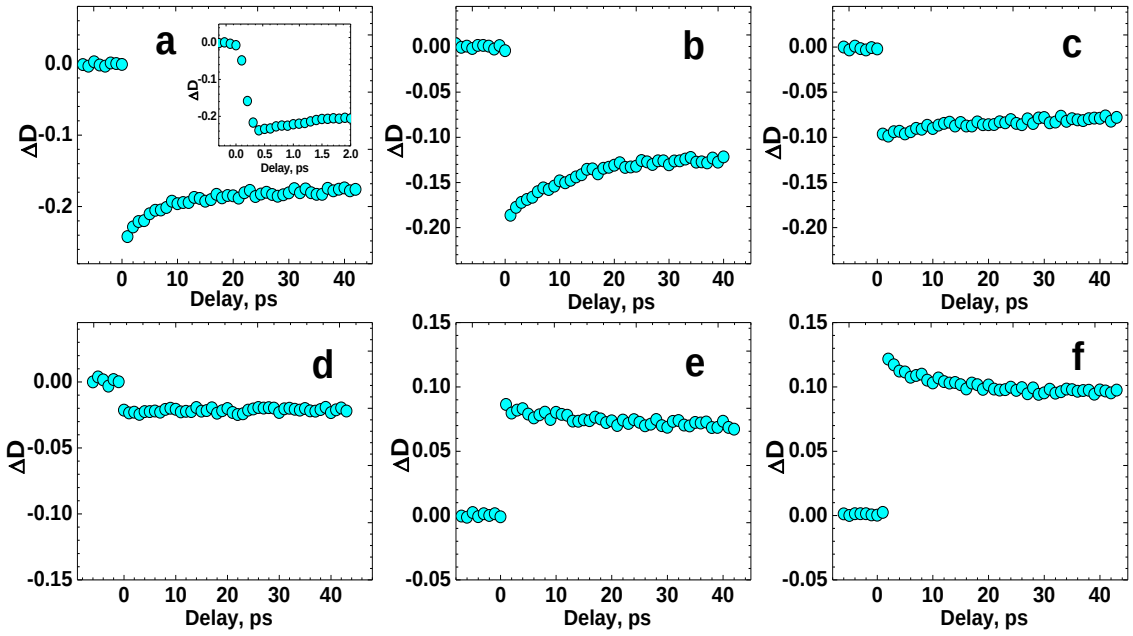

Figure 49. Kinetic dependences, $\Delta D = f(\tau_D)$, for **13** in TOL under pumping at λ_{pm} = 500 nm: λ_{pr} = 530 nm (a), 560 (b), 620 nm (c), 640 nm (d), 700 nm (e), and 720 nm (f). The insert in (a) is the initial part of $\Delta D = f(\tau_D)$ obtained from separate measurement with 100 fs temporal step in τ_D.

Compound **13** exhibited much less efficient supefluorescent properties than **9** despite comparable gain values observed in transient absorption measurements (see Figure 49b-d). Assumingly, it can be explained by smaller Stokes shift and much stronger self-reabsorption in highly concentrated solution. More significantly, superfluorescence phenomena have the potential to be used for dramatic increase in spectral brightness of the fluorescent probes and, therefore, are attractive for further development of the fluorescence microscopy technique.

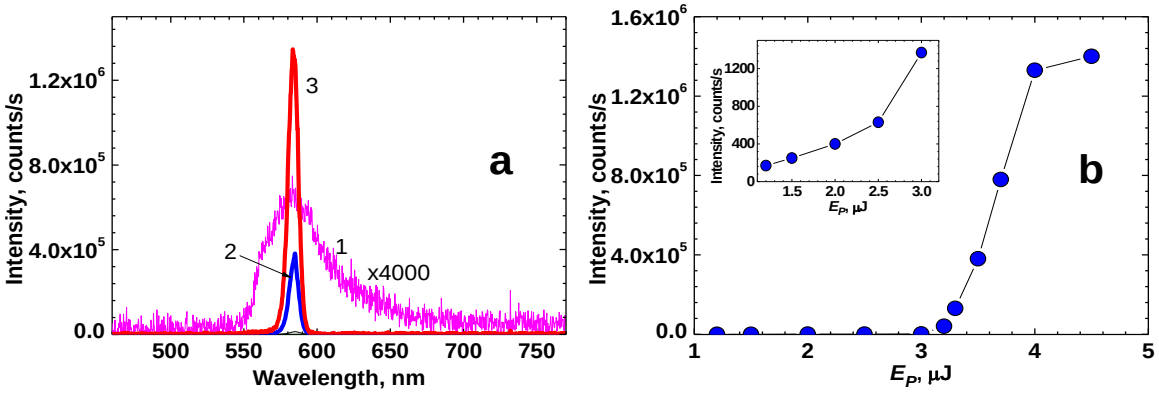

Figure 50. (a) Spontaneous fluorescence spectrum (1) and superfluorescence emission (2, 3) of **9** in TOL (C ~ $2.5 \cdot 10^{-3}$ M) under pump energy E_P = 1.2 μJ (1), 3.5 μJ (2), and 4 μJ (3) at λ_{pm} = 510 nm. (b) The threshold dependence of superfluorescence intensity on the pump energy. The insert in (b) shows the initial part of the threshold dependence.

3.4.7. STED Properties of 9 and 13

One-photon stimulated emission spectra of **9** and **13** were obtained by fluorescence quenching method comprehensively described previously.[83,87] Fluorescence emission was induced by femtosecond pump pulse with λ_{pm} = 500 nm, $E_P \approx$ 0.3 μJ, and τ_P = 100 fs, and then, after a small time delay, was partially quenched by another

(quenching) pulse with wavelength 580 nm ≤ λ_q ≤ 720 nm, energy 1 μJ ≤ E_q ≤ 25 μJ, and pulse duration τ_q = 100 fs. Time delay between pump and quench pulses was set to ≈ 30 ps in order to remove all effects related to the fast relaxation processes in S_1 state (see Figures 48, 49). The values of corresponding stimulated emission cross-sections $\sigma_{10}(\lambda_q)$ (i.e. cross-sections of $S_1 \rightarrow S_0$ optical stimulated transitions) were obtained from the fitting of the experimental dependences:

$$(1 - I_{fl} / I_{fl}^0) = \sigma_{10}(\lambda_q) \cdot \frac{\alpha \cdot E_q}{1 + \beta \cdot E_q} \qquad (2)$$

where $(1 - I_{fl} / I_{fl}^0)$ is the degree of fluorescence quenching (I_{fl} and I_{fl}^0 are the integral fluorescence intensities with and without quenching pulse, respectively); α and β are the parameters including pump and quench beam waists, λ_q, and ground state one-photon absorption cross-section at λ_q. It should be mentioned that equation (2) can be obtained based on the same approach,[87] taking into account additional ground state linear absorption processes and relatively weak multiphoton absorption efficiency at λ_q. In the case of negligible ground state absorption at λ_q ($\beta \cdot E_q << 1$) the values of $\sigma_{10}(\lambda_q)$ can be determined from the slope of the linear dependence:[83]

$$(1 - I_{fl} / I_{fl}^0) = \sigma_{10}(\lambda_q) \cdot \alpha \cdot E_q \qquad (3)$$

Typical experimental dependences $(1 - I_{fl} / I_{fl}^0) = f(E_q)$ and one-photon STED spectra of **9** and **13** are shown in Figure 51. The values of Stokes shifts of new compounds

are relatively small (see Table 5). For most of the employed quenching wavelengths λ_q, experimental dependences $(1-I_{fl}/I_{fl}^0)=f(E_q)$ deviated from the linear type due to ground state linear absorption (Figure 51b, e) and were subsequently fitted by equation (2). In the case of $\lambda_q >> \lambda_{ab}^{max}$, the degree of fluorescence quenching exhibited linear dependence on E_q (Figure 51a, d) which was fitted by equation (3). As follows from the obtained data, the absolute maxima values of $\sigma_{10} \approx 4\cdot10^{-17}$ cm^2 for **9** and $\approx 6\cdot10^{-17}$ cm^2 for **13** were comparable with the corresponding ground state absorption cross-sections maxima $\sigma_{01} \approx 3.7\cdot10^{-17}$ cm^2 and $\approx 7.4\cdot10^{-17}$ cm^2, respectively. The experimental values of $\sigma_{10}(\lambda_q)$ were analogous to calculated contours $\sigma_{10}^{cal}(\lambda) \sim \lambda^4 \cdot I_{fl}(\lambda)$,[98,99] (Figure 51c, d, curves 4), where $I_{fl}(\lambda)$ are the corresponding steady-state fluorescence spectra (curves 3). These results are in agreement with the observed "mirror symmetry" in the absorption-fluorescence spectra, small Stokes shifts, and weak solvatochromic dependences of the investigated diketopyrrolopyrrole derivatives. It should be emphasized that stimulated emission cross-sections of fluorescent probes are important parameters for high resolution STED microscopy technique, which need to be further developed for fundamental research and practical applications.

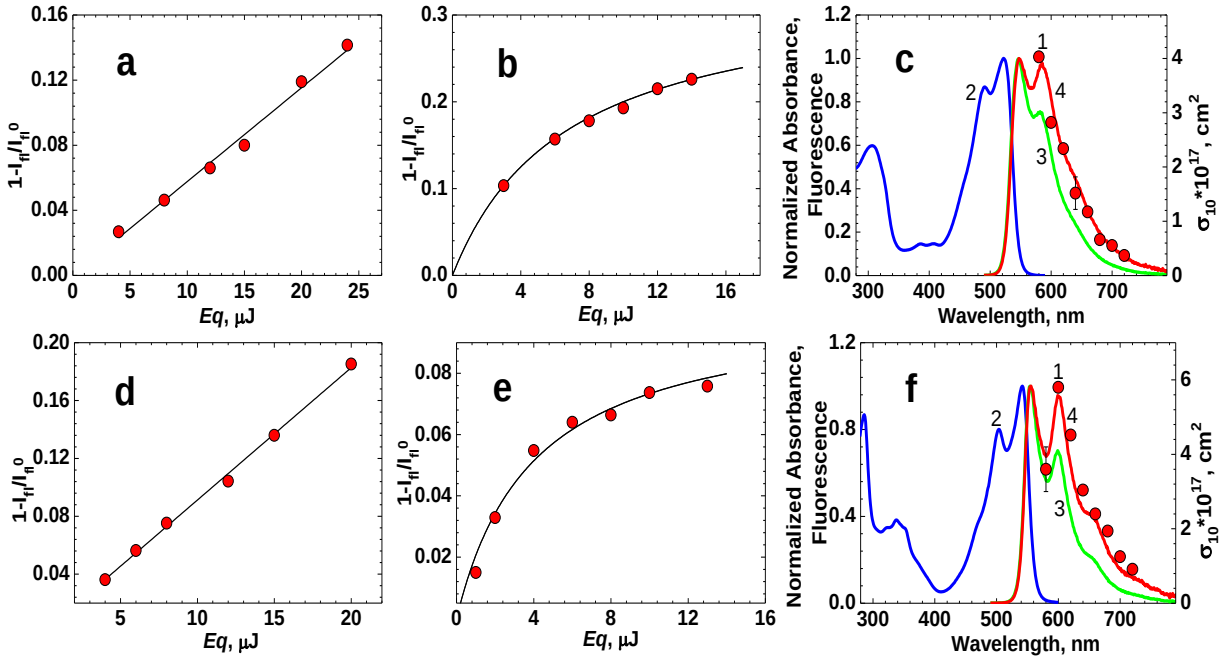

Figure 51. Experimental dependences $(1-I_{fl}/I_{fl}^{0}) = f(E_q)$ (a, b, d, e, red circles) and one-photon STED spectra (c, f, red circles) for **9** (a-c) and **13** (d-f) in TOL: λ_q = 580 (b, e) and 720 nm (a, d). The steady-state 1PA (c, f, curves 2), fluorescence (curves 3), and calculated stimulated emission (curves 4) spectra for **9** (c) and **13** (f) in TOL. Solid lines in (a, d) and (b, e) are the fitting curves obtained by equations (3) and (2), respectively.

3.5. Design and Synthesis of Water-Soluble Fluorescent DPP-based Chromophores

The results discussed above for DPP's **9** and **13** encouraged us to prepare hydrophilic DPP derivatives having extended π-conjugation that could result in higher 2PA efficiency. Enhanced two-photon DPP-fluorophores with large cross-sections would offer the ability for a highly confined excitation as well as intrinsic three-dimensional resolution in microscopic imaging, accompanied by an increased penetration depth in tissues as a by-product of a reduction of scattering losses.[100] The reduced photodamage, as well as improved signal-to-noise ratio may allow for bioimaging at deeper penetration

depth.[91] Toward that goal, 2-pyridyl substituted DPP **14**, having a short polyethylene glycol chains, was accessible through *N*-alkylation of the lactam moiety of **8** (Scheme 7).

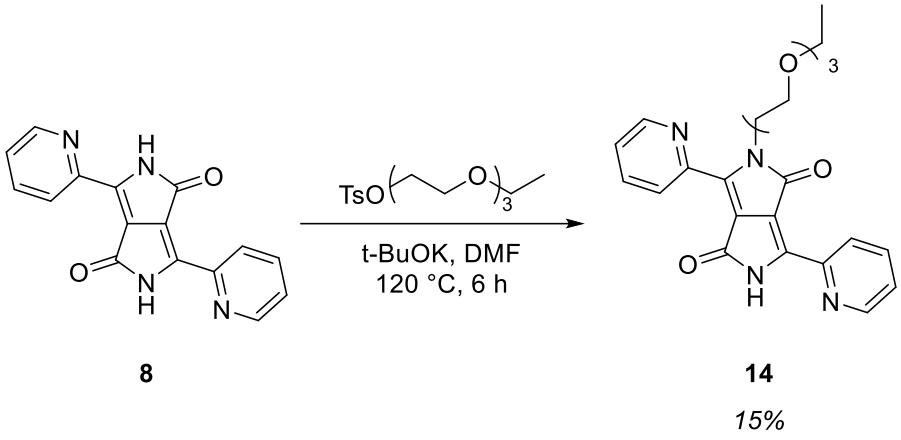

8 **14**

15%

Scheme 7. *N*-alkylation of 8 leads to 2-pyridyl substituted DPP **14**.

Examining the steady-state one-photon absorption (1PA) spectrum of **14** (Figure 52) shows a marked hypsochromic shift (λ_{ab}^{max} = 486 nm) compared to **9** in DCM (λ_{ab}^{max} = 513 nm) with little noticeable vibronic interaction (Figure 52). On the other side, the fluorescence quantum yield Φ_{fl} exhibited weak dependence on solvent polarity Δf with values close to the one obtained previously for **9** and **13** (~ 0.7). The satisfactory solubility and high fluorescence quantum yield of **14** in water prompt us to synthesize dopamine-conjugated DDP derivatives in order to investigate these chromophores as two-photon fluorescent tag suitable for cell imaging. In order to realize this goal, a hydrophobic DPP model compound was designed and prepared, and its linear photophysical properties have been assessed prior to preparing a hydrophilic analogue.

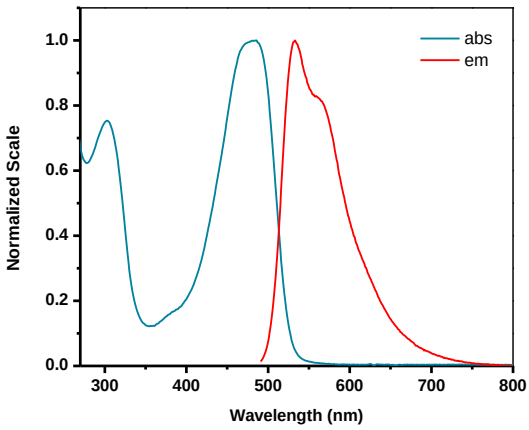

Figure 52. Normalized absorbance (λ_{max} = 486 nm, H_2O) and emission (λ_{em} = 533 nm, Φ_{fl} = 0.71) spectra of **14**.

3.5.1. Synthesis of Hydrophobic π-Extended DPP 18 and 21

The preparation of **18** followed a traditional synthetic route as depicted in Scheme 8. Alkylation of **11** was achieved by using K_2CO_3 in hot DMF, where the purification of the product was simplified by washing the crude solid obtained after the removal of DMF with methanol and hexanes. Borylation of **15** was achieved following a reported literature procedure with some optimization of the equivalence of LDA and boronic ester used to afford **16** in 65%. Finally, Suzuki cross-coupling between **16** and 5-bromo-2,3,3-trimethyl-3*H*-indole afforded **17**, which is prepared via a Fisher indole synthesis starting with 4-bromophenylhydrazine hydrochloride and 3-methylbutan-2-one in boiling ethanol/H_2SO_4 solution, afforded **18** in 40%. The efficiency of the last step was deterred by the deamination side products obtained (Scheme 8).

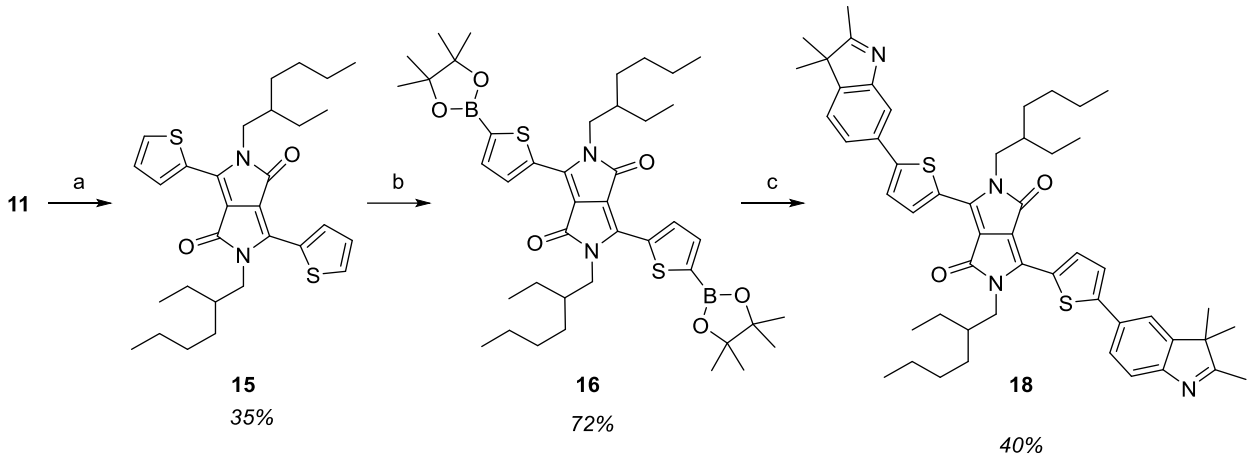

Scheme 8. (a) 2-Ethylhexyl bromide, K_2CO_3, DMF, 120 ˚C; (b) LDA, THF, 2-isopropoxy-4,4,5,5-tetramethyl-1,3,2-dioxaborolane; (c) **17**, $Pd(PPh_3)_4$, K_2CO_3, TOL, H_2O, 2 h, 120 ˚C.

Another hydrophobic DPP **21** with extended conjugation was prepared (Scheme 9). Thus, alkylation of **11** with *t*-butyl 2-bromoacetate afforded **19**, which was brominated at 5′-positions of thienyl moieties using NBS to give **20**. Intermediate **20** was successfully coupled to tributyl(thiophen-2-yl)stannane to provide **21** as dark blue powder.

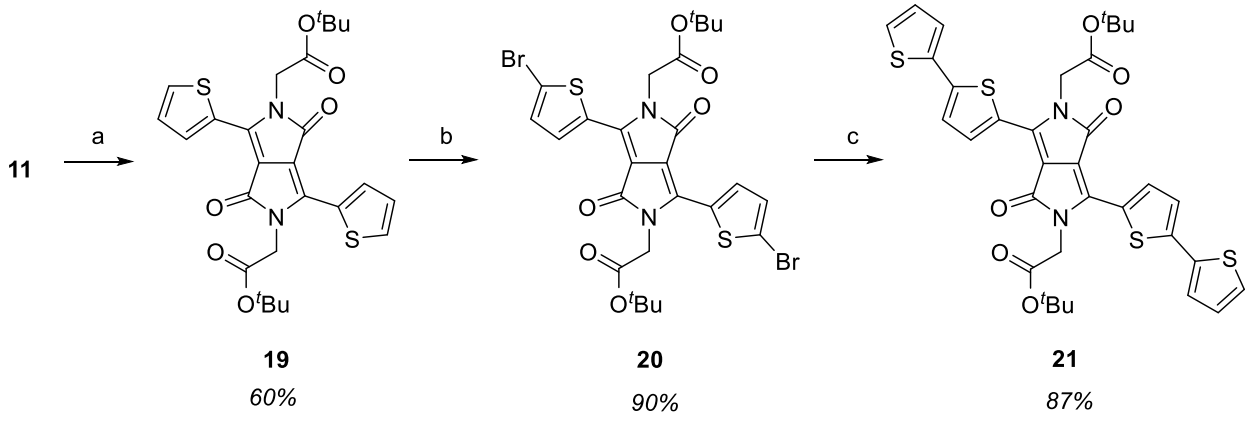

Scheme 9. Synthesis of 21. (a) *t*-butyl 2-bromoacetate, DMF, K_2CO_3, 12 h, 110 ˚C; (b) NBS, $CHCl_3$, dark, 12 h; (c) $Pd(PPh_3)_2$, tributyl(thiophen-2-yl)stannane, THF, 80 ˚C, 12 h.

3.5.2. Photophysical Characterization of 18 and 21

The steady-state OPA spectra of **18** (Figure 53a) were slightly unaffected by solvent polarity and exhibited well-defined vibrational structure as encountered previously (Table 6). The extinction coefficient determined in TOL is relatively larger than that determined for DPPs 9 and 13, with a value of $\varepsilon^{max} = 5.0 \pm 0.5 \times 10^4$ M^1 cm^1.

The steady-state fluorescence spectra of **18** (Figure 53b) were independent of the excitation wavelengths, with emission in the NIR and relatively large Stokes shifts. In contrast to values obtained for DPP's **9** and **13**, obtained values of ϕ_{fl} are significantly dependent on solvent polarity with $\phi_{fl} = 0.28$ in the case of MeOH ($\Delta f = 0.3098$).

This suggested that a hydrophilic derivative of **18** may exhibit a lower quantum yield in water, yet can be significantly fluorescent for bioimaging purposes. A similar suggestion was drawn upon examining the absorption and emission profiles of **21** in TOL which exhibited a $\Phi_{fl} = 0.55$ that is comparable to that obtained for **18** in TOL.

Table 6. Linear photophysical parameters of 18 in solvents with different polarity Δf **.**

Solvent	**Toluene**	**DCM**	**MeOH**
λ_{ab}^{max} (nm)	615 ± 1	611 ± 1	597 ± 1
λ_{fl}^{max} (nm)	704 ± 1	699 ± 1	690 ± 1
Stokes Shift (nm)	89 ± 2	88 ± 2	93 ± 2
Φ_{fl} (CV, MeOH)	0.62	0.56	0.28

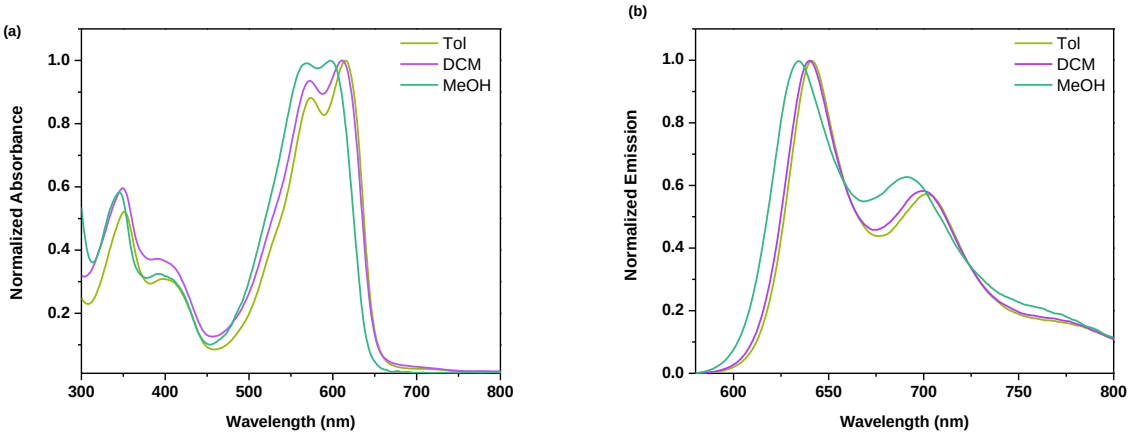

Figure 53. (a) Absorption and (b) emission spectra of **18** in solvents of varying polarity**.**

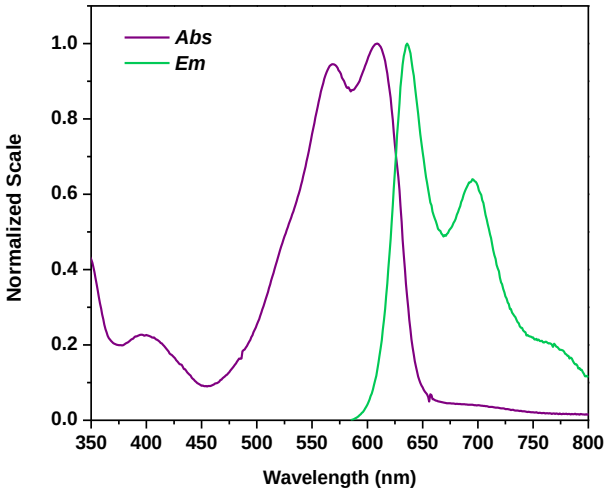

Figure 54. Absorbance and fluorescence spectra of **21** in TOL.

The investigation of 2PA efficiency of **18** was performed over a broad spectral range by the well-developed open-aperture Z-scan method and corresponding degenerate 2PA spectrum are presented in Figure 55. Given the entrosymmetric nature of **18** structure, the 2PA efficiency is relatively low in the main 1PA bands, with a gradual increase in the two-photon allowed short wavelength region up to ~ 210 GM.

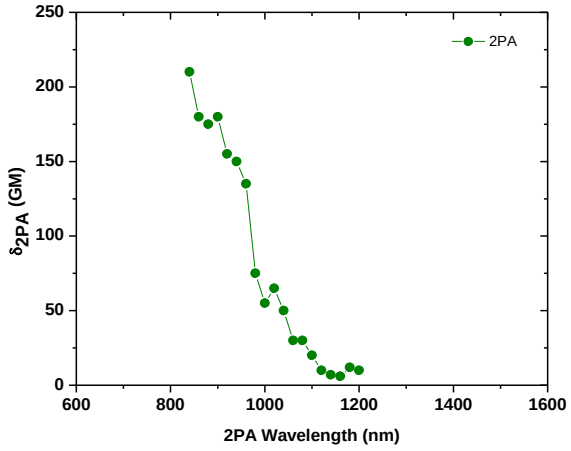

Figure 55. Degenerate 2PA of **18** in TOL.

3.5.3. Synthesis of Hydrophilic π-Extended DPP 24 and 25

The synthesis of hydrophilic derivative of DPP **25** followed a similar synthetic route to that of **18**. Starting with t-butyl ester intermediate **19**, borylation as described previously afforded **22** in poor yields (~ 20%), which was used for coupling to **17** under modified Suzuki conditions, where KF was used instead of K2CO3 to hydrolyze the boronic ester **22**. The resulting intermediate **23** was dissolved in TFA, which was employed for the hydrolysis of t-butyl ester group to furnish **24** as green flakes. The solubility of 24 in NaOH solution is excellent, but shows low solubility in buffer of pH < 7.4. As for **21**, the same hydrolysis conditions resulted in the bis-carboxylic acid **25**, which shows similar solubility characteristics to **24** (Scheme 10).

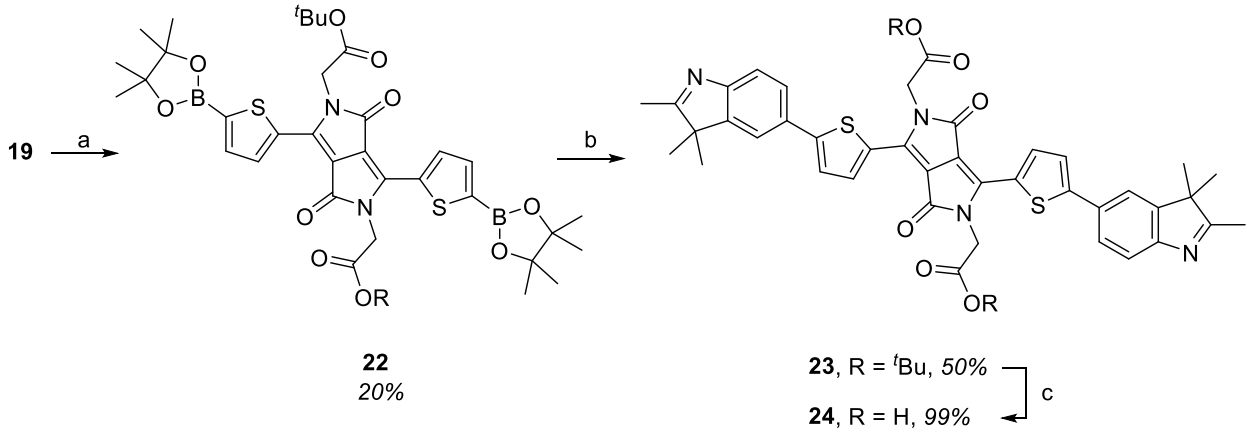

Scheme 10. (a) LDA, THF, 2-isopropoxy-4,4,5,5-tetramethyl-1,3,2-dioxaborolane; (b) **17**, $Pd(PPh_3)_4$, K_2CO_3, TOL, H_2O, 2 h, 120 ˚C, (c) TFA, DCM, 8 h, rt.

*3.5.4. Photophysical Characterization of **24** and **25***

When compared to their hydrophobic analogues **18** and **21**, respectively, the electronic absorption spectra of phosphate-buffered saline (PBS, pH 7.3, simulated physiological conditions) of DPPs **24** and **25** are dominated by a broad and intense band centered around λ = 575 nm for either DPP dyes, and showed no indication of noticeable vibronic interaction in their corresponding absorption spectra. The emission bands corresponding to DPPs **24** (618 and 669 nm) and **25** (640 and 692 nm) in PBS are similar to previously studied analogues, but show a hypsochromic shift in the emission spectrum of **24** as compared to that of **18** (Figure 56). Remarkably, the emission band corresponding o the bithiophene DPP analogue **25** closely resembles that observed for the hydrophobic analogue in MeOH (Figure 57)**.** More notably, the quantum yield of **24** and **25** in PBS was significantly low, with values of 0.01 and 0.02, respectively, suggesting an increased hydrogen-bonding interaction from MeOH to water in the case of indole-terminated DPP

18 and **24** that may contribute to fluorescence-quenching perhaps by composing electron accepting water cages as reported for heterocyclic amines.[101]

In line with the aforementioned observations, bovine serum albumin (BSA) was used in order to determine whether a significant turn-on of fluorescence can be observed. Serum albumin is a plasma protein that is well-known known for its ability to bind and to transport various ligands to specific sites.[102,103] Encapsulation of the DPP dyes with BSA is driven by hydrophobic interactions as well as hydrogen bonding as a result of the anchoring carboxylate moieties of DPPs. Such interactions may lead to enhanced rigidity, which may result in fluorescence turn-on and increased fluorescence life time, as well as shield the DPP against quenchers such as ions and thiols, hence providing enhanced stability to the fluorophores under investigation. Undeniably, fluorescence intensity was strongly enhanced upon addition of BSA, especially in the case of **24**, where quantum yield has increased around two folds (Figure 58). While further studies are underway to determine the binding affinity of these dyes to BSA, fluorescence turn-on was also achieved in a solution containing sodium dodecyl sulfate (SDS), an ionic surfactant, with a one-fold enhancement compared to solution with no additives (Figure 58a). Such observations suggest that cell imaging using these dyes is promising as BSA and SDS mimic the hydrophobic nature of cellular components.

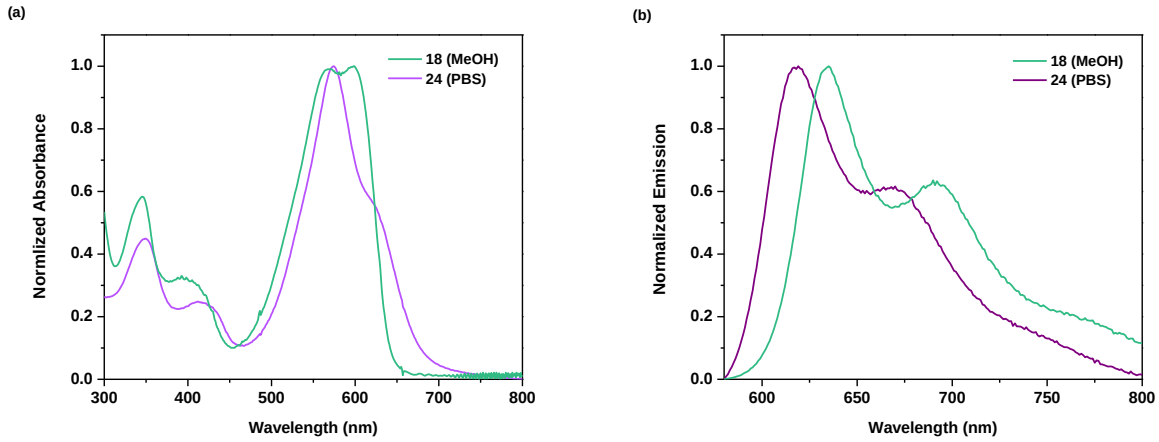

Figure 56. (a) Normalized absorption and (b) emission spectra of **18** and **24**.

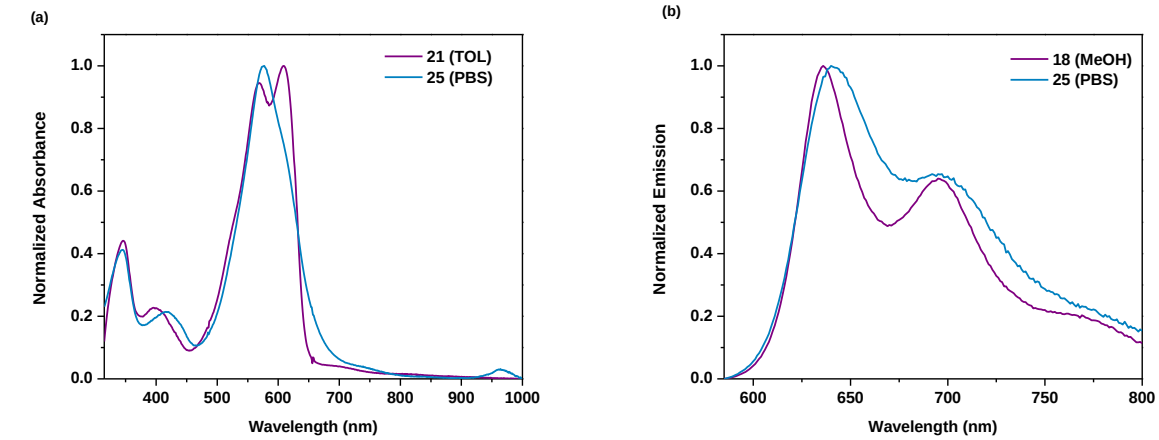

Figure 57. (a) Normalized absorption and (b) emission spectra of **21** and **25**.

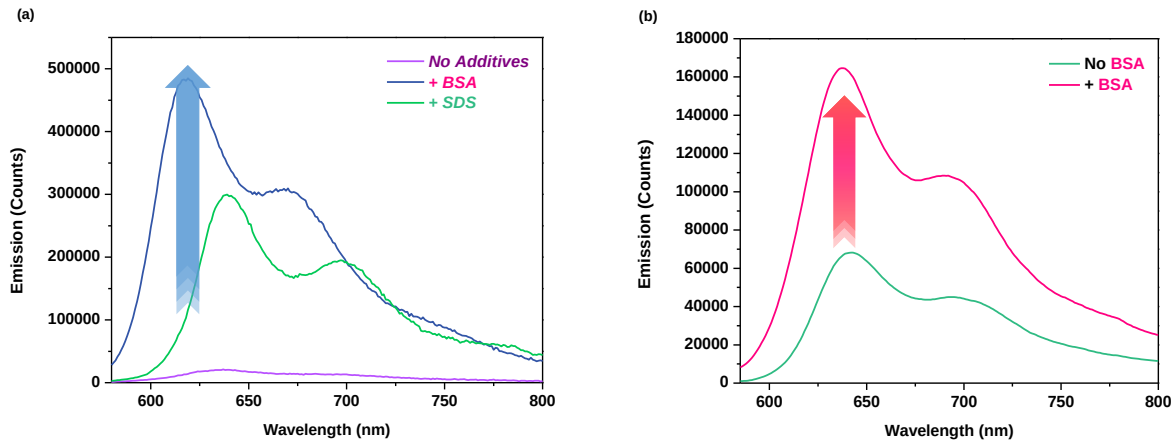

Figure 58. Effect of additives on the emission spectra of (a) **24** and (b) **25** in PBS.

3.6. Investigating DPPs as Fluorescent Dyes for Bioimaging

The efficacy of the prepared DPPs as fluorescent dyes was assessed by preliminary fluorescence imaging experiments. In that regard, hydrophobic DPP **20** was determined to be suitable for encapsulation in Pluronic® F-127, an FDA approved poloxomer micelle that has been used in drug delivery applications to enhance the solubility of hydrophobic drugs.[104-106] Micelle-encapsulated DPP **20** was coincubated with Lysotracker™ Green to determine whether the micelle-encapsulated dye will be localized in the lysosomes as anticipated. Interestingly, fluorescence imaging of the micelle-encapsulated **20** in HCT116 cells demonstrates good cellular uptake. (Figure 59b). Overlap image with LysoTracker Green shows good colocolaization, indicating that most micelles are distributed in the cellular lysosomes (Figure 59c).

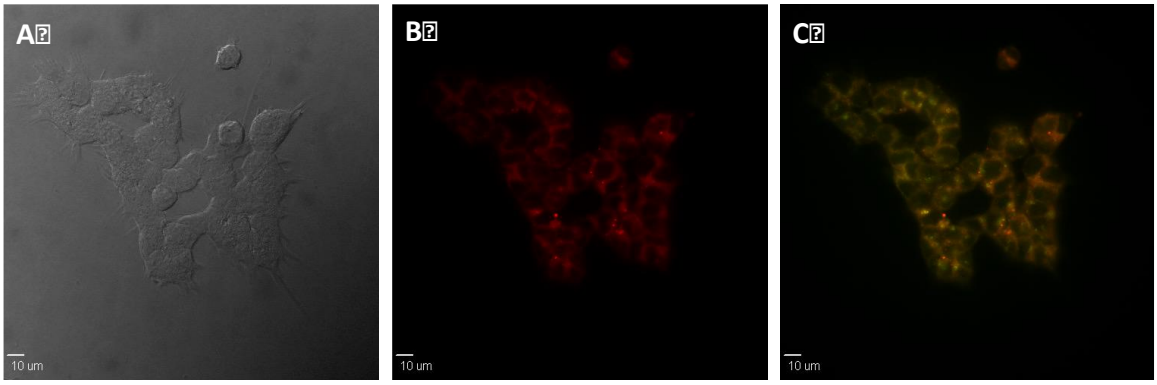

Figure 59. Confocal fluorescence images of HCT 116 cells incubated with **20** micelles (10 μM, 2 h) and LysoTracker Green (75 nM, 2 h). (a) DIC, (b) fluorescence image with **20** micelles, (c) colocalization imaging, overlay of b and LysoTacker Green. FitC filter cube (Ex: 477/50, DM: 507, Em: 536/40) and Texas Red filter cube (Ex: 562/40, DM: 593, Em: 624/40) were applied to excite LysoTracker Green and **20**.

The good solubility of DPP **25** in PBS allowed for the direct use of the dye in buffer solution for cell incubation. Initially, biocompatibility of **25** was examined by employing a cell viability experiment using HCT-116 colon carcinoma cells. Solutions of varying concentrations of **25** (1.5 to 100 μM) were used for dye incubation with the prepared cells and the viability was measured by MTS assay.[107] After 20 h incubation with cells the percentage of viable cells remained above 80%, indicating fairly low overall toxicity of DPP **25** even at 100 μM (Figure 60).

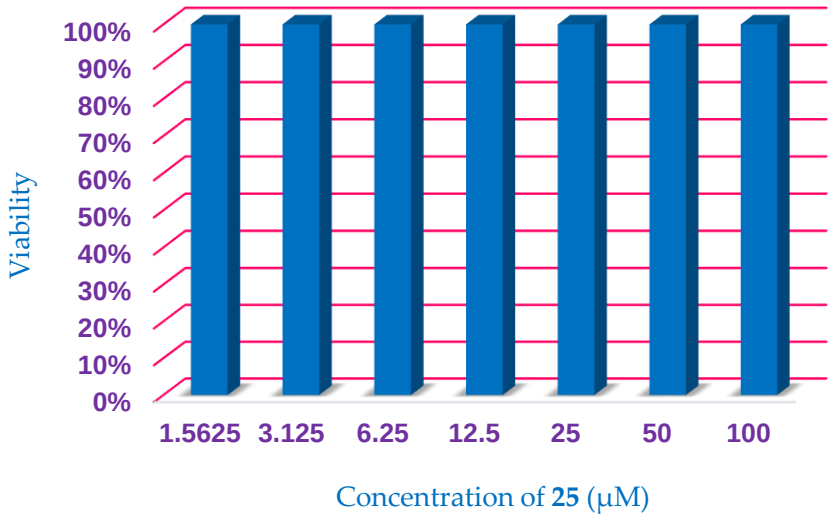

Figure 60. Viability Chart of **25** in HCT-116 cells.

Based on these results, two concentrations (25 and 50 μM) of **25** in PBS were chosen for incubation and imaging, with greater signal-to-noise images obtained at 50 μM. 1PE of the fixed cells (Figure 61a-c) indicates successful permeation of the cell membrane, where strong fluorescence signal can be seen throughout the cytoplasm of the cells, with little specificity of the dye towards organelle. 2PE images also have good signal but show

a greater signal-to-noise ratio when compared to the 1PE images, further supporting the internalization of **25** into the cytoplasm.

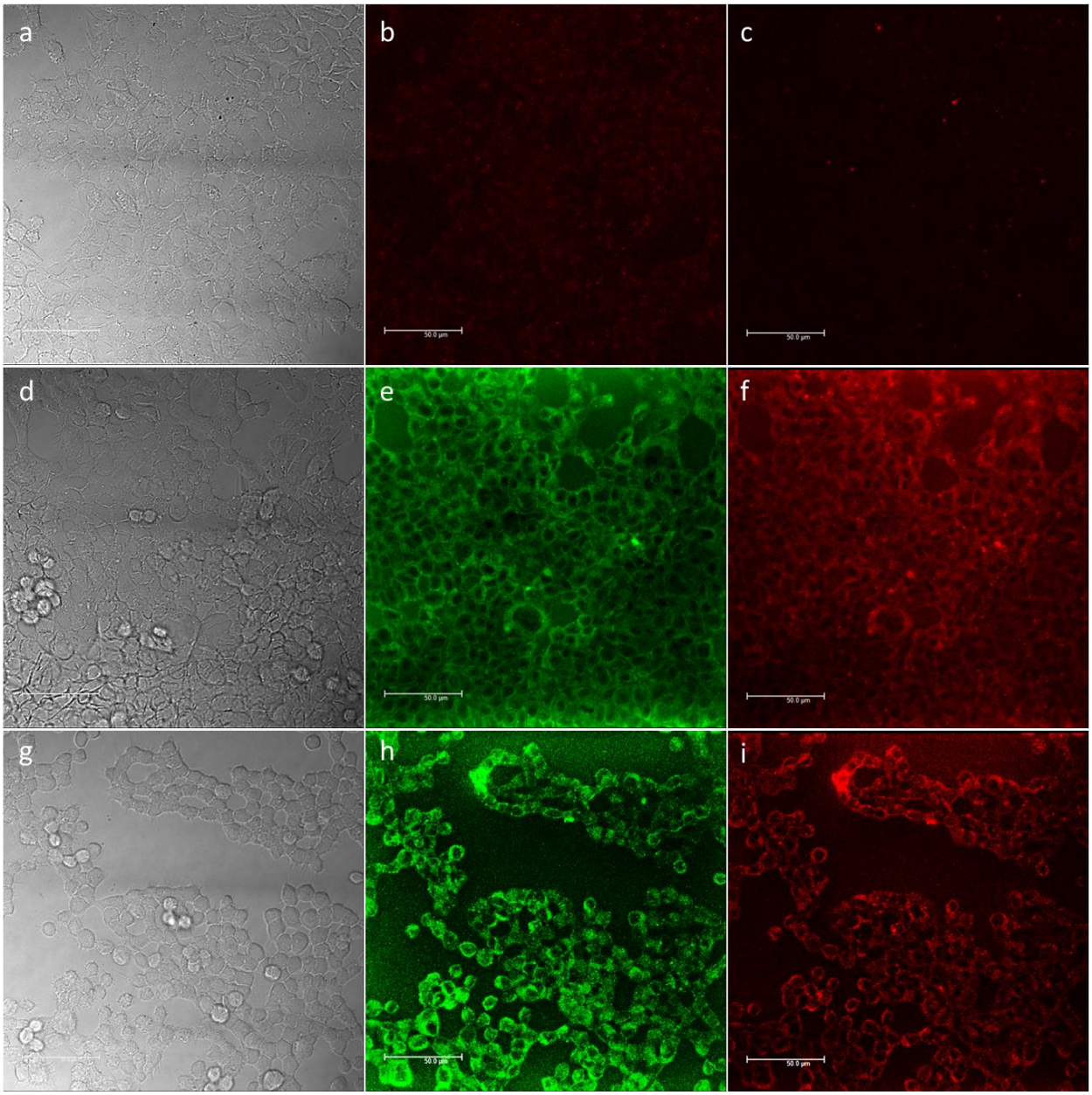

Figure 61. Confocal fluorescence images of HCT 116 cells (control, a-c) incubated with **25** (25 μM, d-f and 50 μM, g-i). (a), (d) and (g) are DIC, (b), (e), and (h) are 1PE (λ_{ex} = 562 nm), 2PE (λ = 810 nm) of HCT 116 cells with no dye, incubated with 25 μM and 50 μM of **25**, respectively.

Fluorescence enhancement through non-covalent binding to BSA, coupled with the presence of a free carboxylic acid group on their core structure, render the prepared DPP **25** as potential candidates for *in vivo* imaging. Furthermore, ongoing efforts entail 1PFM and 2PFM imaging of cells incubated with DPP **24**.

3.7. Conclusions

Derivatives **9** and **13** of the well-known DPP-type organic pigments were synthesized and comprehensively investigated. A variety of linear photophysical, photochemical and nonlinear optical properties of **9** and **13** were shown in a number of organic solvents at room temperature. The steady-state absorption, fluorescence, and excitation anisotropy spectra revealed the nature of the main absorption bands, weak solvatochromic behavior, strong vibronic coupling, and agreement with Kasha's rule. 2PA spectra of **9** and **13** were obtained in a broad spectral range by open aperture Z-scan method and two-photon action cross sections of 50-100 GM were shown. Fast dynamic ESA and gain processes with characteristic times of 10-15 ps were observed for **1** and **2** in a broad spectral range, and efficient superfluorescence emission was shown for **1** in TOL under femtosecond transverse pumping. The values of one-photon STED cross-sections were determined for **9** and **13** by fluorescence quenching pump-probe technique and maxima values of σ_{10}, obtained experimentally, were close to corresponding ground state absorption cross-sections maxima σ_{01}. It is worth mentioning that such interesting linear spectral and nonlinear optical properties of these DPP derivatives make such

derivatives attractive for various practical applications, including two-photon induced fluorescence and STED microscopy techniques.

Water-soluble DPPs exhibits remarkable features including good solubility in aqueous media; the interesting optical properties, and the availability of a free carboxylic acid group on their core structure, and low cytotoxicity render these derivatives suitable candidate for bioimaging applications. Currently, focus to conjugate the studied dyes to targeting peptides is underway.

3.8. Experimental Section

3.8.1. Solutions and Methods for Cell Imaging

Pluronic Micelles of 20. A solution of DPP **20** in DCM (0.5 mM) was mixed with an equal volume of Pluronic-127 solution in PBS (2.5 mg/mL). The mixture were stirred at 60 °C overnight to remove DCM, and the resulting micelle solution was stored at 4 °C for cell incubation.

Cell Incubation for 20 Imaging. HCT-116 colon carcinoma cells (America Type Culture Collection, Manassas, VA) were seeded on poly-D-lysine functionalized coverslip in a 24-well plate. Cells were incubated in RPMI-1640 complete medium (Life Technologies) for 48 h, followed by incubation with **20** micelle (10 μM) and LysoTracker Green (Life Technologies, 100 nM) mixture or **25** (25 or 50 μM) for 45 min. Cells were then fixed with formaldehyde solution (4%) and treated with $NaBH_4$ (1 mg/mL) with 2x

washes of phosphate buffered saline (PBS) between each step. Coverslips were again washed and mounted on slides with ProLong Gold antifade reagent (Life Technologies). Images were taken with Olympus IX70 DSU microscope.

Cytotoxcity Assay. HCT 116 cells (America Type Culture Collection, Manassas, VA) were placed in 96 well plates and incubated until there were no fewer than 6×10^3 cells per well for the cytotoxicity assays. After that, the cells were incubated at different concentrations of **25** for an additional 20 h. Next, 20 μL of CellTiter 96 Aqueous One solution reagent was added into each well and incubated for an additional 4 h. The relative cell viability, incubated with **25** and a control for untreated cells, was determined by measuring the MTS formazan absorbance on a microplate reader at 490 nm. All absorbance values were subtracted from the blank volume from a cell-free control.

Cell Imaging: Images of cells incubated with **25** were taken with a Leica TCS SP5 II laser-scanning confocal microscope system with a 63x objective (HCX Pl APO CS 63.0 x 1.20 WATER UV), while those incubated with **20** micelles were take were taken with Olympus IX70 DSU microscope. One photon images of cells incubated with **25** were taken with 561 nm excitation wavelength and emission collected between 600 to 700 nm. Two-photon fluorescence images were recorded using a tunable Coherent Chameleion Vision S (80MHz, mode-locked, 75 fs pulse width, tuned to 810nm) which is coupled to the Leica system.

3.8.2. Synthesis of DPPs

3,6-Di(pyridin-2-yl)-2,5-dihydropyrrolo[3,4-*c*]pyrrole-1,4-dione (8). A solution of *t*-BuOK (2.70 g, 24.0 mmol) in *t*-amyl alcohol (50 mL) is heated at 110 ˚C for 1 hr under N_2. 2-Cyanopyridine (10.40 g, 20.0 mmol) and a catalytic amount of 18-crown-6 ether (100 mg) are added to the solution, which becomes dark brown. To this mixture, a solution of diethyl succinate (1.66 mL, 10.0 mmol) in *t*-amyl alcohol (10 mL) is added dropwise over a period of 20 min. The purple mixture is heated at 110 ˚C for additional 3 hr before cooling to 50 ˚C, when a solution of MeOH:H_2O (30 mL:10 mL) is carefully added to the reaction mixture. The resulting sluggish deep red solution is heated for 20 min under reflux and then cooled at room temperature, and poured onto dilute HCl (1 N, 50 mL) and ice (100 g). The mixture is stirred vigorously for 30 min and the precipitate was collected by filtration. The solid is dissolved in hot MeOH (100 mL) and heated for 10 min, and then precipitate is collected and dried to afford the title compound as red powder (4.65 g, 16.2 mmol, 81%).

2-(2-Ethylhexyl)-3,6-di(pyridin-2-yl)-2,5-dihydropyrrolo[3,4-*c*]pyrrole-1,4-dione (9). 2-Ethylhexylbromide (2.90 g, 15.0 mmol) was added to a suspension of **8** (2.90 g, 15.0 mmol), t-BuOK (1.70 g, 15.0 mmol) and catalytic amount of 18-crown-6 ether in DMF (25 mL). The suspension was stirred overnight at room temperature and then poured onto ice (150 g). After vigorous stirring, the insoluble materials were collected and dried. Purification was achieved using column chromatography (Hexanes: EtOAc, 3:1) and

washing with cold hexanes to afford the title product as dark red powder (2.60 g, 6.5 mmol, 65%). ^{1}H NMR (400 MHz, Chloroform-*d*) δ 9.01 (dt, *J* = 7.9, 1.0 Hz, 1H), 8.77 (dt, *J* = 8.0, 1.0 Hz, 1H), 8.70 (br s, 1H), 8.64 (ddd, *J* = 4.8, 1.8, 0.9 Hz, 1H), 8.59 (ddd, *J* = 4.8, 1.7, 0.9 Hz, 1H), 7.84 (dddd, *J* = 7.6, 4.6, 1.8 Hz, 2H), 7.31 (dddd, *J* = 9.1, 7.6, 4.8, 1.1 Hz, 2H), 4.29 (t, *J* = 7.5 Hz, 2H), 1.54 – 1.42 (m, 1H), 1.26 – 1.16 (m, 8H), 0.79 – 0.71 (m, 6H). ESI-HRMS calcd. For $C_{24}H_{26}N_4O_2$ $[M+H]^+$ 403.5055; found 403.4045.

2-(10-Azidodecyl)-3,6-di(thiophen-2-yl)-2,5-dihydropyrrolo[3,4-*c*]pyrrole-1,4-dione (13). A solution of 2-(10-bromodecyl)-3,6-di(thiophen-2-yl)-2,5-dihydropyrrolo[3,4-*c*]pyrrole-1,4-dione **12** (0.52 g, 1.0 mmol) prepared as described for the synthesis of **8**, and NaN_3 (0.12 g, 2.0 mmol) in anhyd. DMF (5 mL) was heated under Ar at 80 °C for 8 h. The solution was cooled to room temperature and then poured over ice water (100 mL). The product was collected by filtration, suspended in DCM, and dried over Na2SO4. The solvent was evaporated under reduced pressure to afford the title compound as brick red flakes (0.48 g, 99%). ^{1}H NMR (400 MHz, DMSO-d_6) δ 11.38 (s, 1H), 8.76 (dd, *J* = 3.9, 1.2 Hz, 1H), 8.26 (dd, *J* = 3.8, 1.2 Hz, 1H), 8.05 (dd, *J* = 5.0, 1.2 Hz, 1H), 8.01 (dd, *J* = 5.0, 1.1 Hz, 1H), 7.39 (dd, *J* = 5.0, 3.9 Hz, 1H), 7.32 (dd, *J* = 5.0, 3.8 Hz, 1H), 4.02 – 3.93 (m, 2H), 3.29 (t, *J* = 6.9 Hz, 2H), 1.61 (d, *J* = 7.5 Hz, 2H), 1.55 – 1.43 (m, 2H), 1.27 (m, *J* = 27.1 Hz, 12H).^{13}C NMR (101 MHz,) δ 160.9, 135.0, 134.1, 133.0, 132.5, 130.1, 129.6, 129.4, 107.7, 51.4, 42.0, 40.8, 40.2, 30.1, 29.5, 29.2, 29.0, 26.9. ESI-HRMS calcd. For $C_{24}H_{26}N_4O_2$ $[M+H]^+$ 482.1679; found 482.1670.

2,5-Bis(2-ethylhexyl)-3,6-bis(5-(2,3,3-trimethyl-3*H*-indol-5-yl)thiophen-2-yl)-2,5-dihydropyrrolo[3,4-*c*]pyrrole-1,4-dione (18). Prepared according literature.[108] ^{1}H NMR (400 MHz, $CDCl_3$) δ 8.97 (d, J = 4.1 Hz, 2H), 7.66 (dd, J = 8.0, 1.8 Hz, 2H), 7.61 – 7.56 (m, 4H), 7.47 (d, J = 4.1 Hz, 2H), 4.20 – 4.03 (m, 4H), 2.33 (s, 6H), 1.97 (s, 2H), 1.48 – 1.25 (m, 28H), 0.98 – 0.84 (m, 12H). ^{13}C NMR (100 MHz, $CDCl_3$) δ 189.7, 162.1, 154.9, 150.5, 147.2, 140.1, 137.1, 130.7, 128.9, 126.5, 124.6, 120.8, 119.5, 108.5, 77.6, 54.3, 46.4, 39.6, 30.8, 29.0, 24.1, 23.5, 15.9, 14.4, 11.0. ESI-HRMS calcd. For $C_{52}H_{62}N_4O_2S_2$ $[M+H]^+$ 839.4314; found 839.4353.

Di-tert-butyl 2,2'-(3,6-di([2,2'-bithiophen]-5-yl)-1,4-dioxopyrrolo[3,4-*c*]pyrrole-2,5(1*H*,4*H*)-diyl)diacetate (21). Prepared according to literature procedure.[108] ^{1}H NMR (400 MHz, Chloroform-*d*) δ 8.76 (d, J = 4.1 Hz, 1H), 7.37 – 7.27 (m, 3H), 7.07 (dd, J = 5.1, 3.7 Hz, 1H), 4.82 (s, 2H), 1.47 (s, 9H). ^{13}C NMR (101 MHz, $CDCl_3$) δ 167.5, 161.3, 143.3, 139.4, 136.6, 136.4, 128.7, 128.4, 126.7, 125.6, 125.4, 108.3, 100.3, 83.3, 44.6, 28.4.

2,2'-(1,4-Dioxo-3,6-bis(5-(2,3,3-trimethyl-3*H*-indol-5-yl)thiophen-2-yl)pyrrolo[3,4-c]pyrrole-2,5(1*H*,4*H*)-diyl)diacetic acid (24). TFA (2.00 mL) was added to a solution of DPP **23** (0.42 g, 0.5 mmol) in DCM at 0 ˚C. The solution was stirred overnight, and the solvent was evaporated under reduced pressure. Toluene (20 mL) was then added and the solvent was evaporated again to remove any excess TFA, to afford the title compound as green crystals (0.31 g, 0.5 mmol, 99%). ^{1}H NMR (400 MHz, $CDCl_3$) δ 8.88 (d, J = 4.2 Hz, 1H), 7.60 (dd, J = 8.0, 1.8 Hz, 1H), 7.56 – 7.47 (m, 2H), 7.38 (d, J = 4.1 Hz, 1H), 4.77 (s, 2H),

2.28 (s, 3H), 1.33 (s, 8H). ^{13}C NMR (100 MHz, $CDCl_3$) δ 189.4, 161.8, 149.6, 140.3, 136.2, 131.0, 130.5, 126.2, 124.5, 120.6, 119.6, 108.4, 54.2, 23.4, 15.9.

2,2'-(3,6-Di([2,2'-bithiophen]-5-yl)-1,4-dioxopyrrolo[3,4-*c*]pyrrole-2,5(1*H*,4*H*)-diyl)diacetic acid (25). ^{1}H NMR (400 MHz, $CDCl_3$, 1%Et_3N) δ 8.50 (d, *J* = 3.9 Hz, 1H), 7.72 – 7.38 (m, 3H), 7.14 (d, *J* = 4.2 Hz, 1H), 4.77 (s, 2H). ^{13}C NMR (101 MHz, $CDCl_3$, 1%Et_3N) δ 167.5, 161.3, 143.3, 139.4, 136.6, 136.4, 128.7, 128.4, 126.7, 125.6, 125.4, 108.3, 100.3, 44.6.

REFERENCES

1. Butler, M. S., *J. Nat. Prod*., **2004**, *67*, 2141.

2. Nisbet, L. J.; Moore, M., *Curr. Opin. Biotechnol*., **1997**, *8*, 708.

3. (a) Shahid, M.; Ul-Islam, S.; Mohammad, F., *J. Clean. Prod*., **2010**, *53*, 310. (b) Gandía-Herrero, F.; García-Carmona, F.; Escribano, J., *Phytochem. Anal.*, **2006**, *17*, 262. (c) Gandía-Herrero, F.; Escribano, J.; García-Carmona, F., *J. Nat. Prod.*, **2012**, *75*, 1030. (d) C. I.; Oprea, A.; Dumbravă, I. Enache, A.; Georgescu, Gîrț M. A., *J. Photochem. Photobiol. A*, **2012**, *240*, 5.

4. (a) Wünsche, J.; Deng, Y.; Kumar, P.; Di Mauro, E.; Josberger, E.; Sayago, J.; Pezzella, A.; Soavi, F.; Cicoira, F.; Rolandi, M.; Santato, C., *Chem. Mater.*, **2015**, *27*, 436. (b) Ye, Y. Q.; Koshino, H.; Abe, N.; Nakamura, T.; Hashizume D.; Takahash S., *Biosci., Biotechnol., Biochem*, **2010**, *11*, 2342. (c) Kourounakis, A. P.; Rekka, E. A.; Kourounakis, P. N., *J. Pharm Pharmacol*., **1997**, 49, 938.

5. Bowden, B. F.; Coll, J. C.; Tapiolas, D. M., *Aust. J. Chem*., **1983**, *36*, 211. Harmon; A. D.; Weisgraber, K. H.; Weiss, U. *Cell. Mol.Life Sci.*, **1979**, *36*, 54.

6. Gordon, M. *Chem. Rev.* **1951**, *50*, 127-200.

7. Liu, R. S. H., *J. Chem. Ed*., **2002**, *79*, 183.

8. Shevyakov,S.; Li, H.; Muthyala, R.; Asato, A. E.; Croney, J. C.; Jameson, D. M.; Liu, R. S. H., *J. Chem. Phys. A*, **2003**, *107*, 3295.

9. Liu, R. S. H.; Muthyala, R. S.; Wang, X.-s.; Asato, A. E., *Org. Lett.* **1999**, 269-271.

10. (a) Schmitt, S.; Baumgarten, M.; Simon, J.; Hafner, K. *Angew. Chem., Int. Ed.* **1998**, *37*, 1077. (b) Ito, S.; Morita, N. Eur. *J. Org. Chem*. **2009**, 4567.

11. Wang, F.; Lin, T. T.; He, C.; Chi, H.; Tang, T.; Lai, Y.-H. *J. Mater. Chem.* **2012**, *22*, 10448. Tang, T.; Ding, G.; Lin, T.; Chi, H.; Liu, C.; Lu, X.; Wang, F.; He C. *Macromol. Rapid Commun,*. **2013**, *34*, 431.

12. Tang, T.; Lin, T.; Wang, F.; He, C. *Polym. Chem.* **2014**, *5*, 2980.

13. Yamaguchi, Y.; Ogawa, K.; Nakayama, K.-I.; Ohba, Y.; Katagiri, H. *J. Am. Chem. Soc*., **2013**, *135*, 19095.

14. Wang, F.; Lai, Y.-H.; Kocherginsky, N. M.; Kosteski, Y. Y. *Org. Lett*., **2003**, *5*, 995.

15. Lacroix, P. G.; Malfant, I.; Iftime, G.; Razus, A. C.; Nakatani, K.; Delaire, J. A. *Chem. Eur. J*., **2000**, *6*, 2599.

16. Cristian, L.; Sasaki, I.; Lacroix, P. G.; Donnadieu, B.; Asselberghs, I.; Clays, K.; Razus, A. C. *Chem. Mater*., **2004**, *16*, 3543.

17. Salman, H.; Abraham, Y.; Tal, S.; Meltzman, S.; Kapon, M.; Tessler, N.; Speiser, S.; Eichen, Y. Eur. *J. Org. Chem*., **2005**, 2207.

18. Murai, M.; Ku, S.-Y.; Treat, N. D.; Robb, M. J.; Chabinyc, M. L.; Hawker, C. *J. Chem. Sci*., **2014**, *5*, 3753.

19. Puodziukynaite, E.; Wang, H.-W.; Lawrence, J.; Wise, A. J.; Russell, T. P.; Barnes; M. D., Emrick, T. *J. Am. Chem. Soc*., **2014**, *136*, 11043.

20. Grellmann, K. H.; Heilbronner, E.; Seiler, P.; Weller, A. *J. Am. Chem. Soc.* **1968**, *90*, 4238.

21. Liu, R. S. H.; Muthyala, R. S.; Wang, X.-s.; Asato, A. E.; Wang, P.; Ye, C. *Org. Lett*., **2000**, *2*, 269.

22. (a) Lacroix, P. G.; Malfant, I.; Iime, G.; Razus, A. C.; Nakatani, K.; Delaire, J. A. *Chem.–Eur. J*., **2000**, *6*, 2599. (b) Mitchell, R.; Gillispie, G. D. *J. Phys. Chem.*, **1989**, *93*, 4390.

23. Amir, E.; Amir, R. J.; Campos, L. M.; Hawker, C. J. *J. Am. Chem. Soc*., **2011**, *133*, 10046.

24. Amir, E.; Murai, M.; Amir, R. J.; Cowart, Jr., Chabinyc, M. L.; Hawker, C. *J. Chem. Sci.*, **2014,** *5*, 4483.

25. Koch, M.; Blacque, O.; Venkatesan, K. *Org. Lett*., **2012**, *14*, 1580.

26. Koch, M.; Blacque, O.; Venkatesan, K. J. Mater. Chem. C, **2013**, *1*, 7400.

27. Balduzzi, S.; Muller-Bunz, H.; McGlinchey, M. *J. Chem. Eur. J*., **2004**, *10*, 5398.

28. Song, J.; Hansen H. -J. *Helv. Chim. Acta*., **1999**, *82*, 309.

29. (a) Makinoshima,T.; Fujitsuka, M.; Sasaki, M.; Araki, Y.; Ito, O.; Ito, S.; Morita, N. *J. Phys. Chem. A*, **2004**, *108*, 368. (b) Yeow, E. K.; Steer, R. P. Phys. *Chem. Chem. Phys*., **2003**, *5*, 97.

30. Jin, M.; Hong, H.; Xie, J.; Malval, J.-P.; Spangenberg, A.; Soppera, O.; Wan, D.; Pu, H.; Versace, D.-L.; Leclerc, T.; Baldeck, P.; Poizate, O.; Knopf, S., *Polym. Chem*., **2014**, *5*, 4747.

31. Xing, J.-F.; Dong, X.-Z.; Chen, W.-Q.; Duan, X.-M.; Takeyasu, N.; Tanaka, T.; Kawata, S., *Appl. Phys. Lett*., **2007**, *90*, 131106.

32. Tormen, M.; Businaro, L.; Altissimo, M.; Romanato, F.; Cabrini, S.; Perennes, F.; Proietti, R.; Sun, H.-B.; Kawata, S.; Di Fabrizio E., *Microelectron. Eng*., **2004**, *73*, 535.

33. Weil, T.; Vosch, T.; Hofkens, J.; Peneva, K.; Müllen, K. *Angew. Chem., Int. Ed*., **2010**, *49*, 9068. Carret, S.; Blanc, A.; Coquerel, Y.; Berthod, M.; Greene, A. E.; Deprés, J.-P. *Angew. Chem., Int. Ed*. **2005**, *44*, 5130.

34. Yamaguchi, Y.; Maruya, Y.; Katagiri, H.; Nakayama, K.; Ohba, Y. *Org. Lett*., **2012**, *14*, 2316.

35. Kurotobi, K.; Kim, K. S.; Noh, S. B.; Kim D.; Osuka, A. *Angew. Chem., Int. Ed*., **2006**, *45*, 3944.

36. Hafner, K.; Schneider, J. *Justus Liebigs Ann. Chem., **1959**, 624*, 37.

37. Devendar, B.; Ku, C.-K.; Chenga, L.-Y.; Yang, S.-J.; Chena, J.-X.; Wu, C.-P. *Helv Chim Acta*., **2014**, *97*, 507.

38. Zhou, Z.; Parr, R. G. *J. Am. Chem. Soc*., **1989**, *111*, 7371.

39. Wang, X.; Kok-Peng Ng, J.; Jia, P.; Lin, T.; Cho, C.M.; Xu, J.; Lu, X.; He, C.; *Macromolecules*, **200**9, *42*, 5534.

40. Jin, M.; Hong, H.; Xie, J.; Malval, J.-P.; Spangenberg, A.; Soppera, O.; Wan, D.; Pu, H.; Versace, D.-L.; Leclerc, T.; Baldeck, P.; Poizate, O.; Knopf, S. *Polym. Chem*., **2014**, *5*, 4747.

41. Yanez, C. O.; Andrade, C. D.; Yao, S.; Luchita, G.; Bondar, M. V.; Belfield, K. D. *ACS Appl. Mater. Interfaces*, **2009**, *1*, 2219.

42. Fiori, J.; Gotti, R.; Albini A.; Cavrini, V. *Rapid Commu. Mass Spec.*, **2008**, *22*, 2698.

43. Dean, J. A.; Lange, N. A. *Lange's Handbook of Chemistry*, 15th edn., McGraw-Hill, 1999.

44. Hell, S.W.; Wichmann, J. *Opt. Lett.*, **1994**, *19*, 780.

45. Hell, S.W. *Science*, **2007**, *316*, 1153.

46. Hell, S.W. *Nat. Biotechnol.*, **2003**, *21*, 1347.

47. Hell, S.W., *Nat. Methods*, **2009,** *6*, 24-32.

48. Gustafsson, M. G., *Proc. Natl. Acad. Sci.*, **2005**; *102*, 13081.

49. Rust, M. J., Bates, M.; Zhuang, X. *Nat. Methods*, **2006**, *3*, 793.

50. Betzig, E., Patterson, G. H.; Sougrat, R.; Lindwasser, O. W.; Olenych, S.; Bonifacino, J. S. M.; Davidson, W.; Lippincott-Schwartz, J.; Hess, H. F. *Science*, **2006**, *313*, 1642.

51. Hess, S. T., Girirajan, T. P.; Mason, M. D., *Biophys. J.*, **2006**, *91*, 4258.

52. Abbé, E., *Mikroskop. Anat.*, **1873**, *9*, 413.

53. Hao, Z.; Iqbal, A., *Chem. Soc. Rev.*, **1997**, *26*, 203-213.

54. Zhu, Y.; Rabindranath, A. R.; Beyerlein, T.; Tieke, B., *Macromolecules,* **2007**, *40*, 6981-6989.

55. Qu, S.; Tian, H., *Chem. Commun.*, **2012**, *48*, 3039-3051.

56. Li, H.; Liu, F.; Wang, X.; Gu, C.; Wang, P.; Fu, H., *Macromolecules* **2013**, *46*, 9211-9219.

57. Tamayo, A. B.; Dang, X.-D.; Walker, B.; Seo, J.; Kent, T.; Nguyen, T.-Q., *Appl. Phys. Lett.*, **2009**, *94*, 103301/1-3.

58. Zhang, G.; Bi, S.; Song, L.; Wang, F.; Yu, J.; Wang, L., *Dyes Pigm.*, **2013**, *99*, 779-786.

59. Fukuda, M.; Kodama, K.; Yamamoto, H.; Mito, K., *Dyes Pigm.,* 2002, *53*, 67-72.

60. Fukuda, M.; Kodama, K.; Yamamoto, H.; Mito, K., *Dyes Pigm*., **2004**, *63*, 115-125.

61. Zhang, G.; Wang, L.; Cai, X.; Zhang, L.; Yu, J.; Wang, A., *Dyes Pigm.,* **2013**, *98*, 232-237.

62. Ftouni, H.; Bolze, F.; Nicoud, J.-F., *Dyes Pigm.,* **2013**, *97*, 77-83.

63. Deng, L.; Wu, W.; Guo, H.; Zhao, J.; Ji, S.; Zhang, X.; Yuan, X.; Zhang, C., *J. Org. Chem*., **2011**, *76*, 9294-9304.

64. Wang, B.; He, N.; Li, B.; Jiang, S.; Qu, Y.; Qu, S.; Hua, J., *Aust. J. Chem.,* **2012**, *65*, 387-394.

65. Xiao, P.; Hong, W.; Li, Y.; Dumur, F.; Graff, B.; Fouassier, J. P.; Gigmes, D.; Lalevée, J., *Polymer,* **2014**, *55*, 746-751.

66. Tamayo, A. B.; Tantiwiwat, M.; Walker, B.; Nguyen, T.-Q., *J. Phys. Chem. C,* **2008**, *112*, 15543-15552.

67. Zhang, G.; Song, L.; Bi, S.; Wu, Y.; Yu, J.; Wang, L., *Dyes Pigm.,* **2014**, *102*, 100-106.

68. Liu, S.-Y.; Shi, M.-M.; Huang, J.-C.; Jin, Z.-N.; Hu, X.-L.; Pan, J.-Y.; Li, H.-Y.; Jen, A. K.-Y.; Chen, H.-Z., *J. Mater. Chem., A* **2013**, *1*, (8), 2795-2805.

69. Kirkus, M.; Wang, L.; Mothy, S.; Beljonne, D.; Cornil, J.; Janssen, R. A. J.; Meskers, S. C. J., *J. Phys. Chem. A,* **2012**, *116*, 7927-7936.

70. Kuwabara, J.; Yamagata, T.; Kanbara, T., *Tetrahedron,* **2010**, *66*, 3736-3741.

71. Lafleur-Lambert, A.; Rondeau-Gagné, S.; Soldera, A.; Morin, J.-F., *Tetrahedron Lett*., **2011**, *52*, 5008-5011.

72. Mizuguchi, J., *J. Phys. Chem. A*, **2001**, *105*, 1125-1130.

73. Richert, S.; Mosquera-Vazquez, S.; Grzybowski, M.; Gryko, D. T.; Kyrychenko, A.; Vauthey, E., *J. Phys. Chem. B*, **2014**, *118*, 9952-9963.

74. Alp, S.; Ertekin, K.; Horn, M.; Icli, S., *Dyes Pigm.*, **2004**, *60*, 103-110.

75. Corredor, C. C.; Belfield, K. D.; Bondar, M. V.; Przhonska, O. V.; Yao, S., *J. Photoch. Photobio. A*, **2006**, *184*, 105.

76. Huo, L.; Hou, J.; Chen, H.-Y.; Zhang, S.; Jiang, Y.; Chen, T. L.; Yang, Y., *Macromolecules*, **2009**, *42*, 6564.

77. Yamagata, T.; Kuwabara, J.; T., K., *Tetrahedron* **2014**, *70*, 1451.

78. Palai, A. K.; Mishra, S. P.; Kumar, A.; Srivastava, R.; Kamalasanan, M. N.; Patri, M., *Macromol. Chem. Phys.* **2010**, *211*, 1043.

79. Belfield, K. D.; Bondar, M. V.; Haniff, H. S.; Mikhailov, I. A.; Luchita, G.; Przhonska, O. V., *ChemPhysChem* **2013**, *14*, 3532.

80. Lakowicz, J. R., Principles of fluorescence spectroscopy. Kluwer: New York, 1999.

81. Magde, D.; Wong, R.; Seybold, P. G., *Photochem. Photobiol*. **2002**, *75*, (4), 327.

82. Belfield, K. D.; Bondar, M. V.; Morales, A. R.; Yue, X.; Luchita, G.; Przhonska, O. V., *J. Phys. Chem. C* **2012**, *116*, 11261.

83. Belfield, K. D.; Bondar, M. V.; Morales, A. R.; Yue, X.; Luchita, G.; Przhonska, O. V.; Kachkovsky, O. D., *ChemPhysChem* **2012**, *13*, (15), 3481.

84. Sheik-Bahae, M.; Said, A. A.; Wei, T. H.; Hagan, D. J.; Van Stryland, E. W., *J. Quantum Elect.* **1990**, *26*, (4), 760.

85. Belfield, K. D.; Bondar, M. V.; Morales, A. R.; Frazer, A.; Mikhailov, I. A.; Przhonska, O. V., *J. Phys. Chem. C* **2013**, *117*, 11941.

86. Lepkowicz, R. S.; Przhonska, O. V.; Hales, J. M.; Hagan, D. J.; Van Stryland, E. W.; Bondar, M. V.; Slominsky, Y. L.; Kachkovski, A. D., *Chem. Phys.* **2003**, *286*, (2-3), 277.

87. Belfield, K. D.; Bondar, M. V.; Yanez, C. O.; Hernandez, F. E.; Przhonska, O. V., *J. Phys. Chem.* B **2009**, *113*, (20), 7101.

88. Hales, J. M.; Matichak, J.; Barlow, S.; Ohira, S.; Yesudas, K.; Brédas, J.-L.; Perry, J. W.; Marder, S. R., *Science* **2010**, *327*, 1485.

89. Strickler, S. J.; Berg, R. A., *J. Chem. Phys.* **1962**, 3, (4), 814.

90. Albota, M. A.; Xu, C.; Webb, W. W., *Appl. Optics* **1998**, *37*, (31), 7352.

91. Heo, C. H.; Kim, K. H.; Kim, H. J.; Baik, S. H.; Song, H.; Kim, Y. S.; Lee, J.; Mook-jung, I.; Kim, H. M., *Chem. Commun*. **2013**, *49*, 1303.

92. Yuan, L.; Lin, W.; Chen, H.; Zhu, S.; He, L., *Angew. Chem. Int. Ed*. **2013**, *52*, 10018.

93. Golibrzuch, K.; Ehlers, F.; Scholz, M.; Oswald, R.; Lenzer, T.; Oum, K.; Kim, H.; Koo, S., *Phys. Chem. Chem. Phys*. **2011**, *13*, 6340.

94. Fita, P.; Fedoseeva, M.; Vauthey, E., *J. Phys. Chem. A* **2011**, *115*, (12), 2465.

95. Kosumi, D.; Maruta, S.; Fujii, R.; Kanemoto, K.; Sugisaki, M.; Hashimoto, H., *Phys. Status Solidi C* **2011**, *8*, (1), 92.

96. Kumar, K. S.; Selvaraju, C.; Padma Malar, E. J.; Natarajan, P., *J. Phys. Chem. A* **2012**, *116*, 37.

97. Szemik-Hojniak, A.; Deperasin´ska, I.; Oberda, K.; Erez, Y.; Huppert, D.; Nizhnik, Y. P., *Phys. Chem. Chem. Phys*., **2013**, *15*, 9914.

98. Efimova, S. L.; Malyukin, Y. V., *Funct. Mat.,* **2002**, *9*, 247.

99. Deshpande, A. V.; Beidoun, A.; Penzkofer, A.; Wagenblast, G., *Chem. Phys*., **1990**, *142*, 123.

100. Albota, M.; Beljonne, D.; Bredas, J. L., *Science*, **1998**, *281*, 1653.

101. Tobita, E.; Ida, K.; Shiobara, S., *Res. Chem. Intermed.*, **2000**, *27*, 205.

102. He, X. M.; Carter, D. C. *Nature*, **1992**, *358*, 209.

103. Krenzel, E. S.; Chen, Z.; Hamilton, J. A. *Biochemistry*, **2013**, *52*, 1559.

104. Batrakova, E. V.; Kabanov, A. V. *J Control Rel*., **2008**, *130*, 98.

105. Escobar-Chavez, J. J.; Lopez-Cervantes, M; Naik, A; Kalia, Y. N.; Quintanar-Guerrero, D; Ganem-Quintanar, A. *J Pharm Pharmaceut Sci*., **2006**, *9*, 339.

106. Sahay, G.; Batrakova, E. V.; Kabanov, A. V. *Bioconjugate Chem*., **2008**, *19*, 2023.

107. Malich, G.; Markovic, B.; Winder, C. *Toxicology*, **1997**, *124*, 179.

108. Bürckstümmer, H.; Weissenstein, A.; Bialas, D. Würthner, F. *J. Org. Chem*., **2011**, *76*, 2426.